Ultrafast Photochemical Reactivity of Heptazine-Based Materials

Kathryn Corp

A dissertation

submitted in partial fulfillment of the

requirements for the degree of

Doctor of Philosophy

University of Washington

2019

Reading Committee:

Cody Schlenker, Chair

Daniel Gamelin

Xiaosong Li

Program Authorized to Offer Degree:

Chemistry

University of Washington

Abstract

Ultrafast Photochemical Reactivity of Heptazine-Based Materials

Kathryn Corp

Chair of the Supervisory Committee:
Professor Cody Schlenker
Department of Chemistry

Solar energy conversion and storage is one key aspect in addressing and mitigating the global energy crisis. Photon conversion efficiencies and production rates of photovoltaics have dramatically increased over the last few decades, yet intermittent availability of solar energy will continue to limit the environmental and economic benefits of this technology unless storage becomes more cost effective and available. One avenue that is gaining traction for all-in-one solar energy conversion and storage is photocatalytic water splitting. Graphitic carbon nitride, an organic photocatalyst for hydrogen evolution, has become popular to study for the ease of synthesis and low cost due to the abundance of precursor materials. However, high structural ambiguity and low solubility causes characterization of charge transport in carbon nitride-like materials to be nearly unattainable, leaving many unanswered photophysical questions.

Work enclosed in this dissertation is the first to spectroscopically demonstrate an electron transfer between two carbon nitride co-catalysts for increased hydrogen evolution. This finding suggests electron quenching happens on the order of the diffusion rate for small molecules, which led us to study a model heptazine-based molecule for hydrogen evolution. Additionally, we are interested in studying the water oxidation mechanism to eliminate the need for sacrificial electron scavengers. Interestingly, we discovered the first excited-state proton-coupled electron transfer (ES-PCET) mechanism from water to heptazine that results in heptazinyl and hydroxyl radicals, validating theoretical predictions.

In efforts to better understand the ES-PCET mechanism, we used a series of phenol derivatives, R-PhOH, to tune the excited state energy landscape. As the electron donating ability of the substituent on phenol increases, the luminescence quenching increases, and the kinetic isotope effect decreases. This suggests as the oxidation potential of R-PhOH shifts cathodically, the charge transfer curve is easier to access and thus the electron transfer becomes more favorable. This is supported by increased radical generation rates seen for more electron donating substituents on phenol. Furthermore, we studied the role of branching ratios post-excitation on accessing the charge transfer state using ultrafast pump-push-probe spectroscopy. We found that the excited-state landscape is heavily influenced by an additional “push” pulse for electron withdrawing phenols compared to electron donating phenols, confirming again that the barrier height for reaching the charge transfer state decreases with more electron donating phenols.

From these studies we can outline a set of design rules for chemists and materials scientists to synthesize heptazine-based molecules for increased water oxidation. Specifically, our results suggest functionalizing the heptazine core with electron withdrawing groups to shift the charge transfer curve toward the lowest hydrogen bound excited state for increased ES-PCET with water.

TABLE OF CONTENTS

LIST OF FIGURES

LIST OF TABLES

ACKNOWLEDGEMENTS

First, to my husband James. My absolute favorite thing about graduate school is meeting you. I am unbelievably lucky to have you in my life. I can’t imagine going through the struggles and triumphs of graduate school without you. Thank you for pushing me to do better even when I really don’t want to; I’ve pushed past so many barriers because of you. I love you.

I would like to thank my parents for all the support and encouragement they have provided my entire life. In their eyes there is nothing I can’t do which gives me confidence to be whatever I want to be, no matter what people think. Thank you both for everything.

My dearest sister, Melissa – I have always admired your drive to succeed in everything you do. You live life to the fullest and I appreciate that attitude when I need a pick-me-up. I think graduate school has brought us closer together even though we live so far away. Thank you for being my role model and teaching me what not to do. And thank you for bringing two of the most darling nieces into my life, and a brother!

Madeline, you are a big breath of sunshine. On the days I wanted to quit, you told me you want to be a scientist just like your aunt Katie. I couldn’t let you down, so I kept just going. I will always thank you for that. You’ve grown up into a smart, witty, kind, and beautiful girl and I can’t wait to see where life takes you.

Emberly, you just started walking a few months ago but you’ve already brought so much joy to our family. You always get your way and I hope that never stops.

Grandma Corp. Thank you for being a fierce businesswomen, teaching me how to remodel homes, and supporting my every move. Having you as a role model and someone I want to make proud has always kept me pushing harder and further than I originally think is possible. Thank you and I love you.

To the Gaynor family: Thank you for welcoming me into the family with open arms and endless love. James and I are extremely lucky to have you.

To my kittens, Reggie and Bella – thank you for providing so much love and joy over the last four years. Your cuddles while I work at home are amazing and keep me pinned down so I work a little longer than I would without you.

I would like to thank the miracle of coffee for getting me through graduate school. James got me addicted during our second year and I am positive I would not have been as productive as often without it. A giant shout out goes to the Solstice Café in the University District for providing me with unlimited amounts of caffeinated goodness and treats while writing my thesis. I would also like to thank the late Dr. Daniel Wright for the espresso machine. We use it every day and we will continue to until it is completely unusable.

Microsoft Word, thank you for crashing significantly less than I expected while writing my thesis. And thank you to whomever developed cross-referencing, you are a lifesaver.

Dr. Brian Gilbert, thank you for letting 19-year-old me join your research lab at Linfield! I remember the day so clearly. I thought I was interviewing for a position, but you had already let me in and started talking about my project. I cried tears of joy after this meeting and so did my dad. Somehow you knew that I had it in me well before I did. Thank you for getting me excited about research and encouraging me to go to graduate school. Look at me now!

To my Membrion family. Thank you for warmly welcoming me into your company for six months. I gained so much confidence during my time at Membrion because of your unwaveringly trust in my abilities. I hope I have the chance to work with all of you in the future. Specifically, I want to thank Dr. Stephanie Candelaria for writing a winning grant proposal, hiring me, and being an awesome friend. I greatly enjoyed putting a project together from scratch with you. I also want to thank Dr. Greg Newbloom for being the most incredible boss. Thank you for having confidence that I could figure out whatever problem arose. You have created a wonderful company that I have the utmost confidence will continue flourish in the years to come.

Piper Jahnke, thank you for being my best friend. We've always gone through the good times and the bad times as a team and I hope that never changes.

Brandon Nolan, I am incredibly happy to have you as one of my closest friends. I love your hugs, dance moves, and sincere joy for the people in your life. Thank you for being one of the most genuine people I know, always making me laugh, and caring about your friends and family so deeply.

Tori Kensy, I am so thankful that we have each other. Thank you for always watching Grey's with me, sending/receiving countless animal videos and for always speaking your mind.

Lucas Flagg, thank you for being my sounding board for crazy science ideas, bribing me to get out of lab occasionally, cooking us dinner and playing cards. One of my favorite things about our friendship is somehow being able to read each other's minds. I hope that never changes.

Caitlin Repp and Dorothy Sterling, thank you for always being willing to grab coffee or have a BBQ and pretend like I'm not *still* in school.

Nicole Revis and Jordan Rivers, thank you for our great, nerdy friendship since middle school.

A huge thank you goes to the University of Washington Chemistry Department staff. You are all champions and deserve honorary doctorates for managing everyone's schedules, keys, the stockroom, hundreds of instruments, purchasing, event logistics, the list goes on. Specifically, I want to thank Kim Quigley, Diana Knight, and Lochlan Hickok. I appreciate your friendship, advice, and sarcastic comments. Navigating a PhD would have been a mess without the three of you. Additionally, I'd like to thank the electronics shop, the machine shops (physics and chemistry), and the glass blowing shop for teaching me how to make parts or making parts for me that were crucial for my research.

The Clean Energy Institute (CEI) was one of the main reasons I decided to come to UW and I want to thank everyone who has dedicated their time to make it what it is today. It is making a difference and it’s only just begun. Thank you for funding a full year of graduate school through various fellowships; I loved getting to put all my focus into research and K-12 outreach events during those periods. Lastly, I want to thank the CEI staff for putting together lab tours and networking events. I have learned a lot about industry because of those events and I feel much more prepared to enter the non-academic world because of them.

To my chemistry graduate cohort. Thank you for being amazing friends and encouraging each other to keep going. I can’t believe how quickly time passed and that we did it! I’m so thankful we had each other through one of the craziest times of our lives. From late-night ice cream runs to 90’s parties to intramural soccer games – we got through it together.

To all the student’s I’ve taught during my time at UW: thank you for reminding me how far I’ve come from my undergraduate days. I cherish the “chemistry is SO cool” moments and the friendships I’ve developed with some of you.

My last set of acknowledgements go to the members of the Schlenker Lab. We have built a weird little family over the last five years and I am most sad to leave that. We’ve been through some amazing times and some rough periods, but someone was always there to celebrate or comfort day or night. The following thanks are in alphabetical order by first name so you can’t fight over who I liked the most.

Dana, we miss you like crazy, but we are so proud of you kicking butt at NREL. Thank you for all the advice and paving the way for the rest of us. Emily, thank you for our vent sessions, taco Tuesdays, Barre classes and joining me on team photocatalysis. You made me a better scientist and human. Emma, thank you for obsessing over cranes with me, letting me play with your dogs, and brainstorming about science and life. Jarred, thank you for teaching me almost everything I know about electrochemistry. Liam, thank you for being willing to stay late literally anytime I needed you to and telling the most bizarre stories I've ever heard. Mitchell, thank you for measuring radical generation rates for me and loving cats as much, if not more, than I do. Ryan, thanks for always making us laugh with your snapchat filters and for making us molecules when we didn't want to. Sabrina, thank you for being so willing to try such crazy experiments with me and for being the sweetest person ever. Sarah, thank you for laughing so hard you cry which makes me laugh/cry and for being such a genuine friend. And thank you for making my squaraine upconversion dreams come true. Tim, thank you for our science and life chats. I will always call you when I need a beer or a cute baby animal video.

And last, but certainly not least, Cody: I have learned a tremendous amount from you over the past five years and I can't thank you enough. I joined your lab because you proposed interesting and meaningful research, you were very kind, and mostly because you were incredibly excited about science. I am very thankful all those reasons held true over the years. I appreciate that you were always available to talk about science and troubleshoot with me in lab if I was struggling. Thank you for being an amazing advisor and keeping all of our best interests in mind.

To my friends, family, and wonderful husband.

“Life is a relationship among molecules, not a property of any [single] molecule.”

-Linus Pauling

Chapter 1. Introduction

1.1 THE GLOBAL ENERGY PROBLEM

The greenhouse gas production associated with human activities, such as burning fossil fuels and coal to generate electricity, is an environmental problem affecting global health and sustainability. Recent improvements in solar photovoltaics, CO_2 sequestration, and batteries are promising avenues to offset the global warming effects; however, there is still room and need for improvement.

Solar energy is a nearly unlimited and free resource which shows great promise for alleviating the global energy problem. The amount of solar energy hitting Earth's surface in 90 minutes is enough to provide energy to the world for one year.[1] Solar photovoltaic technology has greatly improved over the last 40 years and production rates have dramatically increased such that the price per kilowatt-hour for solar energy can be as low as 6 cents/kWh on the utility scale which rivals that of coal and natural gas generation methods.[2-3] However, intermittent availability of solar energy presents a challenge. The well-known duck curve shown in Figure 1-1 demonstrates the difference in electricity demand and solar power generation throughout an average day.[4] At peak sunlight hours, over-generation is a problem that is increasing each year as more photovoltaics are placed on the grid. Grid operators curtail the generation – essentially throwing away the excess – and turn on generators well before the sun sets. If operators did not curtail the generation, they would need to ramp the generators faster than suggested which could result in failure of the generators. Curtailment unfortunately minimizes the environmental benefits of using solar energy since a portion of the solar energy is thrown away. To mitigate this problem, energy storage technology needs improvement and implementation so solar energy can be used even when the sun isn't shinning.

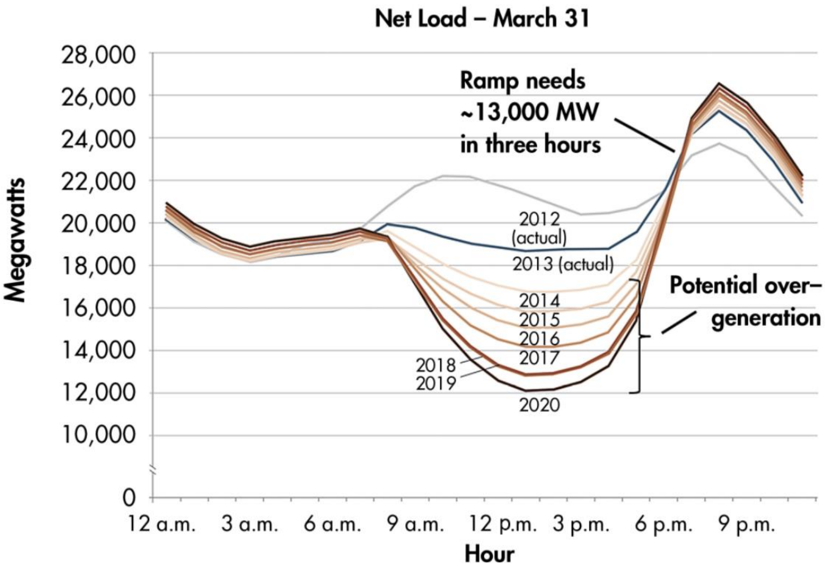

Figure 1-1. The "duck curve" shows the difference in electricity demand and solar power generation throughout an average day from 2012 projected to 2020, increasing the amount of solar power generation each year. Graph from the Department of Energy.[4]

One attractive avenue for storing solar energy is to produce hydrogen gas, an energy dense fuel, in photocatalytic or photoelectrochemical water splitting. One advantage of using hydrogen gas as a fuel is that burning hydrogen gas has no carbon emission; the only biproducts are water and electricity.

Inorganic materials systems such as cadmium chalcogenide nanostructures,[5] *pn* junction silicon,[6-8] and numerous metal oxides[9-10] exhibit activity toward hydrogen evolution. However, these all pose sustainability challenges due to the cost and scarcity of the metal, risks for adverse environmental outcomes (e.g. Cd^{2+} released by photocorrosion), or inadequate scalability, which has limited their commercial development.[11] Carbon-based molecular species,[12-13] oligomers,[14-15] polymers,[16-20] and extended higher-dimensional structures[21-25] are receiving increasing attention as components in photocatalytic systems due to their potential for lower production costs and the ease with which they can be synthetically tailored from earth-abundant starting materials.

Carbon nitride, a heptazine-based polymer known since the early 19th century,[26] has recently shown promise for driving photocatalytic hydrogen evolution from water.[27-29] One particularly compelling quality of graphitic carbon nitride (g-C_3N_4) and its oligomers is that they can be easily prepared via pyrolysis of inexpensive and earth-abundant precursors, such as urea.[30-33] Their catalytic activity toward hydrogen evolution can also be significantly enhanced by non-noble metal[34-37] and metal-free[27] co-catalysts, circumventing the need for cost-prohibitive precious metals. Thus, their potential for low-cost production and their chemical stability make carbon nitrides appealing as scalable, clean energy conversion materials.

1.2 HISTORY OF GRAPHITIC CARBON NITRIDE

Carbon nitride, a name coined for the chemically robust polymer typically made of heptazine or triazine units, was first made in 1834 by Justus von Liebig.[26] Several different monomers, oligomers, and polymers with the similar base units were synthesized and elementally characterized in the 1800 and 1900’s.[38-40] The structure was not well understood for some time, however in the 1930’s Edward C. Franklin gave Linus Pauling carbon nitride-like crystals (at this time it was $C_6N_7O_3Na_3 \cdot 3H_2O$) to perform the first X-ray study.[41] Pauling proposed the three fused ring structure (tri-s-triazine) we know today, but it was not confirmed until the 1980’s by Nelson Leonard and coworkers.[42] The coplanar structure is shown in Figure 1-2.

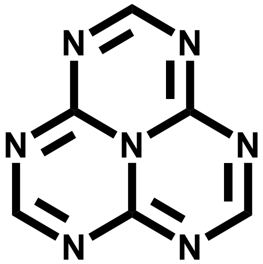

Figure 1-2. Proposed fused ring structure (tri-s-triazine) by Pauling and Leonard.

Carbon nitride has recently emerged as a promising photocatalyst for hydrogen evolution and water splitting using ultraviolet and visible light that withstands harsh chemical environments.[43-45] One particularly compelling quality of graphitic carbon nitride (g-C_3N_4) and its oligomers is that they can be easily prepared via pyrolysis (400 - 600 degrees Celsius) of inexpensive and earth-abundant precursors such as urea, thiourea, melamine, thiocyanate and others.[46-51] However, the bulk synthesis conditions often result in high structural ambiguity and reproducibility issues. Due to the difficulty of characterizing these bulk materials and their low solubility in common solvents, the research community is plagued with unanswered photophysical questions that could help clarify hydrogen evolution and water oxidation mechanisms. There are nearly 19,000 papers concerning carbon nitride materials and only a handful of studies have focused on the charge transfer dynamics.[52-55] Therefore rational design rules for improving photochemical reactivity remain unclear in such systems. Chapter 2 will discuss the first photophysical study on a photoinduced charge transfer mechanism between two carbon nitride species.[56] In summary, we showed that there is an electron transfer from bulk graphitic carbon nitride to exfoliated (oligomeric species rich with oxygen defects) which drastically increases the hydrogen evolution rate with or without a platinum catalyst present. This finding is the first ultrafast characterization of electron transfer between carbon nitride species as well as the first unambiguous characterization of electron and hole absorption in the near infrared. Transient absorption, time-resolved luminescence, global target analysis and spectro-electrochemical techniques were the keys to characterizing this charge transfer process.

1.3 PHOTOCHEMICAL REACTIVITY IN AZA-AROMATIC SYSTEMS

The origin of photochemical reactivity in aza-aromatics has been heavily debated in the literature for at least 70 years. Over this period of time, acridine has been used as a model aza-aromatic compound of which the photochemistry has been extensively studied.[57-62] Historically, the rich photochemistry of these *N*-heteroaromatics, such as acridines, purines, and quinolines in protic media was assumed to proceed directly from low-lying local molecular excited states of the heteroaromatic.[58, 63-64] By local molecular excited states we mean those involving only the orbitals of the chromophore, with no contribution from neighboring solvent molecules. Remarkably, until recently the electronic configuration of the reactive excited state continued to be a contentious issue in the literature, with some reports claiming that any one of the individual $^1\pi\pi^*$, $^3\pi\pi^*$, $^1n\pi^*$, or $^3n\pi^*$ states is the reactive species, while others provided respective counter arguments rejecting them.[57-62]

In 2014, Eisenhart and Dempsey showed a proton-coupled electron transfer (PCET) mechanism by which the local triplet excited state drives H-atom transfer from phenol to acridine orange.[65] Using computational methods, Domcke and coworkers have demonstrated an H-atom abstraction reaction with acridine,[66] and more recently in heptazine-based molecules.[67-68] Authors show this H-atom abstraction reaction involves a manifold of states comprising both aza-aromatic and hydroxylic orbitals of the H-bonded intermolecular complex.

PCET reactions are scientifically and technologically relevant beyond studying the aza-aromatic photochemical reactivity. In general, PCET is pertinent for characterizing and controlling energy conversion and storage processes since the coupled electron and proton motion lowers the charge transfer barrier.[69-73] The majority of intermolecular PCET literature to date focuses on metal-containing complexes,[69-71, 74] with fewer examples of all-organic heterocyclic aromatics.[65, 75-76] The research contained in this thesis is some of the first experimental results suggesting PCET between heptazine-based molecules and H-atom donors (phenols and water).

Competition among decay processes such as fluorescence, phosphorescence, internal conversion, intersystem crossing, charge transfer, surface hopping and H-atom tunneling ultimately determine the overall reaction efficiency. Understanding how to manipulate the branching ratios among these excited-state relaxation pathways is likely the key to directing reactivity in photochemical transformations such as CO_2 reduction,[77] water remediation,[78-79] acid/base photochemistry,[80-81] and artificial photosynthesis.[82]

1.4 PHOTOPHYSICAL CHARACTERIZATION OF TAHZ

To attempt to understand the dynamics controlling aza-aromatic photochemistry, the Schlenker lab synthesized and studied 2,5,8-tris(4-methoxyphenyl)-1,3,4,6,7,9,9b-heptaazaphenalene (TAHz), a molecular photocatalyst structurally related to carbon nitride.[83] The structure and ground state absorption spectrum of TAHz are shown in Figure 1-3.

We spectrally and kinetically resolved a new photoluminescent (PL) feature which was blue shifted from the steady state emission.[83] Importantly, this feature shows a fast decay component with a kinetic isotope effect (KIE) of 2.9, whereas the long-lived PL feature shows negligible isotopic dependence. From *ab initio* electronic-structure calculations, we attribute this new PL feature to the fluorescence of an upper singlet excited state of mixed $n\pi^*/\pi\pi^*$ character. The KIE of the PL suggests that this excited state is quenched by PCET. Correspondingly, our radical detection measurements with terephthalic acid as a hydroxyl radical scavenger confirms that OH radicals form when TAHz is illuminated in water. These findings are consistent with recent theoretical predictions that heptazine-based photocatalysts can participate in excited-state PCET with water.[67-68]

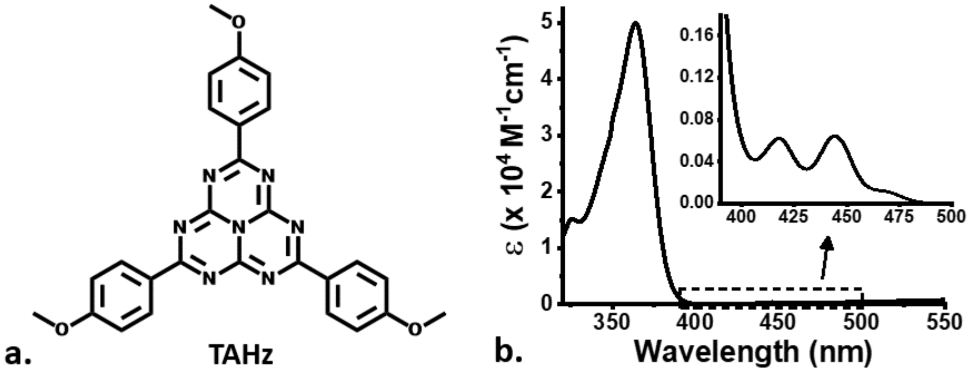

Figure 1-3. **S**tructure and ground-state absorption spectrum of 2,5,8-tris(4-methoxyphenyl)-1,3,4,6,7,9,9b-heptaazaphenalene (TAHz).

Further studies contained herein with TAHz showed PCET with a series of six para-substituted phenol derivatives.[84] Phenol was used as the H-atom donor since TAHz is more soluble in toluene compared to water. Furthermore, it is easy to change the oxidation potential of the H-atom donor with the para-substitution of electron donating or withdrawing groups onto phenol. We determined association constants (K_A), excited state quenching rate constants (k_Q), KIE, and transition-state barriers ($\Delta E^{\ddagger}$). The phenols with more electron donating character have higher pKa's and a lower (more cathodic) oxidation potential. As the electron donating character increased, we measure increased k_Q, higher radical generation rates, lowered Ka, and lowered KIEs. Theoretically, in the case of methoxyphenol and TAHz, we showed there is no barrier to access the charge transfer state from the lowest lying hydrogen-bound excited state, which explains the above trends.

To dig even deeper into the photochemical reactivity of TAHz, we examined the intermolecular hydrogen-bonded complexes of TAHz with four phenol derivatives using ultrafast multi-pulse pump-push-probe transient absorption spectroscopy. We utilize pump-push-probe spectroscopy to monitor the role of mixed $n\pi^*/\pi\pi^*$ states comprising TAHz and phenolic orbitals in facilitating excited-state H-atom transfer to TAHz. Following the initial ultraviolet excitation (365 nm), we "push" into a higher-lying excited state with a NIR laser pulse (1150 nm). When phenol is present, the push induces a persistent decrease (ΔΔOD) in the initial excited-state absorption, indicating that the push pulse engenders a divergence in the photochemical branching ratios. Furthermore, in the presence of electron-donating substituted phenols, the magnitude of ΔΔOD diminishes markedly due to the increased excited-state reactivity of the complex that accompanies the cathodic shift in the phenol oxidation potential. Thus, the H-atom abstraction proceeds without aid from the additional energy of the push pulse. These results reveal new insight into the branching ratio among unreactive localized heptazine upper excited states and reactive intermolecular charge transfer states of H-bonded heptazine chromophores.

From this data we provide a generalizable picture of hydrogen-bond formation and excited-state reactivity of heptazine-based materials with H-atom donating molecules such as phenol and water, which will be discussed further in Chapters 4 and 5. This data suggests design rules for future heptazine-based materials for solar energy collection and storage. Tuning the functionalization of the heptazine core to have electron withdrawing groups presumably will shift the charge transfer curve of water to fall near the lowest lying hydrogen-bound state of the heptazine-water complex. Additional modifications to the heptazine core should include adding solubilizing moieties and bulkier, potentially aromatic, groups to extend the conjugation and the light absorption further into the solar spectrum.

In addition to PCET seen between TAHz and water or phenol, we also see comparable hydrogen evolution to that of graphitic carbon nitride with the addition of an electron donor/hole acceptor (triethanolamine). This distinct mechanism is much more well understood than that of excited state PCET reactions with heptazine-based molecules. However, the more interesting and impactful question is to study if organic photocatalysts can generate hydrogen without the need for an electron donor (i.e. full water splitting). If organic, particle-based, photocatalytic systems become ~10% efficient, it could be possible to reach the Department of Energy's goal of $2 per gallon of gasoline equivalent.[85]

1.5 REFERENCES

1. Office of Energy Efficiency & Renewable Energy: Solar Energy Technology Basics. https://www.energy.gov/eere/solar/articles/solar-energy-technology-basics.
2. Office of Energy Efficiency & Renewable Energy: New Solar Opportunities for a New Decade. https://www.energy.gov/eere/solar/sunshot-2030.
3. Laboratory, N. R. E. Best Research-Cell Efficiency Chart. https://www.nrel.gov/pv/cell-efficiency.html.
4. Jones-Albertus, B. Confronting the Duck Curve: How to Address Over-Generation of Solar Energy. https://www.energy.gov/eere/articles/confronting-duck-curve-how-address-over-generation-solar-energy.
5. Kalisman, P., et al., Perfect Photon-to-Hydrogen Conversion Efficiency. *Nano Lett.* **2016,** *16* (3), 1776-1781.
6. Seger, B., et al., Using TiO2 as a Conductive Protective Layer for Photocathodic H2 Evolution. *J. Am. Chem. Soc.* **2013,** *135* (3), 1057-1064.

7. Roske, C. W., et al., Comparison of the Performance of CoP-Coated and Pt-Coated Radial Junction n+p-Silicon Microwire-Array Photocathodes for the Sunlight-Driven Reduction of Water to H2(g). *Journal of Physical Chemistry Letters* **2015,** *6* (9), 1679-1683.

8. Warren, E. L., et al., Hydrogen-evolution characteristics of Ni-Mo-coated, radial junction, n+p-silicon microwire array photocathodes. *Energ. Environ. Sci.* **2012,** *5* (11), 9653-9661.

9. Kudo, A.; Miseki, Y., Heterogeneous photocatalyst materials for water splitting. *Chem. Soc. Rev.* **2009,** *38* (1), 253-278.

10. Kato, H., et al., Highly Efficient Water Splitting into H2 and O2 over Lanthanum-Doped NaTaO3 Photocatalysts with High Crystallinity and Surface Nanostructure. *J. Am. Chem. Soc.* **2003,** *125* (10), 3082-3089.

11. Kamat, P. V.; Christians, J. A., Solar Cells versus Solar Fuels: Two Different Outcomes. *J. Phys. Chem. Lett.* **2015,** *6* (10), 1917-1918.

12. Yang, X., et al., Mechanistic Studies of Electrode-Assisted Catalytic Oxidation by Flavinium and Acridinium Cations. *ACS Catal.* **2014,** *4* (8), 2635-2644.

13. Mirzakulova, E., et al., Electrode-assisted catalytic water oxidation by a flavin derivative. *Nature chemistry* **2012,** *4* (10), 794-801.

14. Lau, V. W., et al., Low-molecular-weight carbon nitrides for solar hydrogen evolution. *J. Am. Chem. Soc.* **2015,** *137* (3), 1064-72.

15. Schwinghammer, K., et al., Phenyl-triazine oligomers for light-driven hydrogen evolution. *Energ. Environ. Sci.* **2015,** *8* (Copyright (C) 2016 American Chemical Society (ACS). All Rights Reserved.), 3345-3353.

16. Li, L., et al., Photocatalysts Based on Cobalt-Chelating Conjugated Polymers for Hydrogen Evolution from Water. *Chem. Mater.* **2016,** *28* (15), 5394-5399.

17. Li, L., et al., Rational Design of Porous Conjugated Polymers and Roles of Residual Palladium for Photocatalytic Hydrogen Production. *J. Am. Chem. Soc.* **2016,** *138* (24), 7681-7686.

18. Yanagida, S., et al., Poly(p-phenylene)-catalysed photoreduction of water to hydrogen. *J. Chem. Soc., Chem. Commun.* **1985,** (8), 474-475.

19. Shibata, T., et al., Novel visible-light-driven photocatalyst. Poly(p-phenylene)-catalyzed photoreductions of water, carbonyl compounds, and olefins. *J. Phys. Chem.* **1990,** *94* (5), 2068-2076.

20. Sprick, R. S., et al., Visible-Light-Driven Hydrogen Evolution Using Planarized Conjugated Polymer Photocatalysts. *Angew. Chem., Int. Ed.* **2016,** *55* (5), 1792-6.

21. Xinchen, W., et al., A metal-free polymeric photocatalyst for hydrogen production from water under visible light. *Nat. Mater.* **2009,** *8,* 76-80.

22. Maeda, K., et al., Photocatalytic Activities of Graphitic Carbon Nitride Powder for Water Reduction and Oxidation under Visible Light. *J. Phys. Chem. C* **2009,** *113* (Copyright (C) 2016 American Chemical Society (ACS). All Rights Reserved.), 4940-4947.

23. Jun, Y.-S., et al., Mesoporous, 2D Hexagonal Carbon Nitride and Titanium Nitride/Carbon Composites. *Advanced Materials* **2009,** *21* (Copyright (C) 2016 American Chemical Society (ACS). All Rights Reserved.), 4270-4274.

24. Xiang, Q.; Yu, J., Graphene-Based Photocatalysts for Hydrogen Generation. *J. Phys. Chem. Lett.* **2013,** *4* (5), 753-759.

25. Zhao, C., et al., A novel composite of TiO2 nanotubes with remarkably high efficiency for hydrogen production in solar-driven water splitting. *Energy & Environmental Science* **2014,** *7* (5), 1700-1707.
26. Liebig, J., Uber einige Stickstoff - Verbindungen. *Annalen der Pharmacie* **1834,** *10* (1), 1-47.
27. Liu, J., et al., Metal-free efficient photocatalyst for stable visible water splitting via a two-electron pathway. *Science* **2015,** *347* (6225), 970-4.
28. Wang, W., et al., g-C3N4 quantum dots: direct synthesis, upconversion properties and photocatalytic application. *Chemical Communications* **2014,** *50*, 10148-10150.
29. Zhang, H., et al., Pyridine derivative/graphene nanoribbon composites as molecularly tunable heterogeneous electrocatalysts for the oxygen reduction reaction. *Phys Chem Chem Phys* **2016,** *18* (6), 5040-7.
30. Liu, J., et al., Self-regenerated solar-driven photocatalytic water-splitting by urea derived graphitic carbon nitride with platinum nanoparticles. *Chem. Commun.* **2012,** *48* (70), 8826-8828.
31. Xu, J., et al., Eosin Y-sensitized graphitic carbon nitride fabricated by heating urea for visible light photocatalytic hydrogen evolution: the effect of the pyrolysis temperature of urea. *Phys. Chem. Chem. Phys.* **2013,** *15* (20), 7657-65.
32. Huang, J., et al., Metal-free disinfection effects induced by graphitic carbon nitride polymers under visible light illumination. *Chem. Commun.* **2014,** *50* (33), 4338-40.
33. Zheng, Y., et al., Graphitic Carbon Nitride Polymers toward Sustainable Photoredox Catalysis. *Angew. Chem., Int. Ed.* **2015,** *54* (Copyright (C) 2016 American Chemical Society (ACS). All Rights Reserved.), 12868-12884.

34. Chen, Y.; Qin, Z., General applicability of nanocrystalline Ni2P as a noble-metal-free cocatalyst to boost photocatalytic hydrogen generation. *Catal. Sci. Technol.* **2016,** *6* (23), 8212-8221.

35. Li, C., et al., Unique P-Co-N Surface Bonding States Constructed on g-C3N4 Nanosheets for Drastically Enhanced Photocatalytic Activity of H2 Evolution. *Advanced Functional Materials* **2017,** *27* (4), 1604328.

36. Hou, Y., et al., Layered Nanojunctions for Hydrogen-Evolution Catalysis. *Angew. Chem., Int. Ed.* **2013,** *52* (13), 3621-3625.

37. Kasap, H., et al., Solar-Driven Reduction of Aqueous Protons Coupled to Selective Alcohol Oxidation with a Carbon Nitride-Molecular Ni Catalyst System. *J Am Chem Soc* **2016,** *138* (29), 9183-92.

38. Franklin, E. C., THE AMMONO CARBONIC ACIDS. *Journal of the American Chemical Society* **1922,** *44* (3), 486-509.

39. Liebig, J., Ueber die Constitution der Mellonverbindungen. *Justus Liebigs Annalen der Chemie* **1855,** *95* (3), 257-282.

40. Miller, T. S., et al., Carbon nitrides: synthesis and characterization of a new class of functional materials. *Physical Chemistry Chemical Physics* **2017,** *19* (24), 15613-15638.

41. Pauling, L.; Sturdivant, J. H., The Structure of Cyameluric Acid, Hydromelonic Acid and Related Substances. *Proceedings of the National Academy of Sciences* **1937,** *23* (12), 615-620.

42. Hosmane, R. S., et al., Synthesis and structure of tri-s-triazine. *Journal of the American Chemical Society* **1982,** *104* (20), 5497-5499.

43. Teter, D. M.; Hemley, R. J., Low-compressibility carbon nitrides. *Science* **1996,** *271* (5245), 53-55.

44. Goettmann, F., et al., Chemical synthesis of mesoporous carbon nitrides using hard templates and their use as a metal-free catalyst for Friedel-Crafts reaction of benzene. *Angew Chem Int Ed Engl* **2006,** *45* (27), 4467-71.

45. Ong, W. J., et al., Graphitic Carbon Nitride (g-C3N4)-Based Photocatalysts for Artificial Photosynthesis and Environmental Remediation: Are We a Step Closer To Achieving Sustainability? *Chem Rev* **2016,** *116* (12), 7159-329.

46. Liu, J., et al., Self-regenerated solar-driven photocatalytic water-splitting by urea derived graphitic carbon nitride with platinum nanoparticles. *Chem. Commun.* **2012,** *48* (70), 8826-8.

47. Xu, J., et al., Eosin Y-sensitized graphitic carbon nitride fabricated by heating urea for visible light photocatalytic hydrogen evolution: the effect of the pyrolysis temperature of urea. *Phys Chem Chem Phys* **2013,** *15* (20), 7657-65.

48. Huang, J., et al., Metal-free disinfection effects induced by graphitic carbon nitride polymers under visible light illumination. *Chem Commun (Camb)* **2014,** *50* (33), 4338-40.

49. Zheng, Y., et al., Graphitic Carbon Nitride Polymers toward Sustainable Photoredox Catalysis. *Angew Chem Int Ed Engl* **2015,** *54* (44), 12868-84.

50. Koryakin, A., et al., Thermography of urea and its pyrolysis products. *Zhurnal Organicheskoi Khimii* **1971,** *7* (5), 972-&.

51. Khabashesku, V. N., et al., Powder synthesis and characterization of amorphous carbon nitride. *Chemistry of Materials* **2000,** *12* (11), 3264-3270.

52. Merschjann, C., et al., Photophysics of polymeric carbon nitride: An optical quasimonomer. *Physical Review B* **2013,** *87* (20).

53. Zhang, H.; Yu, A., Photophysics and Photocatalysis of Carbon Nitride Synthesized at Different Temperatures. *J. Phys. Chem. C* **2014,** *118* (22), 11628-11635.

54. Zhang, H., et al., Charge carrier kinetics of carbon nitride colloid: a femtosecond transient absorption spectroscopy study. *Phys Chem Chem Phys* **2016,** *18* (22), 14904-10.

55. Ye, C., et al., Enhanced Driving Force and Charge Separation Efficiency of Protonated g-C3N4 for Photocatalytic O2 Evolution. *ACS Catal.* **2015,** *5* (11), 6973-6979.

56. Corp, K. L.; Schlenker, C. W., Ultrafast Spectroscopy Reveals Electron-Transfer Cascade That Improves Hydrogen Evolution with Carbon Nitride Photocatalysts. *J. Am. Chem. Soc.* **2017,** *139* (23), 7904-7912.

57. Kellmann, A.; Dubois, J. T., Photoreactive State of Acridine in Solution. *J. Chem. Phys.* **1965,** *42* (7), 2518-2522.

58. Whitten, D. G.; Lee, Y. J., Photochemistry of aza aromatics. Identification of the reactive intermediate in the photoreduction of acridine. *J. Am. Chem. Soc.* **1971,** *93* (4), 961-966.

59. Kikuchi, K., et al., Reaction and deactivation of excited acridine in ethanol. *J. Phys. Chem.* **1985,** *89* (5), 868-871.

60. Donckt, E. V.; Porter, G., Role of the 3(n—π*) State in the Photoreduction of Acridine. *J. Chem. Phys.* **1967,** *46* (3), 1173-1175.

61. Wilkinson, F.; Dubois, J. T., Reactive State in the Photoreduction of Acridine in Ethanol. *J. Chem. Phys.* **1968,** *48* (6), 2651-2654.

62. Koizumi, M., et al., Reactive State of Acridine in the Photoreduction in Alcohols. *J. Chem. Phys.* **1968,** *48* (4), 1869-1870.

63. Stermitz, F. R., et al., Photochemistry of n-heterocycles. V. Photochemistry of quinoline and some substituted quinoline derivatives. *J. Am. Chem. Soc.* **1970,** *92* (9), 2745-2752.

64. Whitten, D. G.; Lee, Y. J., Reactions of Hidden n, π* Excited States in N-Heteroaromatics. Photoreduction and Photoaddition. *J. Am. Chem. Soc.* **1970,** *92* (2), 415-416.

65. Eisenhart, T. T.; Dempsey, J. L., Photo-induced Proton-Coupled Electron Transfer Reactions of Acridine Orange: Comprehensive Spectral and Kinetics Analysis. *J. Am. Chem. Soc.* **2014,** *136* (35), 12221-12224.

66. Liu, X., et al., Photocatalytic Water Splitting with the Acridine Chromophore: A Computational Study. *J. Phys. Chem. B* **2015,** *119* (33), 10664-10672.

67. Ehrmaier, J., et al., Mechanism of Photocatalytic Water Splitting with Graphitic Carbon Nitride: Photochemistry of the Heptazine-Water Complex. *J. Phys. Chem. A* **2017,** *121* (25), 4754-4764.

68. Ehrmaier, J., et al., Mechanism of photocatalytic water splitting with triazine-based carbon nitrides: insights from ab initio calculations for the triazine-water complex. *Phys. Chem. Chem. Phys.* **2018,** *20* (21), 14420-14430.

69. Concepcion, J. J., et al., Excited-State Quenching by Proton-Coupled Electron Transfer. *Journal of the American Chemical Society* **2007,** *129* (22), 6968-6969.

70. Lennox, J. C., et al., Excited-State Proton-Coupled Electron Transfer: Different Avenues for Promoting Proton/Electron Movement with Solar Photons. *ACS Ener. Lett.* **2017,** *2* (5), 1246-1256.

71. Weinberg, D. R., et al., Proton-Coupled Electron Transfer. *Chem. Rev.* **2012,** *112* (7), 4016-4093.

72. Gagliardi, C. J., et al., The role of proton coupled electron transfer in water oxidation. *Energy & Environmental Science* **2012,** *5* (7), 7704-7717.

73. Oliver, T. A. A., et al., Exploring Autoionization and Photoinduced Proton-Coupled Electron Transfer Pathways of Phenol in Aqueous Solution. *The Journal of Physical Chemistry Letters* **2015,** *6* (20), 4159-4164.

74. Damrauer, N. H., et al., Observation of Proton-Coupled Electron Transfer by Transient Absorption Spectroscopy in a Hydrogen-Bonded, Porphyrin Donor−Acceptor Assembly. *Journal of Physical Chemistry B* **2004,** *108* (20), 6315-6321.

75. Liu, X., et al., Photocatalytic Water Splitting with the Acridine Chromophore: A Computational Study. *Journal of Physical Chemistry B* **2015,** *119* (33), 10664-72.

76. Reimers, J. R.; Cai, Z.-L., Hydrogen bonding and reactivity of water to azines in their S1 (n,pi*) electronic excited states in the gas phase and in solution. *Physical Chemistry Chemical Physics* **2012,** *14* (25), 8791-8802.

77. Wang, S.; Wang, X., Imidazolium Ionic Liquids, Imidazolylidene Heterocyclic Carbenes, and Zeolitic Imidazolate Frameworks for CO2 Capture and Photochemical Reduction. *Angew. Chem. Int. Ed.* **2016,** *55* (7), 2308-2320.

78. Kumar, S., et al., Two-dimensional carbon-based nanocomposites for photocatalytic energy generation and environmental remediation applications. *Beilstein J. Nanotech.* **2017,** *8*, 1571-1600.

79. Ong, W.-J., et al., Graphitic Carbon Nitride (g-C3N4)-Based Photocatalysts for Artificial Photosynthesis and Environmental Remediation: Are We a Step Closer To Achieving Sustainability? *Chem. Rev.* **2016,** *116* (12), 7159-7329.

80. Roy, S., et al., 5-Methoxyquinoline Photobasicity Is Mediated by Water Oxidation. *J. Phys. Chem. A* **2019,** *123* (31), 6645-6651.

81. Hunt, J. R.; Dawlaty, J. M., Photodriven Deprotonation of Alcohols by a Quinoline Photobase. *The Journal of Physical Chemistry A* **2018,** *122* (40), 7931-7940.

82. Wasielewski, M. R., Photoinduced electron transfer in supramolecular systems for artificial photosynthesis. *Chem. Rev.* **1992,** *92* (3), 435-461.

83. Rabe, E. J., et al., Proton-Coupled Electron Transfer from Water to a Model Heptazine-Based Molecular Photocatalyst. *J. Phys. Chem. Lett.* **2018,** *9* (21), 6257-6261.

84. Rabe, E. J., et al., Barrierless Heptazine-Driven Excited-State Proton-Coupled Electron Transfer: Implications for Controlling Photochemistry of Carbon Nitrides and Aza-Arenes. *J. Phys. Chem. C.* **2019,** *10.1021/acs.jpcc.9b08842*.

85. Pinaud, B. A., et al., Technical and economic feasibility of centralized facilities for solar hydrogen production via photocatalysis and photoelectrochemistry. *Energy & Environmental Science* **2013,** *6* (7), 1983-2002.

Chapter 2. Background

2.1 PHOTOEXCITATION RESULTS

When using spectroscopy to understand an excited state landscape and its dynamics, one must first understand what types of features may be observable and how they may be distinguished. Often in transient spectroscopy, features will overlap which makes understanding the spectra features and kinetics significantly more difficult. More information on getting around that can be found in Section 2.5: Global Analysis.

The Lanzani text *The Photophysics behind Photovoltaics and Photonics* has a section devoted to “The Excitation Zoo in Molecular Semiconductors,” in which Lanzani details the aftermath of photo-excitations in molecular semiconductors.[1] After excitation, there are dozens of results that could happen and they often interact with one another. A few worth noting are the free charge, the exciton, and a charge transfer state.

A free charge is localized in space but can easily propagate in a crystalline solid as a wavepacket since it is not tied to an atom or location in the crystal lattice. Frequently, free carriers become trapped carriers due to structural defects or lower lying forbidden transitions. Spectroelectrochemistry is often a great way to determine spectroscopic features for charge carriers. In this technique, one first needs to find the redox potential of interest for the active species. After a proper cyclic voltammogram has been taken, the redox potential is held constant (chronoamperometry) while absorption spectra are taken periodically (every few seconds or minutes depending on the system). If the system is sensitive to degradation during the course of this measurement, alternating cyclic voltammetry can be utilized. This technique was made possible in our laboratory by Timothy Pollock and the details of the procedure can be found in his thesis and manuscript.[2]

An exciton is a bound electron-hole pair, attracted by coulombic forces. In organic materials, excitons can have binding energy as large as 1.5 eV. This means before the individual charges can be used productively, in a solar cell for instance, there must be additional energy provided to the system to overcome the binding energy.[3] Therefore one must be careful in comparing ground state ionization potentials and electron affinities since the excited state landscape could be far different. Rabe and Schlenker go in detail with best practices for estimating the excited state energy levels in their recent book chapter.[3]

A charge transfer state is a state in which a fraction of ionic character has shifted either within a single molecule (donor-acceptor type molecules) or between two initially discrete molecules. Compared to an exciton, a charge transfer state has more ionic character and thus has a larger static dipole. Charge transfer states can often be identified by a new induced absorption feature or a new luminescent feature. Occasionally, the charge transfer state even has a ground state absorption depending on the degree to which the transition is allowed.

Charge transfer states and localized excited states can be singlet or triplet in nature. The distinction is the pairings of spins present. A singlet excited state only has a single option for the pairing of spins – one “up” electron and one “down” electron. This state generally has a lifetime on the order of picoseconds to nanoseconds. A triplet excited state has three electron pairings. The best representation of these options is by using a spin diagram, like the one seen in Figure 2-1. Triplet states are generally much longer lived than singlet states, on the order of hundreds of nanoseconds to milliseconds or even minutes. These states can interconvert depending on the energy and the nature of the state, this process is called intersystem crossing.

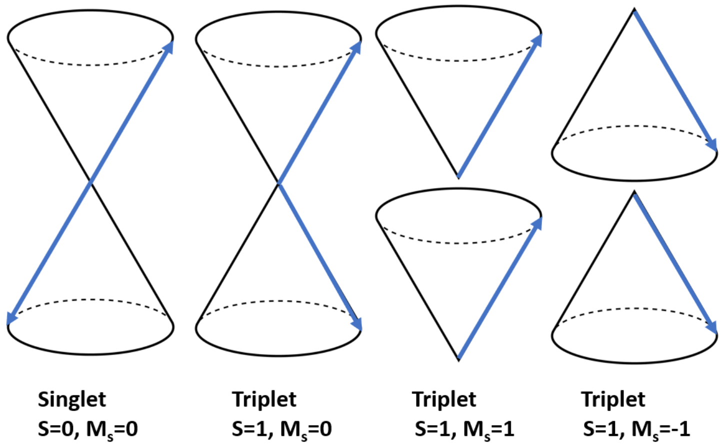

Figure 2-1. A spin diagram denoting singlet and triplet states.

2.2 Time-Resolved Photoluminescence

Time-resolved photoluminescence (TR-PL) is a helpful technique to characterize the rates of formation and decay of luminescent states in a given system. Kasha's rule says emission will happen from the lowest lying state, however, on the femtosecond to picosecond timescale, emission can be seen from higher lying states not just the lowest lying emissive state. Additionally, time resolution for luminescence can assist in the characterization of trapped charge carrier luminescence, intersystem crossing to a triplet state (therefore watching the phosphorescence), or thermally activated delayed fluorescence. None of these different types of relaxation pathways can be seen with steady-state luminescence measurements.

Time-resolved luminescence measurement techniques are often performed in two ways: time-correlated single photon counting (TCSPC) or using a streak camera. In TCSPC, a laser diode is used to excite the sample and a filter is used to cut out the excitation wavelengths (which can also cut out some luminescence if the Stokes shift is small) and the luminescence is collected. Depending on the system of interest, this relatively simple technique can provide enough information to characterize the radiative decay. However, since the photons are not spread over a grating, this technique provides limited spectral resolution. As such, it can provide an incomplete picture of the luminescence characteristics of the system that may, in some cases, lead the researcher to incorrect conclusions about the excited state landscape. For instance, if the luminescence spectrum is not resolved and photons are collected at all wavelengths longer than that of the excitation light, one could not distinguish between emission arising from native states of the material vs. emission from low-energy trap states. Additionally, if the luminescence has a lifetime shorter than a nanosecond, TCSPC is not advised used due to the long instrument response function (>300 ps).

A streak camera (Figure 2-2) can allow for spectral detection over time and higher time resolution compared to TCSPC. The data collected in this work was taken by pumping with a roughly 50 fs pulses and collecting with a Hamamatsu streak camera (details in Chapter 3 materials and methods section). A streak camera collects light with a wide range of energies (200-300 nm) dispersed onto a grating to get the spectral response. The streak tube is referenced to the rep rate of the laser (80 MHz laser, 1 kHz pump in our case), the photons are turned into electrons on the photocathode and voltage is swept over the desired time range to delay electrons variably giving time resolution. The electrons hit a phosphor screen resulting in an image that can be capture using a charge coupled device (CCD) camera. This process is repeated until the desired signal-to-noise ratio is achieved. Example data can be seen in Figure 2-3.

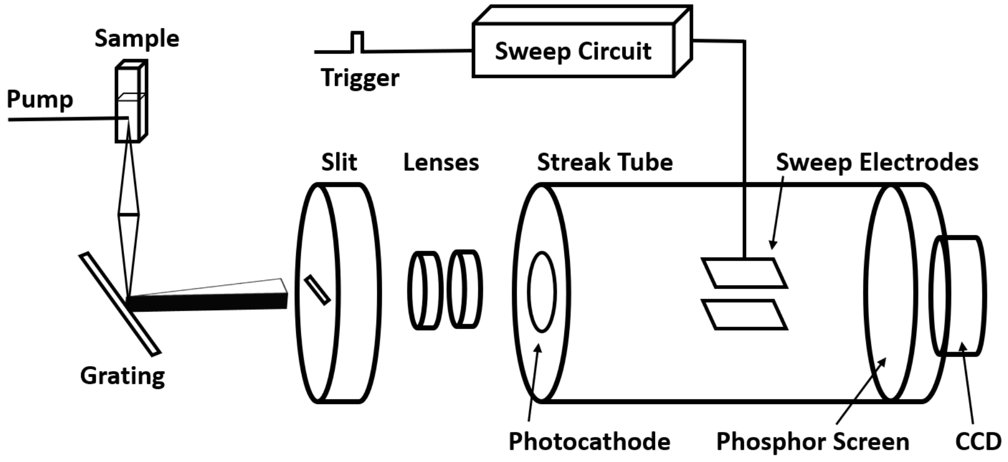

Figure 2-2. Streak camera diagram depicting spectral resolution using a grating and temporal resolution using a voltage sweep circuit.

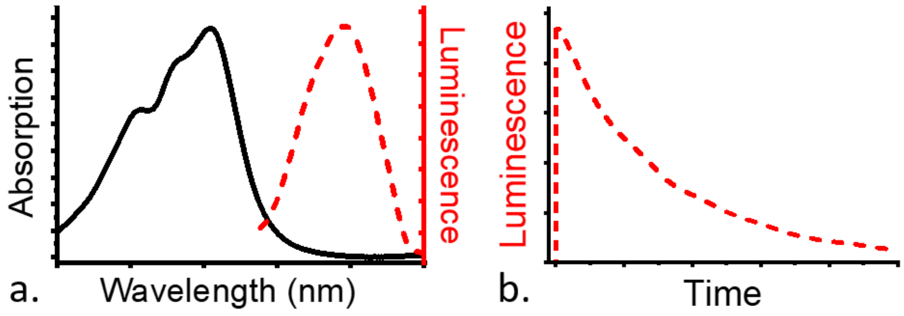

Figure 2-3. Example of time-resolved photoluminescence (a) spectra and (b) kinetics.

Two types of streak tubes are generally used – one for the nanosecond to millisecond time range (called the Slow Sweep unit) and one for the picosecond to nanosecond time range (called the Synchroscan). On the Synchroscan, the voltage is swept continuously between pulses – forward to collect data and backward while clearing the phosphor screen. If the radiative species has not entirely relaxed after half the time between pulses of the laser (6.25 ns in our system) the data will be convoluted with the tail of the luminescence. This problem can be overcome with a pulse picker (also known as a shift blanking unit) which allows laser pulses to be skipped and thus the radiative species can fully relax before the next voltage sweep and data collection.

If the luminescence is spectrally evolving over time with multiple decay constants, global analysis can help pull out associated species (see section 2.5 Global Analysis below). Furthermore, low-temperature (cryogenic) TR-PL measurements can be extremely helpful when characterizing possible influence of excited state triplets playing a role in the luminescence as well as “freezing out” states to learn more about vibronic progression in the excited state and how it can influence relaxation pathways. Time-resolved measurements in general are paramount in characterizing the energy landscape of a system and the mechanisms that ensue after photon absorption.

2.3 TRANSIENT ABSORPTION SPECTROSCOPY

Transient absorption spectroscopy is a well-established technique in which a pump pulse, generally a single color, causes a non-equilibrium state (an excited state) and a probe pulse, generally a broad spectrum of light, comes later in time to monitor changes in the sample’s transmission induced by the pump pulse. This technique provides complementary information to time-resolved photoluminescence as it can monitor species that are radiative and non-radiative. A general schematic for the setup is shown in Figure 2-4. These beams are focused and spatially overlapped. The probe pulse is on a physical or electronic delay line to get kinetic information about the way the new excited state is evolving. Data is collected and plotted as the differential optical density $\Delta OD = \log_{10} [I_{0\ sample}/I_{ex\ sample} \times I_{ex\ ref}/I_{0\ ref}]$, where I is the intensity of the transmission of either the initial (ground state) or the excited state of the sample. In this setup there is a reference probe beam to account for fluctuations during the data collection. The signal intensity is the difference between the pump on and the pump off.

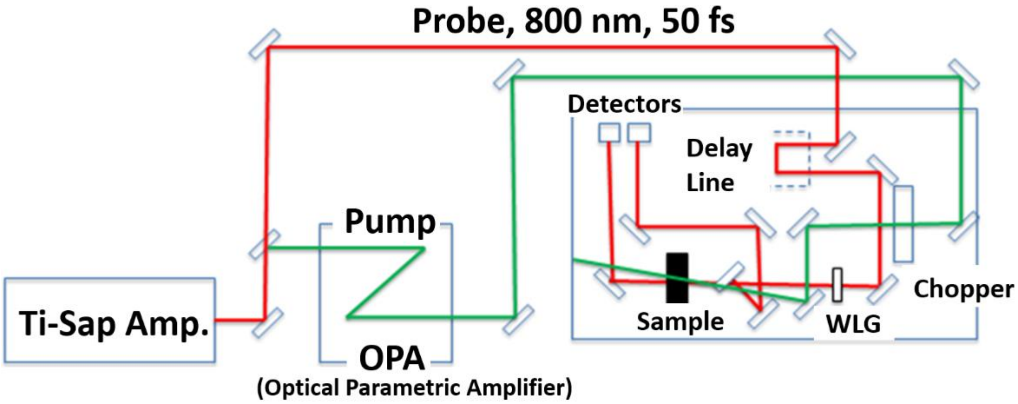

Figure 2-4. Schematic of pump-probe transient absorption spectroscopy.
This setup contains a delay line for temporal resolution on the femtosecond timescale, white light generation (WLG) on calcium fluoride or sapphire plates, and two detectors – one for the probe light passing through the sample and the other as a reference to account for fluctuations in the probe intensity over the course of the measurement.

The resulting signal could include a ground state bleach, stimulated emission, and/or an induced absorption as seen in Figure 2-5. The ground state bleach represents absorption of the pump by the chromophore causing an excited state. Once a chromophore is in the excited state, it no longer absorbs the same energies as it did in the ground state and therefore the detector sees more light at the ground state absorption energies causing the bleach feature (negative signal if plotted as -ΔT/T where T is transmission). If stimulated emission is present in the transient absorption signal, it will be close to the same energy as spontaneous luminescence and the signal will have the same sign as the ground state bleach since the detector is sees light than before the pump pulse.

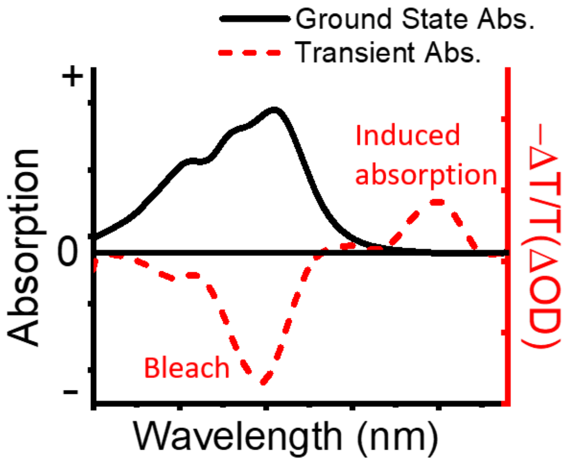

Figure 2-5. Example of transient absorption data overlaid with ground state absorption.

2.4 PUMP-PUSH-PROBE SPECTROSCOPY

Recently pump-push-probe spectroscopy has been utilized by a number of authors to monitor charge separation dynamics in organic materials often used in solar cells.[4-11] Such results have demonstrated that photocurrent generation efficiency is governed by access to delocalized intermolecular charge separated states. In the case of thin-film heterojunction organic solar cells, the role of the push pulse is to impart additional energy to overcome the activation barrier for accessing the delocalized charge separated states. In the context of photochemical reactivity, pump-push-probe spectroscopy allows us to infer information concerning the role of the mixed $n\pi^*$ excitations of the H-bonded complex in propelling the system toward the reactive CT state excitation.

Pump-push-probe spectroscopy is comparatively less common than pump-probe spectroscopy (above). However, the two techniques are generally performed in a similar fashion, just with the addition of a third pulse, the push (see Figure 2-6). Predicting the state to which an excited state absorbs is challenging without detailed computational work or additional supporting characterization techniques. In pump-push-probe spectroscopy, one must consider the state to which the excited state is absorbing, and furthermore, where that new excited state absorbs. This approach allows one to probe compelling questions such as, “Do new reactions ensue due to the energy of this higher lying excited state?” “What do the new charge dynamics mean for the upper excited state manifold?”

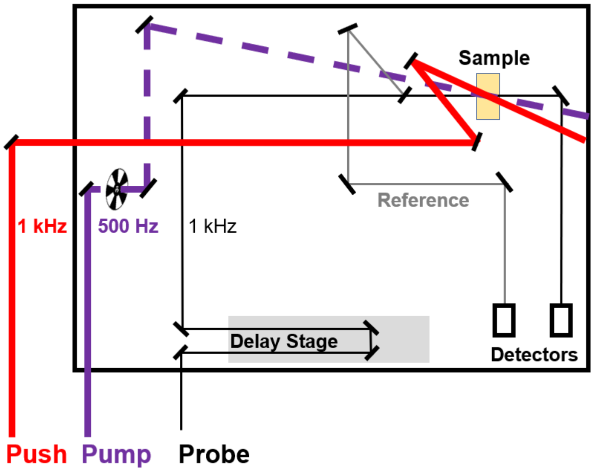

Figure 2-6. Schematic of pump-push-probe spectroscopy.
The pump pulse (500 Hz) is first incident on the sample, followed by the push pulse (1 kHz). The probe pulse (1 kHz) is on an adjustable delay stage and measures the change in absorption before and after the pump and push pulses. There is a reference detector accounting for the fluctuations in the probe power over the course of the measurement.

2.5 GLOBAL ANALYSIS

Global analysis is used to kinetically resolve overlapping spectral features with differing temporal decay constants, an example is shown in Figure 1-1Figure 2-7. The overall spectrum, $\psi(t,\lambda)$, is assumed to be a function of a time-dependent concentration of the associated species, $c_i(t)$, and a wavelength-dependent spectrum, $\sigma_i(\lambda)$, for the i^{th} species, such that $\psi(t,\lambda) =$

$\sum c_i(t)\sigma_i(\lambda)$. The resulting spectral traces are called species associated difference spectra, SADS. In this work, global and target analysis were performed using Glotaran,[12] a graphical user interface for the R-package TIMP.

If spectral features overlap and have different decay constants (roughly an order of magnitude or more different) global analysis can separate features. If the spectral features overlap and have similar decay constants, analysis requires a more targeted relaxation scheme combining the mechanisms for internal conversion and recombination post-excitation. This is call target analysis. It is worth noting that global and target analysis methods can give many possibilities for any one set of data, therefore without further characterization to assist in the modeling of the excited state relaxation mechanisms the results are not entirely meaningful. Some of the additional characterization methods to assist in the identification of legitimate mechanisms were time-resolved photoluminescence, spectro-electrochemistry, charge quenching experiments, and ground state absorption.

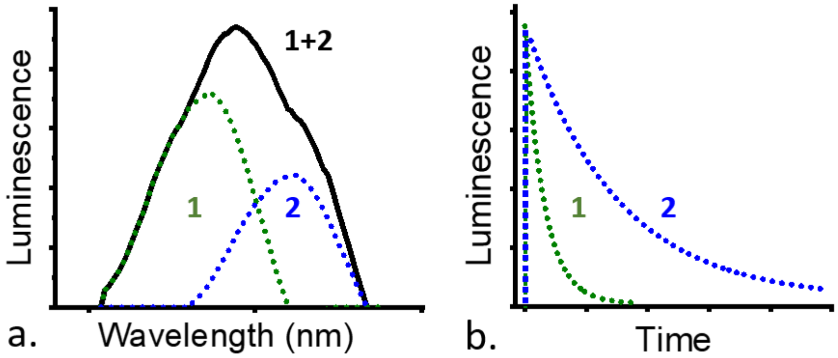

Figure 2-7. Example of (a) spectrally convoluted luminescence data, deconvoluted into two components with different (b) single exponential decays.

2.6 REFERENCES

1. Lanzani, G., *The Photophysics behind Photovoltaics and Photonics*. Wiley-VCH: 2012.
2. Pollock, T. P.; Schlenker, C. W., Electromodulation and Transient Absorption Spectroscopy Suggest Conduction Band Electron Lifetime, Electron Trapping Parameters, and CH3NH3PbI3 Solar Cell Fill Factor Are Correlated. *The Journal of Physical Chemistry C* **2019,** *123* (30), 18160-18170.
3. Rabe, E. J.; Schlenker, C. W., Excited-state Energies Drive Charge-transfer in Organic Semiconductors. In *World Scientific Handbook of Organic Optoelectronic Devices*, pp 89-120.
4. Bakulin, A. A., et al., The Role of Driving Energy and Delocalized States for Charge Separation in Organic Semiconductors. *Science* **2012,** *335* (6074), 1340-1344.
5. Bakulin, A. A., et al., Ultrafast Spectroscopy with Photocurrent Detection: Watching Excitonic Optoelectronic Systems at Work. *J. Phys. Chem. Lett.* **2016,** *7* (2), 250-258.
6. Dimitrov, S. D., et al., On the energetic dependence of charge separation in low-band-gap polymer/fullerene blends. *J. Am. Chem. Soc.* **2012,** *134* (44), 18189-92.
7. Mangold, H., et al., Control of charge generation and recombination in ternary polymer/polymer:fullerene photovoltaic blends using amorphous and semi-crystalline copolymers as donors. *Phys. Chem. Chem. Phys.* **2014,** *16* (38), 20329-20337.
8. Tan, Z. K., et al., Suppressing recombination in polymer photovoltaic devices via energy-level cascades. *Adv. Mater.* **2013,** *25* (30), 4131-8.
9. Zhang, J., et al., On the energetics of bound charge-transfer states in organic photovoltaics. *J. Mater. Chem. A* **2017,** *5* (23), 11949-11959.

10. Cabanillas-Gonzalez, J., et al., Pump-Probe Spectroscopy in Organic Semiconductors: Monitoring Fundamental Processes of Relevance in Optoelectronics. *Adv. Mater.* **2011,** *23* (46), 5468-5485.
11. Paternò, G. M., et al., Pump–Push–Probe for Ultrafast All-Optical Switching: The Case of a Nanographene Molecule. *Adv. Funct. Mater.* **2019,** *29* (21), 1805249.
12. Snellenburg, J. J., et al., Glotaran: A Java-Based Graphical User Interface for the R Package TIMP. *J. Stat. Softw.* **2012,** *49* (3), 22.

Chapter 3. Ultrafast Spectroscopy Reveals Electron Transfer Cascade that Improves Hydrogen Evolution with Carbon Nitride Photocatalysts

Reprinted (adapted) with permission from J. Am. Chem. Soc. 2017, 139, 23, 7904-7912.

3.1 INTRODUCTION

One attractive avenue for storing solar energy is to produce hydrogen fuel using photoinduced electron transfer in photocatalytic or photoelectrochemical water splitting. Inorganic materials systems such as cadmium chalcogenide nanostructures,[1-2] *pn* junction silicon,[3-5] and numerous metal oxides[6-7] exhibit activity toward hydrogen evolution. However, these all pose sustainability challenges due to either the cost/scarcity of the metal, risks for adverse environmental outcomes (e.g. Cd^{2+} released by photocorrosion), or inadequate scalability, which have limited their commercial development.[8] Carbon-based molecular species,[9-10] oligomers,[11-12] polymers,[13-17] and extended higher-dimensional structures[18-22] are receiving increasing attention as components in photocatalytic systems due to their potential for lower production costs, their low toxicity, and the ease with which they can be synthetically tailored from earth-abundant starting materials.

Carbon nitride, a heptazine-based polymer known since the early 19th century,[23] has recently shown promise for driving photocatalytic hydrogen evolution from water.[24-26] Interest in β-phase carbon nitride originated from its mechanical and chemical durability. For example, it was predicted to possess a hardness value rivaling that of diamond.[27] As a result, the electronic and catalytic properties of carbon nitride received little consideration until the graphitic phase was identified[28-29] as a chemically robust and environmentally benign catalyst. One particularly compelling quality of graphitic carbon nitride (g-C_3N_4) and its oligomers is that they can be easily prepared via pyrolysis of inexpensive and earth-abundant precursors, such as urea.[30-33] Their catalytic activity toward hydrogen evolution can also be significantly enhanced by non-noble metal[34-37] and metal-free[24] co-catalysts, circumventing the need for cost-prohibitive precious metals. Thus, their potential for low-cost production and their chemical stability make carbon nitrides appealing as scalable, clean energy conversion materials.

With mounting interest in 2D materials, such as graphene[38] and transition metal dichalcogenides,[39] chemically exfoliated 2D carbon nitride nanostructures have also garnered increasing attention.[11, 20, 25, 40-43] For example, Wang et al. observed an improvement in hydrogen activity when they added chemically exfoliated carbon nitride to bulk g-C_3N_4.[25] However, the underlying role that electron transfer dynamics play between bulk g-C_3N_4 and exfoliated carbon nitride in controlling the hydrogen evolution rate is still an open question.

Transient absorption (TA) and time-resolved photoluminescence (PL) spectroscopy are particularly well-suited techniques for assessing electron transfer kinetics in photochemical reactions.[44-49] While a select number of studies have employed such techniques to study carbon nitride,[37, 50-58] the influence of many fundamental photophysical processes, particularly photoinduced electron transfer, in controlling photocatalytic activity remain unclear. Based on time-resolved PL, the character of the luminescent states have been shown to be largely excitonic,[50] with lower pyrolysis temperatures resulting in larger interlayer stacking distances and longer PL lifetimes.[50-51] Recent ultrafast stimulated emission measurements suggest that singlet excitons can rapidly (within 200 fs) dissociate into polaron pairs across neighboring carbon nitride sheets.[52] Zhang et al.[53] and Ye et al.[54] have assigned spectra and kinetics of induced absorption features that they associated with singlet excitons and positive charge carriers on g-C_3N_4. Ye et al. additionally suggested that protonation introduces defects into carbon nitride that help promote longer charge separation lifetimes, resulting in higher oxygen evolution rates.[54] Lotsch et al. demonstrated that model heptazine-based oligomers with either oxidative terminations, secondary amines, or cyanamide moieties[11, 37, 43, 59] support improved hydrogen evolution activity. These findings imply that the photocatalytic activity of carbon nitride can be improved via photoinduced charging of chemically activated chain terminations, which appear to act as catalytic centers. Yet, a direct correlation between photocatalytic hydrogen activity and the kinetics of electron transfer from bulk g-C_3N_4 to chemically exfoliated carbon nitride has been elusive.

Here we use TA spectroscopy to correlate the excited state electron dynamics of carbon nitride with improvements that we observe in photocatalytic activity when we mix bulk g-C_3N_4 with chemically exfoliated carbon nitride, which possesses additional oxidative chain terminations. We find that when we introduce a small amount (10% by mass) of exfoliated carbon nitride into a suspension of g-C_3N_4, the hydrogen evolution rate nearly doubles, increasing from 2050 $\mu L\ h^{-1}g^{-1}$ for g-C_3N_4 alone to 3810 $\mu L\ h^{-1}g^{-1}$ for the mixture. Interestingly, exfoliated carbon nitride yields only trace levels of hydrogen (less than 44 $\mu L\ h^{-1}g^{-1}$) in the absence of bulk g-C_3N_4. Our TA measurements reveal that the absorption signal of electrons formed following photoexcitation of bulk g-C_3N_4 is precipitously quenched in the presence of exfoliated carbon nitride. This result suggests a cooperative electron cascade effect in which charge carriers form via exciton dissociation on photoexcited bulk g-C_3N_4,[52] followed by electron transfer to exfoliated carbon nitride. From this correlation, we conclude that our exfoliated carbon nitride possesses highly active catalytic sites, but evidently exfoliated carbon nitride does not sustain long-lived photoinduced charge carrier formation when compared with bulk g-C_3N_4 (Figure A-1). This new insight into the excited state dynamics of g-C_3N_4 helps to lay the groundwork for future structural designs aimed at tailoring the charge transfer kinetics and the activity of organic photocatalysts.

3.2 RESULTS AND DISCUSSION

We synthesize bulk g-C_3N_4 by thermal condensation of urea (Figure 3-1a).[60-62] From this material we prepare exfoliated carbon nitride using a mixture of sulfuric and nitric acids to modify the chain termination chemistry of the heptazine-polymer and to promote solubility (Figure 3-1a).[11, 20, 25, 40-41, 43, 59] We use ultrafast TA and time-resolved PL spectroscopies to clarify the origin of the increase in catalytic activity that we observe upon incorporating small quantities of exfoliated carbon nitride into colloidal suspensions of bulk g-C_3N_4 (Figure 3-1b).

In Figure 3-2a we show the ground-state absorption spectra of bulk g-C_3N_4 and exfoliated carbon nitride. (Figure A-2 shows the absorption spectra on a semi-log scale for reference.) Exfoliation blueshifts the absorption spectrum by approximately 10 nm, with an increase in the intensity of tail state absorption near 450 nm due to increased long-range structural disorder consistent with a slight line broadening of the X-ray diffraction peaks (Figure 3-2b).[63] The singlet exciton emission (Figure 3-2a) shows a significant blueshift (25 nm) and a slight decrease in fluorescence quantum efficiency from $\eta_f = 5.2\%$ to $\eta_f = 3.1\%$ upon exfoliation. The shift in emission is consistent with a decrease in local chromophore electronic coupling and the decrease in particle size, confirmed by the appearance of smaller regions of contrast by bright field transmission electron microscopy (TEM) in Figure A-3.

Our nitrogen 1s X-ray photoelectron spectroscopy (XPS) and Fourier Transform infrared (FTIR) data in Figure 3-2c and Figure 3-2d reveal the prevalence of oxidative chain terminations in our exfoliated carbon nitride samples. The XPS spectral envelope for bulk g-C_3N_4 contains peaks at 398.3, 399.8, and 400.8 eV that are indicative of C=N-C, N-$(C)_3$, and amine functionalities, respectively.[64-69]

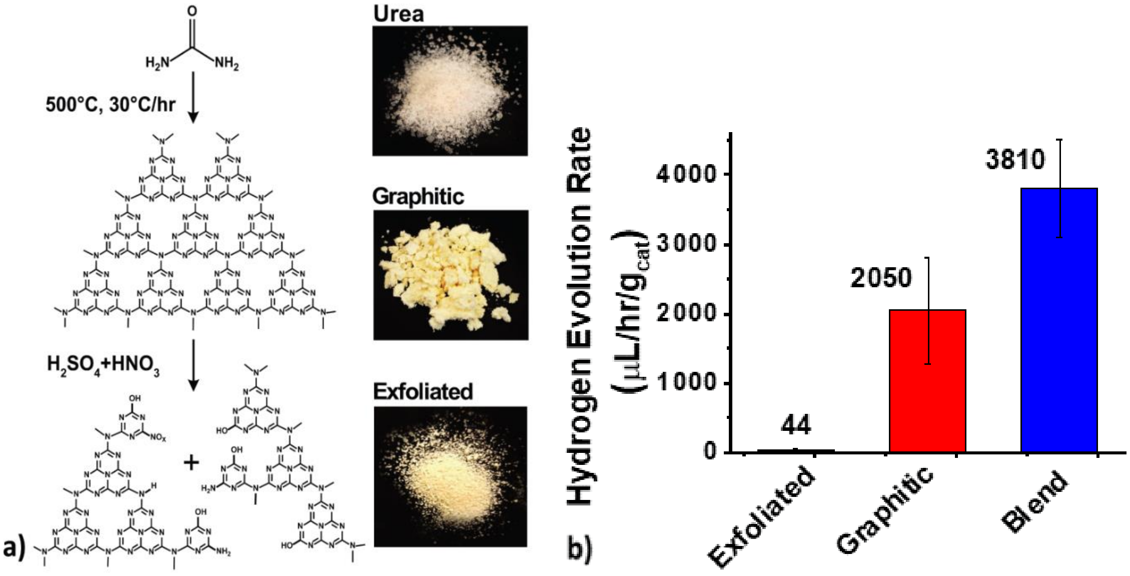

Figure 3-1. Synthesis and hydrogen evolution rate of graphitic and exfoliated carbon nitride. a) Synthesis of graphitic carbon nitride ("graphitic") from urea and subsequent chemical exfoliation of bulk graphitic carbon nitride ("exfoliated"). b) Hydrogen activity for exfoliated carbon nitride, graphitic carbon nitride and a graphitic carbon nitride suspension infused with 10% mass-loading of exfoliated carbon nitride co-catalyst under 365 nm LED illumination (5 mW/cm^2). Rates are for 2% Pt loading. Comparable activity ratios are observed without Pt loading, see Table 3-1.

Following exfoliation, we observe a significant decrease in the relative intensity and a shift to higher binding energy from 398.3 eV to 398.8 eV for the pyridinic peak, while a new peak appears at 406.2 eV, corresponding to highly oxidized chain terminations in the polymer matrix.[70] The weak signal at 404.3 eV, present in both carbon nitride spectra, has been attributed to charging effects.[69] By XPS, we also find that the overall oxygen content increased from 7% to 17% with exfoliation (Figure A-4 and Table A-1). Carbon 1s XPS data (Figure A-5) suggests that carbon-carbon bond cleavage also occurs upon exfoliation.[26, 71-72] Consistent with previous reports, the FTIR spectrum of bulk g-C_3N_4 exhibits the triazine ring breathing mode at 807 cm^{-1}, various C-N and C=N stretches from 1200 cm^{-1} to 1600 cm^{-1}, as well as the broad vibrational mode from 2700-3500 cm^{-1} which is associated with a combination of primary and secondary amines and possible

-OH stretching modes.[17,18] Exfoliation increases this broad signal indicating more primary and secondary amines or -OH moieties are present. Despite introducing oxidative chain terminations, exfoliation maintains the long-range ordering of the stacked carbon nitride polymeric structure, with *d* spacing of 0.32 nm, as demonstrated by the prominent (002) peak at 27.6 degrees in X-ray diffraction (XRD, Figure 3-2b).[50]

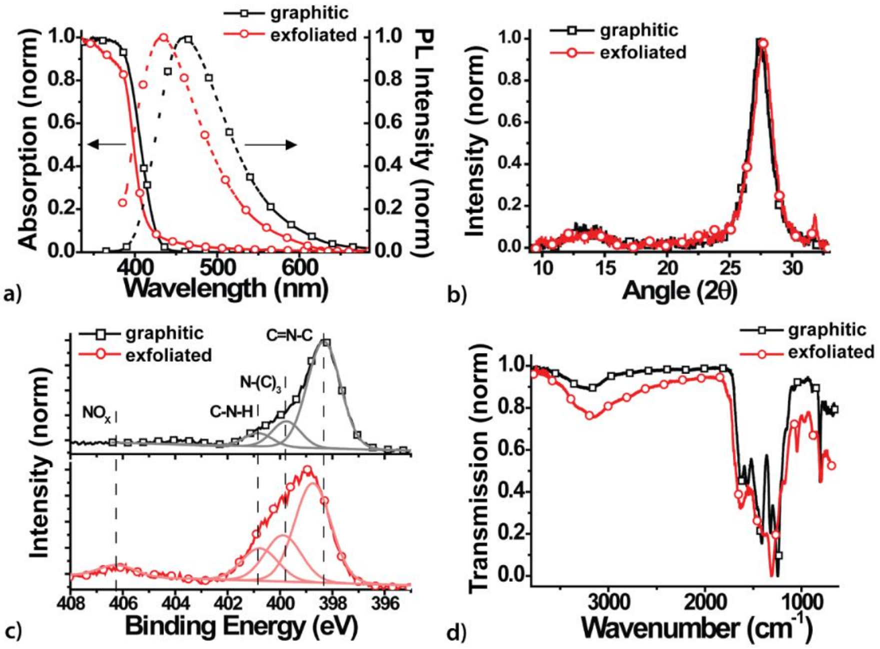

Figure 3-2. Ground state absorption, XRD, XPS and FTIR characterization of $g-C_3N_4$.
a) Ground state absorption (solid lines) and steady-state luminescence spectra (dotted lines) for 365 nm excitation of graphitic and exfoliated carbon nitride. b) X-ray diffraction (XRD) patterns for graphitic and exfoliated carbon nitride. c) Nitrogen 1s X-ray photoelectron spectroscopy (XPS) for graphitic and exfoliated carbon nitride with Gaussian fits of individual XPS peaks. The envelop peak fit is denoted with open symbols. d) Fourier Transform Infrared (FTIR) spectra of graphitic and exfoliated carbon nitride powders.

Chemically activated chain terminations, such as those in the XPS profiles for our exfoliated samples (e.g. highly oxidized moieties, amine groups, etc.), are commonly suspected to promote catalytic activity in carbon nitride.[11, 25-26, 41-43, 59, 71-74] However, we observe a hydrogen evolution rate that is almost 50 times slower for exfoliated carbon nitride (43.6 μL $h^{-1}g^{-1}$) compared to bulk g-C_3N_4 (2050 µL $h^{-1}g^{-1}$). Based only on this result, one might initially conclude that the exfoliation process poisons the catalytic sites or decreases the number density of active sites in our material. However, when we infuse our bulk g-C_3N_4 suspension with a small loading (10% by mass) of exfoliated carbon nitride, we observe a cooperative effect in which the hydrogen evolution rate jumps to 3810 µL $h^{-1}g^{-1}$ (Figure 3-1b), nearly twice that of bulk g-C_3N_4 alone. Our hydrogen evolution data suggests that rather than depleting the number of catalytic sites, exfoliation instead suppresses the exciton dissociation that has been suggested to drive long-lived interlayer charge separation in bulk g-C_3N_4.[52] We hypothesize that in the presence of exfoliated carbon nitride, an electron transfer cascade is established in which the exfoliated carbon nitride accepts photogenerated electrons that form on bulk g-C_3N_4. To test this hypothesis, we utilize TA spectroscopy spanning the femtosecond (fs) to nanosecond (ns) time window and a wavelength range spanning the visible to near-infrared (NIR) regions. In combination with picosecond (ps) time-resolved PL, these measurements allow us to monitor the electron transfer process from bulk g-C_3N_4 to exfoliated carbon nitride.

In Figure 3-3a we present the ultrafast TA spectra of bulk g-C_3N_4 at select time points from 1 ps to 5 ns. These spectra exhibit broad positive induced absorption features between 600 nm and 1350 nm, which we attribute to overlapping electron and hole absorption on the heptazine network based on fluence-dependent TA kinetics (Figure 3-4a and Figure 3-4b), reductive spectroelectrochemistry (Figure 3-4d), and electron scavenger experiments (Figure 3-5, *vide infra*). We also observe a negative signal from 420 nm to 550 nm that we associate with stimulated emission (Figure A-6). The TA spectrum of exfoliated carbon nitride exhibits limited signal magnitude compared to that of bulk g-C_3N_4 at matched excitation densities (Figure A-7). The low signal intensity for the exfoliated carbon nitride alone is consistent with our earlier hypothesis that fewer charges are generated in the exfoliated carbon nitride than in bulk g-C_3N_4.

Global analysis (Figure 3-3b) of this bulk g-C_3N_4 TA data yields two evolution associated difference spectra (EADS),[75] corresponding to one short lived spectral component (130 ps), which spans the visible and NIR spectrum, as well as a longer lived component (4.89 ns) with a similar spectral profile. We associate the faster decay with solvent relaxation and the slower decay with the recombination of non-geminate electron-hole pairs.

We first compare the pump fluence-dependence of the induced absorption (Figure 3-4a and Figure 3-4b) with that of the PL decay kinetics (Figure 3-4c) to investigate the origin of the induced absorption feature. Over a comparable range of laser fluences, we find that the decay dynamics of the induced TA signal and the PL behave differently from one another. This suggests that the emitting species and the absorbing species in TA are distinct. The NIR excited state absorption decay rate exhibits a marked fluence dependence, consistent with non-geminate charge recombination. This is true for the induced absorption monitored from 1000 – 1050 nm shown in Figure 3-4a, as well as from 1275 – 1325 nm shown in Figure 3-4b. Conversely, the PL decay rate, monitored from 475 – 525 nm in Figure 3-4c, is largely fluence-independent, suggesting quasi-monomolecular decay dynamics that we associate with neutral singlet excitons.

To further validate the identity of the photophysical species that contribute to the excited state absorption spectrum, we utilize spectroelectrochemistry to recover the absorption spectrum of negatively charged bulk g-C_3N_4. Spectroelectrochemistry is a powerful tool for identifying the absorption spectra associated with the reduced or oxidized forms of an analyte.

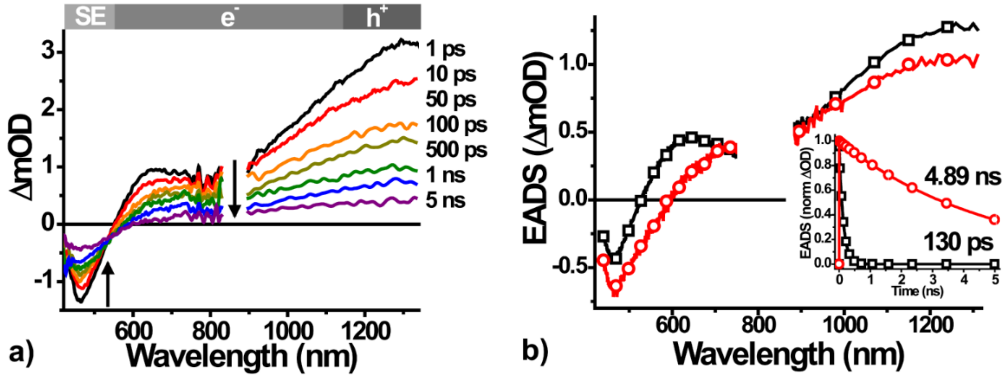

Figure 3-3. Transient absorption spectra and global analysis fits of g-C_3N_4.
a) Visible to near-infrared femtosecond transient absorption spectra of graphitic carbon nitride at selected time points from 1 ps to 5 ns and b) the evolution associated difference spectra and kinetics from global analysis. Samples excited with 365 nm pump light (1.6×10^{15} photons/cm^3/pulse).

Figure 3-4d shows the spectroelectrochemical change in absorption of a bulk g-C_3N_4 suspension under reducing conditions. A constant cathodic potential of -0.50 V referenced to a normal hydrogen electrode (NHE) (see inset in Figure 3-4d) was applied to the sample and the spectra were collected over time. The positive feature in the resulting differential spectra is associated with induced absorption of reduced carbon nitride. This induced absorption suggests that a portion of the positive feature in the TA spectrum (Figure 3-3) starting near 600 nm and extending into the NIR corresponds to photogenerated electrons on carbon nitride. The negative feature in the spectroelectrochemical spectra from 375 to 550 nm is the bleach of the neutral ground state absorption of bulk g-C_3N_4 (Figure A-6).

Furthermore, we introduce chemical charge quenchers to scavenge electrons and holes from bulk g-C_3N_4 while we monitor the response of the induced absorption and PL to further corroborate our TA spectral assignments. Interestingly, the PL lifetime of bulk g-C_3N_4 remains unquenched (Figure 3-5a) when we introduce an electron scavenger (e.g. persulfate, sulfate, or nitrate ions), a hole scavenger (e.g. methanol or triethanolamine) or the exfoliated carbon nitride.

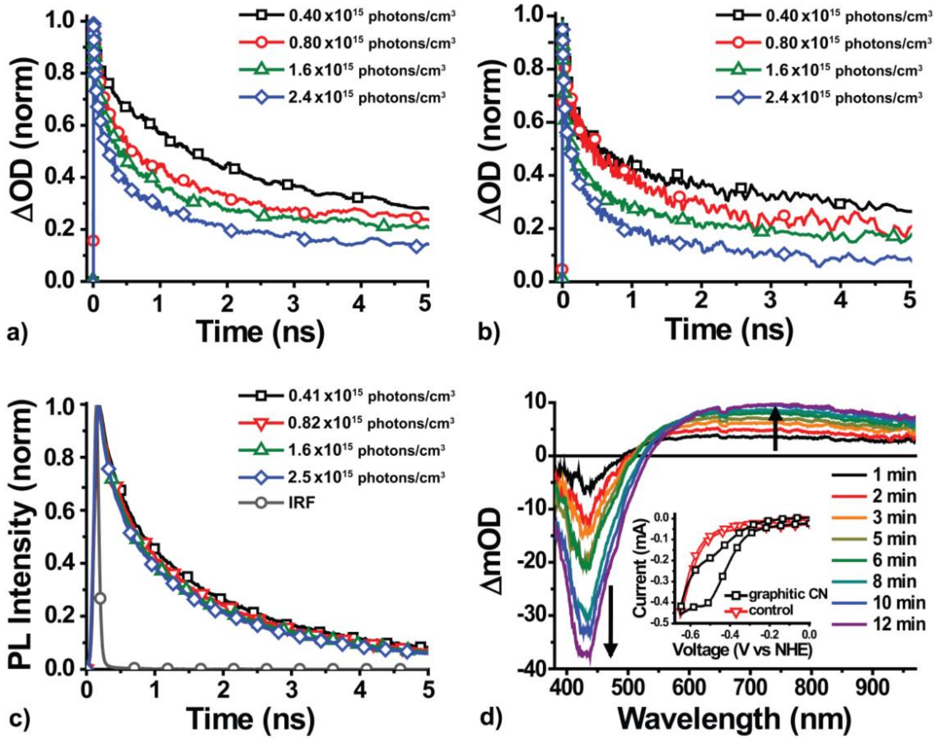

Figure 3-4. Fluence-dependent transient absorption spectra and kinetics of g-C_3N_4. Experimentally measured pump fluence-dependent transient absorption (TA) kinetics of graphitic carbon nitride (g-C_3N_4) probed at a) 1000 – 1050 nm and b) 1275 – 1325 nm. c) Fluence-independent photoluminescence (PL) decay for g-C_3N_4 (475 – 525 nm). TA and PL kinetics measured under 365 nm pump with $0.4\times10^{15} – 2.5\times10^{15}$ absorbed photons/cm^3/pulse, as indicated. d) Differential absorption for cathodic spectroelectrochemistry of g-C_3N_4 in 0.5 M sodium hydroxide. Fluorine-doped tin oxide (FTO), Ag/AgCl, and a platinum wire served as the working, pseudo-reference and counter electrodes, respectively. Inset shows cathodic cyclic voltammagram of g-C_3N_4 in 5% nafion matrix on FTO scanned at 200 mV/s.

Conversely, when we add an electron scavenger (as shown for sulfate in Figure 3-5b and persulfate or nitrate ions in Figure A-8) the photoinduced absorption signal from approximately 600 – 1250 nm is quenched, while the low energy induced absorption from 1100 – 1350 nm is largely unperturbed. This is most evident by examining the dynamic quenching in the kinetic traces from 1000 – 1050 nm in Figure 3-5c and the lack of quenching from 1275 – 1325 nm, shown in Figure A-9. The static and dynamic electron quenching effect, along with the spectroelectrochemical electron absorption and fluence-dependent TA, indicates that the absorptive features in the 600 – 1250 nm region of the TA spectrum are primarily associated with photogenerated electrons in our bulk g-C_3N_4 samples. Recalling that, in the absence of an extrinsic quencher, the lower energy portion of the NIR spectrum (1100 – 1350 nm) exhibits nearly identical fluence-dependent (non-geminate) decay kinetics to the electron absorption, we associate signals in this low energy feature with absorption of positive charge carriers (holes). With the addition of a hole scavenger, such as triethanolamine (Figure 3-5b and Figure 3-5c) or methanol, the spectrum and dynamics are not quenched within the time window of our measurement. This suggests that the quenching rates for photogenerated holes are comparatively slow. While the dynamic quenching for the electron (Figure 3-5c) is relatively fast, one can estimate a diffusion rate constant in water to be between $3.0\times10^{9}\ M^{-1}s^{-1}$ and $7.4\times10^{9}\ M^{-1}s^{-1}$. With 0.5 M sodium sulfate as the electron scavenger, the expected diffusion limit is on the order of several hundred picoseconds (270 ps – 660 ps),[76-77] which is commensurate with the kinetics that we measure experimentally.

Figure 3-5b shows that the TA signal magnitude in the 600 – 1250 nm region diminishes dramatically when we introduce chemically exfoliated carbon nitride into the suspension. In fact, the TA spectrum and kinetics (Figure 3-5c) for bulk g-C_3N_4 after the addition of 10% mass loading of exfoliated carbon nitride are almost identical to the quenching that we observe with known electron scavengers. This quenching suggests that bulk g-C_3N_4 transfers photogenerated electrons to exfoliated carbon nitride.

To more thoroughly examine the kinetics of positive and negative charge carriers based on our TA spectra, we apply global target analysis to evaluate our data according to a model with suitable physicochemical parameters.[75] Global target analysis is a method to analyze the superposition of species-associated difference spectra (SADS)[78] that appear in transient spectroscopy, weighted by their concentration over time. The overall transient spectrum, $\psi(t,\lambda)$, at time t is represented as a sum of concentration-weighted spectra over the total number of components such that, $\psi(t,\lambda) = \Sigma c_i(t)\sigma_i(\lambda)$, where $c_i(t)$ and $\sigma_i(\lambda)$ correspond respectively to the time-dependent, wavelength-independent concentration and the wavelength-dependent, time-independent SADS of the i^{th} species. As we show in Figure 3-6, this analysis allows us to more clearly assess the electron and hole dynamics. For clarity, we focus on the NIR region, where the spectral overlap between positive and negative features is minimal. From our target analysis, we recover two distinct SADS, σ_e corresponding to electrons (Figure 3-6a) and σ_h corresponding to holes (Figure 3-6c) on bulk g-C_3N_4. These SADS are consistent with our spectroelectrochemical measurements, our electron quenching experiments, and our fluence-dependent TA kinetics.

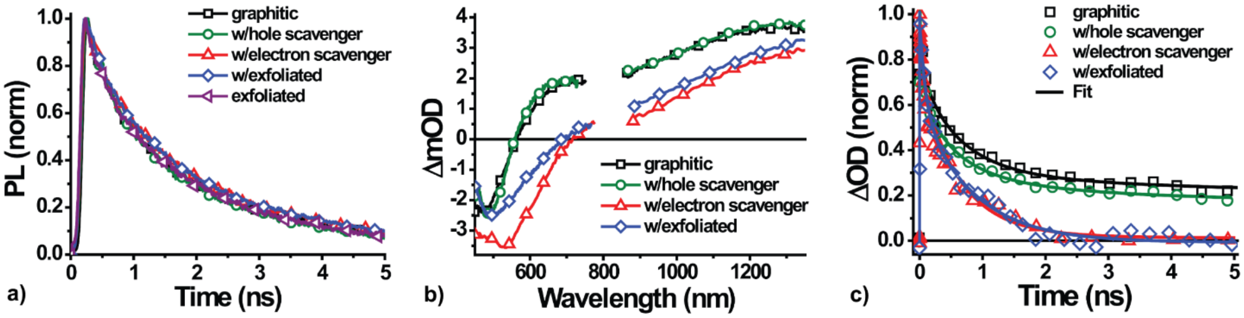

Figure 3-5. Comparing photoluminescence kinetics and transient absorption spectra and kinetics of graphitic carbon nitride with hole and electron scavengers.
a) Quencher-independent photoluminescence (PL) decay kinetics for graphitic carbon nitride (g-C_3N_4). b) Transient absorption (TA) spectra and c) experimentally measured quencher-dependent TA kinetics probed at 1000 – 1050 nm for g-C_3N_4 in the absence of and in the presence an extrinsic chemical electron scavenger compared to g-C_3N_4 infused with 10% mass loading of exfoliated carbon nitride. g-C_3N_4 in the presence of a hole scavenger is included for reference. Measured kinetics (symbols) in c) are overlaid with fits to the data (lines) obtained from global target analysis described in Chapter 3. Samples were excited with 365 nm pump (1.6×10^{15} photons/cm^3/pulse).

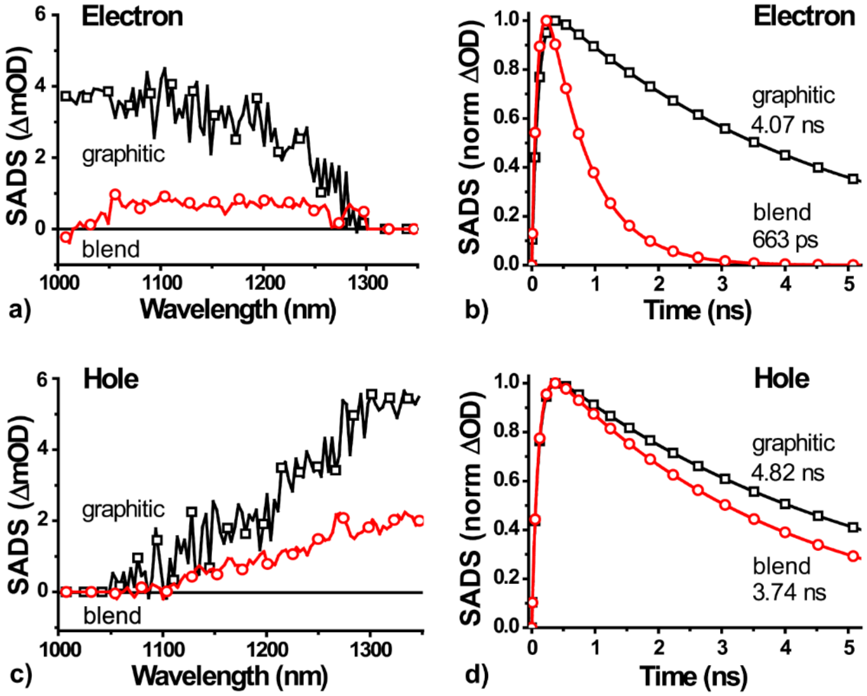

Figure 3-6. Target analysis of graphitic carbon nitride transient absorption.
Target analysis of the transient absorption data shown in Figure 3-5 for graphitic carbon nitride (“graphitic”) and a mixture of graphitic carbon nitride plus 10% exfoliated carbon nitride by mass (“blend"). Species associated difference spectra (SADS) σ_e for the electron a) and σ_h for the hole c) correspond to the kinetics profiles in b) and d), respectively.

The resulting kinetic parameters extracted for the electron and hole in our target analysis yield excellent fits to the experimental data shown in Figure 3-5c and indicate a drastic quenching of the electron lifetime in Figure 3-6b when 10% mass loading of exfoliated carbon nitride is added to graphtic carbon nitride. The decay of the quenched electron in the blend occurs on a timescale of several hundred picoseconds (663 ps), as expected for diffusion controlled kinetics in water (*vide supra*). By comparison, the lifetime of the hole on bulk g-C_3N_4 is largely unperturbed by the addition of exfoliated carbon nitride (Figure 3-6d).

Based on our spectroscopic characterization and our photocatalytic results, we propose the kinetic scheme depicted in Figure 3-7a for g-C_3N_4 in the presence and in the absence of exfoliated carbon nitride. Given that the TA signals for electrons (e^-) and holes (h^+) on bulk g-C_3N_4 emerge within the temporal response of our instrument, we conclude that exciton dissociation occurs in layered bulk g-C_3N_4 on timescales of $1/k_{cs}$ = 200 fs or faster.[52] From the electron signal magnitude we estimate the concentration of photogenerated charges that result from each excitation pulse and we place a lower bound estimate on the photoinduced charge separation efficiency, η_{cs}, in bulk g-C_3N_4 of η_{cs} = 65%. That is, at least 65% of the excitons that are generated during photon absorption by bulk g-C_3N_4 are converted to non-geminate electron – hole pairs that contribute to the TA signal that we measure. To estimate the charge separation efficiency, we assume that each g-C_3N_4 chromophore comprises a single heptazine monomer. We take the molar absorption coefficient (ε) of the polaron to be no greater in magnitude than that of the neutral ground state chromophore (~5,000 L mol^{-1} cm^{-1}) which has been demonstrated to be a reasonable assumption experimentally[79] and predicted computationally[80] for semiconducting polymers. We then relate the change in electron concentration (Δc) to our TA signal magnitude (ΔOD) using Beer's law as $\Delta c = \Delta \mathrm{OD}/\varepsilon l$, where l is the path length. The estimates for the electron generation efficiency that we obtain should thus be regarded as a very conservative lower limit.

In the absence of any additional charge scavenger, we observe moderate rates for non-geminate electron ($1/k_e$ = 4.1 ns) and hole ($1/k_h$ = 4.8 ns) decay. The electron absorption feature for g-C_3N_4 is rapidly quenched by charge transfer with a quenching time of $1/k_e'$ = 0.66 ns in the presence of exfoliated carbon nitride. However, the neutral singlet exciton fluorescence lifetime ($1/k_f$ = 3.0 ns) and fluorescence quantum efficiency (η_f = 5.2% Table 3-1) are insensitive to the addition of exfoliated carbon nitride. We infer the presence of a non-geminate (fluence-dependent) charge-separated intermediate state (CS in Figure 3-7b), which is non-luminescent, but can participate in productive photocatalysis.

Table 3-1. Photochemical and photophysical parameters for carbon nitride photocatalysts.

	Symbol	Units	Graphitic	Exfoliated	Blend [f]
Electronic Transition Energy [a]	E_{00}	nm, eV	415, 2.99	398, 3.12	-
Singlet Exciton Emission Peak Max		nm, eV	460, 2.70	435, 2.85	458, 2.71
Singlet Exciton Emission Lifetime [b,c]	$1/k_f$	ns	2.98	2.82	2.93
Fluorescence Quantum Efficiency	η_{f}	%	5.2 ± 0.05	3.1 ± 0.22	5.2 ± 0.03
Hydrogen Evolution Rate [d]		μL h^{-1}g^{-1}	2050 ± 702	43.6 ± 5.5	3810 ± 764
Electron Lifetime [b,e]	$1/k_e$	ns	4.07	-	0.663
Hole Lifetime [b,e]	$1/k_h$	ns	4.82	-	3.74
Photogenerated Charge Efficiency [f]	η_{cs}	%	>65	-	-

[a] Transition energy estimated from spectral intersection of absorption and emission. [b] Extracted based on global target analysis. [c] Short time components are approximately 400 ps for graphitic, exfoliated and the blend. [d] Activities reported for 2% mass loading of platinum. Activities without platinum are graphitic: 5.4 μL h^{-1}g^{-1} and blend: 10.6 μL h^{-1}g^{-1}. Activity for exfoliated carbon nitride alone was below detectable limits. [e] Lower bound estimate. Assumes polaron absorption coefficients (ε) is no greater than that of neutral ground state. There is no correction for scattered excitation light. [f] Colloidal suspension: 90% graphitic / 10% exfoliated carbon nitride by mass.

Figure 3-7b depicts the relative energy ordering of the non-geminate charge separated (CS) intermediate state that our kinetic analysis suggests. The CS state is populated following optical excitation of the carbon nitride singlet state (S_1), which possesses an excited state ionization energy[81-84] ($E_{(M+/M*)}$) equal to the sum of the ground state ionization energy ($E_{(M+/M)}$) and the optical transition energy[76] (E_{00}), such that $E_{(M+/M*)} = E_{(M+/M)} + E_{00}$. The ionization energy ($E_{(M+/M)}$) was estimated using experimental and theoretical UPS values from the literature.[24, 85-91] From electron quenching of the CS state and the subsequent enhancement in proton reduction, we conclude that both electron transfer steps must be exergonic.

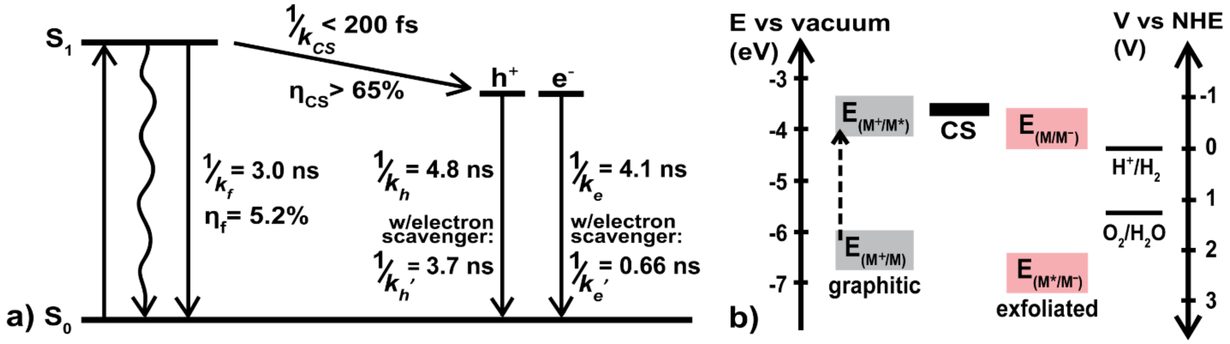

Figure 3-7. Proposed kinetic scheme and energy level diagram.
(a) Proposed kinetic scheme based on fitting parameters derived from global target analysis of ultrafast transient absorption data and time resolved luminescence for exciton, hole and electron decays in carbon nitride. Kinetic parameters are described in Chapter 3 and summarized in Table 3-1. (b) Proposed energy diagram depicting exergonic electron transfer cascade pathway involving the excited-state oxidation potential with an energy, $E_{(M+/M*)}$, and charge-separated (CS) intermediate states of graphitic carbon nitride ("graphitic") relative to the ground state reduction potential of exfoliated carbon nitride ("exfoliated") with energy, $E_{(M/M-)}$, that is consistent with our time-resolved spectroscopy measurements and photocatalytic hydrogen evolution experiments. Left scale is energy (E) versus vacuum level ($E = 0$) and the right scale is potential (V) versus normal hydrogen electrode (NHE). Estimates for energies ($E_{(M+/M)}$) associated with the ground state oxidation potentials are also depicted.

Electrons in the non-geminate CS state of g-C_3N_4 are quenched by exfoliated carbon nitride on relatively fast timescales that one would more commonly associate with diffusion-controlled molecular interactions. This surprising finding suggests that the active chemical species responsible for the cooperative near-doubling of the hydrogen evolution rate in the blend is likely a low molecular weight oligomer or molecular unit rather than an extended higher-dimensional nanostructure. These results appear to be consistent with recent reports by Lotsch et al.,[11-12, 59, 92] suggesting that oligomers and molecular heptazine-based materials may be promising future targets for next-generation organic photocatalysts.

3.3 CONCLUSIONS

Using visible and NIR ultrafast TA, we present the first direct spectroscopic characterization of the photoinduced electron transfer cascade (shown in Figure 3-7) that is established between g-

C_3N_4 and chemically exfoliated carbon nitride. We observe a correlation between the electron transfer mechanism and the near-doubling of the photocatalytic rate of aqueous hydrogen evolution when exfoliated carbon nitride is added to g-C_3N_4. From XPS and FTIR we conclude that exfoliated carbon nitride contains a higher density of oxidative chain terminations when compared to g-C_3N_4, indicating that exfoliated carbon nitride likely has more catalytically active sites for hydrogen evolution. Our quenching experiments and spectroelectrochemistry results suggest that the TA signal from approximately 600 – 1250 nm is associated with the electron absorption. The timescale for the electron transfer process that we observe approaches rates that are consistent with diffusion-controlled small molecule interactions. This surprising result suggests that it might be fruitful to target new oligomeric or molecular species to further improve the activity of organic photocatalysts. The excited state electron dynamics that we have uncovered here help to provide a roadmap for chemical and structural modifications aimed at controlling charge generation and recombination kinetics to improve the activity of future high-performance organic photocatalysts.

3.4 EXPERIMENTAL METHODS

Reagents: Urea, sodium sulfate, sodium persulfate, silver nitrate, triethanolamine, nafion (5% in aliphatic alcohols) and FTO (surface resistivity ~7 Ω/sq) were purchased from Sigma Aldrich. Sulfuric and nitric acids were purchased from Macron Fine Chemicals.

Preparation of g-C_3N_4: Urea (10 g) was heated in a porcelain crucible (20 mL) using a potter's kiln at 500˚C for 3 hours, with a ramp rate of 30˚C per hour under ambient atmosphere. The light-yellow product was ground thoroughly with a mortar and pestle prior to characterization.

Preparation of exfoliated carbon nitride: g-C_3N_4 (80 mg) was carefully added to a mixture nitric acid (30 mL, conc.) and sulfuric acid (10 mL, conc.). The solution was sonicated (1 hour) and stirred (23 hours) in a fume hood. The homogeneous solution was added to DI water (200 mL) and the product was filtered through a microporous membrane (0.45 μm PVDF filter purchased from Sterlitech Corporation). Resultant powder was ground thoroughly with a mortar and pestle.

Sample preparation: Suspensions (2.0 mg/mL) were prepared by sonicating the carbon nitride catalyst in deionized (DI) water for 24 hours, then was left to settle for 48 hours. The supernatant liquid was collected and used for all non-powder characterization, including TA spectroscopy, spectroelectrochemistry, and photocatalysis.

Physical and chemical characterization: Transmission electron microscopy (TEM) was performed with a 200 kV Tecnai G2 F20 Supertwin with samples mounted on 300 mesh ultrathin carbon coated copper grids. X-ray diffraction (XRD) patterns were collected on a Bruker D8 Discover system with powder samples mounted on glass substrates, using Cu-Kα radiation (λ = 1.5418 Å). X-ray photoelectron spectroscopy (XPS) was performed on a Surface Sciences Instruments M-Probe with powder samples mounted on glass slides. Fourier transform infrared (FTIR) spectroscopy was carried out on a Nicolet 8700 spectrometer in attenuated total reflection (ATR) mode with active N_2 purging.

Steady-state optical characterization: Ground state absorption spectra were collected in diffuse reflectance geometry with a Cary-5000 UV-vis-NIR spectrometer using an integrating sphere with barium sulfate as the reference. The Kubelka-Munk function was computed directly using commercial software provided by the vendor. Steady-state photoluminescence (PL) was acquired on a home-built spectrometer using amplitude-modulated excitation and phase sensitive detection. Samples were irradiated with a modulated (200 Hz) 365 nm LED (5.2 mW/cm^2).

Photocatalytic activity: Hydrogen evolution was measured with a SRI GC (8610 C) equipped with a thermal conductivity detector and a 6' MS-13X column, using argon as the carrier gas. Samples were made with carbon nitride suspensions in DI water with 10% (v/v) triethanolamine as a sacrificial hole acceptor and chloroplatinic acid (2% photo-deposited Pt loading). Samples were illuminated with 4, 365 nm LEDs (5 mW/cm^2) for 24 hours while stirring at 1150 rpm. The hydrogen generation rate is normalized to the length of time the sample was illuminated as well as the total mass of the catalyst in the system. We note that the catalytic activity for the blend compared to g-C_3N_4 alone also nearly doubles when we do not incorporate Pt as a co-catalyst. Under identical illumination conditions, the H_2 activity for the Pt-free blend was 10.58 µL h^{-1}g^{-1}, while that of g-C_3N_4 alone was 5.44 µL h^{-1}g^{-1}.

Electrochemical characterization: Cyclic voltammetry (CV) was performed in sodium hydroxide (0.5 M) with a fluorine-doped tin oxide (FTO) working electrode, Ag/AgCl reference and platinum counter electrodes. The FTO working electrode was coated with a g-C_3N_4/nafion matrix to mitigate slow mass transport to the electrode surface. The matrix was prepared by adding a 5% nafion solution to a 2.0 mg/mL suspension of carbon nitride material that was extracted from decanted supernatant liquid following 24 hours of sonication. Spectroelectrochemistry was performed with a suspension of carbon nitride in sodium hydroxide (0.5 M) and an ozone treated FTO substrate as the working electrode (submerged in a 1 cm quartz cuvette). A platinum wire and Ag/AgCl were used as a counter and reference electrode respectively. The electrochemical cell was held at -0.5 V vs NHE and the change in the absorption spectrum was collected over time.

Transient absorption spectroscopy: Samples were irradiated with the 365 nm output of a Coherent, Inc./Light Conversion OPerA Solo optical parametric amplifier (OPA) that was pumped with 50 fs pulses from a 1 kHz Ti:Sapphire amplifier (Libra-HE, Coherent, Inc.) to generate

$0.41\times10^{15} – 2.5\times10^{15}$ excitations/cm^3/pulse within the sample. Supercontinuum probe pulses (~200 fs) were generated by focusing a fraction of the 800 nm amplifier output onto CaF_2 or sapphire plates. Spectra were collected with a CMOS sensor and InGaAs fiber-coupled multichannel photodiode array spectrometer and plotted as the differential optical density $\Delta OD = \log_{10} [I_{0\ sample}/I_{ex\ sample} \times I_{ex\ ref}/I_{0\ ref}]$. Samples were irradiated with spatially aligned pump and probe beams, with the probe beam temporally delayed from the pump using a mechanical delay line (Ultrafast Systems). Kinetics were recorded with random time steps to minimize any influence of sample degradation over the time of the experiment. The estimated absorbed photon flux was not corrected for laser scatter.

Time-resolved PL: Time-resolved PL spectra were collected using a Hamamatsu streak camera (C10910) with a slow-sweep unit (M10913-01). Samples were irradiated with 50 fs pulses at 365 nm and 1 kHz pump from a Coherent/Light Conversion OPerA solo optical parametric amplifier (OPA) to generate $0.41\times10^{15} – 2.5\times10^{15}$ excitations/cm^3/pulse within the sample.

Global and target analysis: To model time-resolved spectral decay parameters, global and target analyses were performed using Glotaran,[75] a graphical user interface for the R-package TIMP, which is itself a problem solving environment for fitting superposition models. The number of components for global analysis of g-C_3N_4 TA and PL data was selected based on singular value decomposition, and no parameter constraints were placed on the parallel evolution model. Identical decay parameters were obtained from a sequential decay model. Physicochemical data used in target analysis were obtained from spectroelectrochemistry and TA absorption quenching experiments. Accordingly, the target model assumes that σ_e(1350 nm) = 0 and σ_h(1000 nm) = 0. During target analysis, early time decay constants (~100 ps) were imposed using results obtained from unconstrained global analysis. No constraints were placed on longer time components.

3.5 REFERENCES

1. Kalisman, P., et al., Perfect Photon-to-Hydrogen Conversion Efficiency. *Nano Lett* **2016,** *16* (3), 1776-81.
2. Uygun, M., et al., Photopolymerization Kinetics and Dynamic Mechanical Properties of Silanes Hydrolyzed without Evolution of Byproducts. Tetrakis[(methacryloyloxy)ethoxy]silane−Diethylene Glycol Dimethacrylate. *Macromolecules* **2011,** *44* (7), 1792-1800.
3. Seger, B., et al., Using TiO2 as a Conductive Protective Layer for Photocathodic H2 Evolution. *J. Am. Chem. Soc.* **2013,** *135* (3), 1057-1064.
4. Roske, C. W., et al., Comparison of the Performance of CoP-Coated and Pt-Coated Radial Junction n+p-Silicon Microwire-Array Photocathodes for the Sunlight-Driven Reduction of Water to H2(g). *Journal of Physical Chemistry Letters* **2015,** *6* (9), 1679-1683.
5. Warren, E. L., et al., Hydrogen-evolution characteristics of Ni-Mo-coated, radial junction, n(+)p-silicon microwire array photocathodes. *Energy & Environmental Science* **2012,** *5* (11), 9653-9661.
6. Kudo, A.; Miseki, Y., Heterogeneous photocatalyst materials for water splitting. *Chem Soc Rev* **2009,** *38* (1), 253-78.
7. Kato, H., et al., Highly efficient water splitting into H2 and O2 over lanthanum-doped NaTaO3 photocatalysts with high crystallinity and surface nanostructure. *J Am Chem Soc* **2003,** *125* (10), 3082-9.
8. Kamat, P. V.; Christians, J. A., Solar Cells versus Solar Fuels: Two Different Outcomes. *J Phys Chem Lett* **2015,** *6* (10), 1917-8.

9. Yang, X., et al., Mechanistic Studies of Electrode-Assisted Catalytic Oxidation by Flavinium and Acridinium Cations. *ACS Catal.* **2014,** *4* (8), 2635-2644.

10. Mirzakulova, E., et al., Electrode-assisted catalytic water oxidation by a flavin derivative. *Nature chemistry* **2012,** *4* (10), 794-801.

11. Lau, V. W., et al., Low-molecular-weight carbon nitrides for solar hydrogen evolution. *J Am Chem Soc* **2015,** *137* (3), 1064-72.

12. Schwinghammer, K., et al., Phenyl-triazine oligomers for light-driven hydrogen evolution. *Energy & Environmental Science* **2015,** *8* (11), 3345-3353.

13. Li, L., et al., Photocatalysts Based on Cobalt-Chelating Conjugated Polymers for Hydrogen Evolution from Water. *Chem. Mater.* **2016,** *28* (15), 5394-5399.

14. Li, L., et al., Rational Design of Porous Conjugated Polymers and Roles of Residual Palladium for Photocatalytic Hydrogen Production. *J. Am. Chem. Soc.* **2016,** *138* (24), 7681-7686.

15. Yanagida, S., et al., Poly(p-phenylene)-catalysed photoreduction of water to hydrogen. *Journal of the Chemical Society, Chemical Communications* **1985,** (8), 474-475.

16. Shibata, T., et al., Novel visible-light-driven photocatalyst. Poly(p-phenylene)-catalyzed photoreductions of water, carbonyl compounds, and olefins. *The Journal of Physical Chemistry* **1990,** *94* (5), 2068-2076.

17. Sprick, R. S., et al., Visible-Light-Driven Hydrogen Evolution Using Planarized Conjugated Polymer Photocatalysts. *Angew Chem Int Ed Engl* **2016,** *55* (5), 1792-6.

18. Xinchen, W., et al., A metal-free polymeric photocatalyst for hydrogen production from water under visible light. *Nat. Mater.* **2009,** *8,* 76-80.

19. Maeda, K., et al., Photocatalytic Activities of Graphitic Carbon Nitride Powder for Water Reduction and Oxidation under Visible Light. *J. Phys. Chem. C* **2009,** *113* (Copyright (C) 2016 American Chemical Society (ACS). All Rights Reserved.), 4940-4947.

20. Jun, Y.-S., et al., Mesoporous, 2D Hexagonal Carbon Nitride and Titanium Nitride/Carbon Composites. *Advanced Materials* **2009,** *21* (Copyright (C) 2016 American Chemical Society (ACS). All Rights Reserved.), 4270-4274.

21. Xiang, Q.; Yu, J., Graphene-Based Photocatalysts for Hydrogen Generation. *J Phys Chem Lett* **2013,** *4* (5), 753-9.

22. Zhao, C., et al., A novel composite of TiO2 nanotubes with remarkably high efficiency for hydrogen production in solar-driven water splitting. *Energy & Environmental Science* **2014,** *7* (5), 1700-1707.

23. Liebig, J., Uber einige Stickstoff - Verbindungen. *Annalen der Pharmacie* **1834,** *10* (1), 1-47.

24. Liu, J., et al., Metal-free efficient photocatalyst for stable visible water splitting via a two-electron pathway. *Science* **2015,** *347* (6225), 970-4.

25. Wang, W., et al., g-C3N4 quantum dots: direct synthesis, upconversion properties and photocatalytic application. *Chemical Communications* **2014,** *50,* 10148-10150.

26. Zhang, H., et al., Pyridine derivative/graphene nanoribbon composites as molecularly tunable heterogeneous electrocatalysts for the oxygen reduction reaction. *Phys Chem Chem Phys* **2016,** *18* (6), 5040-7.

27. Liu, A. Y.; Cohen, M. L., Prediction of new low compressibility solids. *Science* **1989,** *245* (4920), 841-2.

28. Teter, D. M.; Hemley, R. J., Low-compressibility carbon nitrides. *Science* **1996,** *271* (5245), 53-55.

29. Goettmann, F., et al., Chemical synthesis of mesoporous carbon nitrides using hard templates and their use as a metal-free catalyst for Friedel-Crafts reaction of benzene. *Angew Chem Int Ed Engl* **2006,** *45* (27), 4467-71.

30. Liu, J., et al., Self-regenerated solar-driven photocatalytic water-splitting by urea derived graphitic carbon nitride with platinum nanoparticles. *Chem. Commun.* **2012,** *48* (70), 8826-8.

31. Xu, J., et al., Eosin Y-sensitized graphitic carbon nitride fabricated by heating urea for visible light photocatalytic hydrogen evolution: the effect of the pyrolysis temperature of urea. *Phys Chem Chem Phys* **2013,** *15* (20), 7657-65.

32. Huang, J., et al., Metal-free disinfection effects induced by graphitic carbon nitride polymers under visible light illumination. *Chem Commun (Camb)* **2014,** *50* (33), 4338-40.

33. Zheng, Y., et al., Graphitic Carbon Nitride Polymers toward Sustainable Photoredox Catalysis. *Angew Chem Int Ed Engl* **2015,** *54* (44), 12868-84.

34. Chen, Y.; Qin, Z., General applicability of nanocrystalline Ni2P as a noble-metal-free cocatalyst to boost photocatalytic hydrogen generation. *Catal. Sci. Technol.* **2016,** *6* (23), 8212-8221.

35. Li, C., et al., Unique P-Co-N Surface Bonding States Constructed on g-C3N4 Nanosheets for Drastically Enhanced Photocatalytic Activity of H2 Evolution. *Advanced Functional Materials* **2017,** *27* (4), 1604328.

36. Hou, Y., et al., Layered nanojunctions for hydrogen-evolution catalysis. *Angew Chem Int Ed Engl* **2013,** *52* (13), 3621-5.

37. Kasap, H., et al., Solar-Driven Reduction of Aqueous Protons Coupled to Selective Alcohol Oxidation with a Carbon Nitride-Molecular Ni Catalyst System. *J Am Chem Soc* **2016,** *138* (29), 9183-92.

38. Geim, A.; Novoselov, K. The Nobel Prize in Physics 2010. http://www.nobelprize.org/nobel_prizes/physics/laureates/2010/ (accessed December 2016).

39. Wang, Q. H., et al., Electronics and optoelectronics of two-dimensional transition metal dichalcogenides. *Nature nanotechnology* **2012,** *7* (11), 699-712.

40. Chong, S. Y., et al., Tuning of gallery heights in a crystalline 2D carbon nitride network. *Journal of Materials Chemistry A* **2013,** *1* (4), 1102-1107.

41. Bojdys, M. J., et al., Exfoliation of crystalline 2D carbon nitride: thin sheets, scrolls and bundles via mechanical and chemical routes. *Macromol Rapid Commun* **2013,** *34* (10), 850-4.

42. Du, X., et al., A scalable chemical route to soluble acidified graphitic carbon nitride: an ideal precursor for isolated ultrathin g-C3N4 nanosheets. *Nanoscale* **2015,** *7* (19), 8701-6.

43. Lau, V. W., et al., Rational design of carbon nitride photocatalysts by identification of cyanamide defects as catalytically relevant sites. *Nat Commun* **2016,** *7*, 12165.

44. Haque, S. A., et al., Parameters influencing charge recombination kinetics in dye-sensitized nanocrystalline titanium dioxide films. *Journal of Physical Chemistry B* **2000,** *104* (3), 538-547.

45. Tachibana, Y., et al., Subpicosecond interfacial charge separation in dye-sensitized nanocrystalline titanium dioxide films. *Journal of Physical Chemistry* **1996,** *100* (51), 20056-20062.

46. Kamat, P. V., et al., Photoinduced Charge Transfer between Carbon and Semiconductor Clusters. One-Electron Reduction of C60 in Colloidal TiO2 Semiconductor Suspensions. *The Journal of Physical Chemistry* **1994,** *98* (37), 9137-9142.

47. Peiró, A. M., et al., Photochemical Reduction of Oxygen Adsorbed to Nanocrystalline TiO2 Films: A Transient Absorption and Oxygen Scavenging Study of Different TiO2 Preparations. *Journal of Physical Chemistry B* **2006,** *110* (46), 23255-23263.

48. Fujishima, A., et al., TiO2 photocatalysis and related surface phenomena. *Surface Science Reports* **2008,** *63* (12), 515-582.

49. Koelle, U., et al., Dynamics of interfacial charge-transfer reactions in semiconductor dispersions. Reduction of cobaltoceniumdicarboxylate in colloidal titania. *Inorganic chemistry* **1985,** *24* (14), 2253-2258.

50. Merschjann, C., et al., Photophysics of polymeric carbon nitride: An optical quasimonomer. *Physical Review B* **2013,** *87* (20).

51. Zhang, H.; Yu, A., Photophysics and Photocatalysis of Carbon Nitride Synthesized at Different Temperatures. *J. Phys. Chem. C* **2014,** *118* (22), 11628-11635.

52. Merschjann, C., et al., Complementing Graphenes: 1D Interplanar Charge Transport in Polymeric Graphitic Carbon Nitrides. *Adv Mater* **2015,** *27* (48), 7993-9.

53. Zhang, H., et al., Charge carrier kinetics of carbon nitride colloid: a femtosecond transient absorption spectroscopy study. *Phys Chem Chem Phys* **2016,** *18* (22), 14904-10.

54. Ye, C., et al., Enhanced Driving Force and Charge Separation Efficiency of Protonated g-C3N4 for Photocatalytic O2 Evolution. *ACS Catal.* **2015,** *5* (11), 6973-6979.

55. Albero, J., et al., Toward Efficient Carbon Nitride Photoelectrochemical Cells: Understanding Charge Transfer Processes. *Advanced Materials Interfaces* **2017,** *4* (1), 1600265-n/a.

56. Ye, C., et al., Protonated Graphitic Carbon Nitride with Surface Attached Molecule as Hole Relay for Efficient Photocatalytic O2 Evolution. *ACS Catal.* **2016,** *6* (12), 8336-8341.

57. Walsh, J. J., et al., Photochemical CO2 reduction using structurally controlled g-C3N4. *Phys Chem Chem Phys* **2016,** *18* (36), 24825-24829.

58. Velusamy, D. B., et al., 2D Organic–Inorganic Hybrid Thin Films for Flexible UV–Visible Photodetectors. *Advanced Functional Materials* **2017**, 1605554-n/a.

59. Schwinghammer, K., et al., Triazine-based carbon nitrides for visible-light-driven hydrogen evolution. *Angew Chem Int Ed Engl* **2013,** *52* (9), 2435-9.

60. Koryakin, A., et al., Thermography of urea and its pyrolysis products. *Zhurnal Organicheskoi Khimii* **1971,** *7* (5), 972-&.

61. Liu, J. H., et al., Simple pyrolysis of urea into graphitic carbon nitride with recyclable adsorption and photocatalytic activity. *J. Mater. Chem.* **2011,** *21* (38), 14398-14401.

62. Dong, F., et al., Efficient synthesis of polymeric g-C3N4 layered materials as novel efficient visible light driven photocatalysts. *Journal of Materials Chemistry* **2011,** *21* (39), 15171-15174.

63. Kronemeijer, A. J., et al., Two-dimensional carrier distribution in top-gate polymer field-effect transistors: correlation between width of density of localized states and Urbach energy. *Adv Mater* **2014,** *26* (5), 728-33.

64. Ronning, C., et al., Carbon nitride deposited using energetic species: A review on XPS studies. *Physical Review B* **1998,** *58* (4), 2207-2215.

65. Wang, P., et al., Efficient degradation of organic pollutants and hydrogen evolution by g-C3N4 using melamine as the precursor and urea as the modifier. *Rsc Advances* **2016,** *6* (40), 33589-33598.

66. Martin, D. J., et al., Highly Efficient Photocatalytic H2 Evolution from Water using Visible Light and Structure-Controlled Graphitic Carbon Nitride. *Angew. Chem., Int. Ed.* **2014,** *53,* 9240-9245.

67. Guo, D., et al., Active sites of nitrogen-doped carbon materials for oxygen reduction reaction clarified using model catalysts. *Science* **2016,** *351* (6271), 361-5.

68. Daems, N., et al., Metal-free doped carbon materials as electrocatalysts for the oxygen reduction reaction. *Journal of Materials Chemistry A* **2014,** *2* (12), 4085-4110.

69. Thomas, A., et al., Graphitic carbon nitride materials: variation of structure and morphology and their use as metal-free catalysts. *J. Mater. Chem.* **2008,** *18* (41), 4893-4908.

70. Briggs, G. B. a. D., *High Resolution XPS of Organic Polymers*. John Wiley and Sons: Chichester, England, 1992.

71. Ma, L. T., et al., A simple melamine-assisted exfoliation of polymeric graphitic carbon nitrides for highly efficient hydrogen production from water under visible light. *Journal of Materials Chemistry A* **2015,** *3* (44), 22404-22412.

72. Xu, J., et al., Chemical exfoliation of graphitic carbon nitride for efficient heterogeneous photocatalysis. *Journal of Materials Chemistry A* **2013,** *1* (46), 14766-14772.

73. Yang, S., et al., Exfoliated graphitic carbon nitride nanosheets as efficient catalysts for hydrogen evolution under visible light. *Adv Mater* **2013,** *25* (17), 2452-6.

74. Han, Q., et al., Facile production of ultrathin graphitic carbon nitride nanoplatelets for efficient visible-light water splitting. *Nano Res.* **2015,** *8* (Copyright (C) 2016 American Chemical Society (ACS). All Rights Reserved.), 1718-1728.

75. Snellenburg, J. J., et al., Glotaran: A Java-Based Graphical User Interface for the R Package TIMP. *J. Stat. Softw.* **2012,** *49* (3), 22.

76. Turro, N. J., et al., *Principles of Molecular Photochemistry: An Introduction*. University Science Books: Sausalito, California, 2009.

77. Elliot, A. J., et al., Estimation of rate constants for near-diffusion-controlled reactions in water at high temperatures. *Journal of the Chemical Society Faraday Transactions* **1990,** *86* (9), 1539-1547.

78. Whited, M. T., et al., Singlet and triplet excitation management in a bichromophoric near-infrared-phosphorescent BODIPY-benzoporphyrin platinum complex. *J Am Chem Soc* **2011,** *133* (1), 88-96.

79. Ariu, M., et al., The effect of morphology on the temperature-dependent photoluminescence quantum efficiency of the conjugated polymer poly(9, 9-dioctylfluorene). *Journal of Physics-Condensed Matter* **2002,** *14* (42), 9975-9986.

80. Zojer, E., et al., Theoretical investigation of the geometric and optical properties of neutral and charged oligophenylenes. *Physical Review B* **1999,** *59* (12), 7957-7968.

81. Delcamp, J. H., et al., Modulating dye E(S+/S*) with efficient heterocyclic nitrogen containing acceptors for DSCs. *Chem Commun (Camb)* **2012,** *48* (17), 2295-7.

82. Zhu, X. Y., How to Draw Energy Level Diagrams in Excitonic Solar Cells. *J Phys Chem Lett* **2014,** *5* (13), 2283-8.

83. Ren, G., et al., Photoinduced Hole Transfer Becomes Suppressed with Diminished Driving Force in Polymer-Fullerene Solar Cells While Electron Transfer Remains Active. *Advanced Functional Materials* **2013,** *23* (10), 1238-1249.

84. Schlenker, C. W.; Thompson, M. E., Current Challenges in Organic Photovoltaic Solar Energy Conversion. In *Unimolecular and Supramolecular Electronics I: Chemistry and Physics Meet at Metal-Molecule Interfaces*, Metzger, R. M., Ed. Springer Berlin Heidelberg: Berlin, Heidelberg, 2012; pp 175-212.

85. Hammer, P., et al., Electronic structure of hydrogenated carbon nitride films. *J Vac Sci Technol A* **1998,** *16* (5), 2941-2949.

86. Hammer, P., et al., Comparative study on the bonding structure of hydrogenated and hydrogen free carbon nitride films with high N content. *Diamond and Related Materials* **2000,** *9* (3–6), 577-581.

87. Hellgren, N., et al., Electronic structure of carbon nitride thin films studied by X-ray spectroscopy techniques. *Thin Solid Films* **2005,** *471* (1–2), 19-34.

88. Zhang, H., et al., Origin of photoactivity in graphitic carbon nitride and strategies for enhancement of photocatalytic efficiency: insights from first-principles computations. *Phys Chem Chem Phys* **2015,** *17* (9), 6280-8.

89. Zuluaga, S., et al., Structural band-gap tuning in g-C3N4. *Physical Chemistry Chemical Physics* **2015,** *17* (2), 957-962.

90. Liu, S., et al., Metal-free melem/g-C3N4 hybrid photocatalysts for water treatment. *J Colloid Interface Sci* **2016,** *464*, 10-7.

91. Meek, G. A., et al., Polaronic Relaxation by Three-Electron Bond Formation in Graphitic Carbon Nitrides. *Journal of Physical Chemistry C* **2014,** *118* (8), 4023-4032.

92. Braml, N. E., et al., Synthesis of triazine-based materials by functionalization with alkynes. *Chemistry* **2015,** *21* (21), 7866-73.

Chapter 4. Barrierless Heptazine-Driven Excited-State Proton-Coupled Electron Transfer: Implications for Controlling Photochemistry of Carbon Nitrides and Aza-Arenes

Reprinted (adapted) with permission from J. Phys. Chem. C.
DOI: 10.1021/acs.jpcc.9b08842 Copyright 2019 American Chemical Society.

4.1 INTRODUCTION

Concerted motion of protons and electrons is critical for a variety of chemical transformations relevant for applications spanning energy storage[1] to municipal wastewater treatment.[2] Recently, there has been mounting world-wide interest in deploying molecular and polymeric organic constructs as photoredox catalysts to drive these transformations using photons.[3-5] In order to utilize solar energy in such processes, it is desirable to understand what molecular properties control the efficiency of inter-molecular excited-state proton-coupled electron transfer (ES-PCET) reactions. The majority of inter-molecular ES-PCET literature to date focuses on metal-containing complexes,[6-9] with fewer examples of all-organic chromophores,[10-12] despite their photophysical properties being extensively studied over the past century.[3-4, 13-15] Precious metal-containing catalysts have become promising candidates, in part, due to their long-lived excited state lifetimes ranging from hundreds of nanoseconds to microseconds.[16] However, identifying earth-abundant alternatives continues to be a compelling challenge to overcome. We have elected to examine all-organic materials with long excited-state lifetimes and good photostability. Recently, the nitrogen-rich heptazine (Hz) unit has garnered increased attention for applications in photocatalytic hydrogen production.[5, 17-19] The mechanism of molecular Hz driving ES-PCET has been studied computationally,[20-22] and our group reported the first experimental evidence for this processes resulting in neutral radical species.[23] This Hz-based chromophore exhibits a singlet lifetime of roughly 300 ns, the same order of magnitude as $[Ru(bpy)_3]^{2+}$, a compound which is ubiquitous in the study of photochemical transformations.[16, 24] Interestingly, this 300 ns lifetime is significantly longer than first row transition metal complexes[25] as well as traditional strongly-absorbing organic chromophores, which typically have lifetimes of no more than tens of nanoseconds.[26] Additionally, we previously reported computational and experimental evidence that Hz derivatives can exhibit an extremely unusual inversion of the energies of their lowest singlet and triplet excited states.[27] This peculiar violation of Hund's multiplicity rule stands in contrast to virtually all other classes of known organic compounds. With the lowest lying excited state being a singlet rather than a triplet, the sensitization of singlet oxygen appears to become an inaccessible decay pathway for Hz-based chromophores. Those results imply that Hz molecules should enjoy unique photostability in the presence of oxygen. This is important because typical organic photocatalysts achieve the long excited-state lifetimes necessary to outlast slow diffusive processes by accessing the triplet manifold through efficient intersystem crossing. Unfortunately, relying on triplet molecular photoexcitations relegates the use of such chromophores to anaerobic environments in order to avoid destroying the photocatalyst by sensitizing highly reactive singlet oxygen.

Herein, we provide further mechanistic insights into inter-molecular ES-PCET using 2,5,8-tris(4-methoxyphenyl)-1,3,4,6,7,9,9b-heptaazaphenalene (TAHz) with a series of phenol (PhOH) derivatives as proton and electron donors, shown in Figure 4-1. By altering the functional group on PhOH, we monitor the effect of redox potential and hydrogen-bonding on the mechanism of the resulting photochemical reaction.[28-32] In particular, we consider the energy of the intermolecular charge transfer (CT) states that form in these complexes and the corresponding excited state reaction barrier heights. For each PhOH, we determine a quenching rate constant (k_Q)

of excited TAHz, an association constant (K_A), and a kinetic isotope effect (KIE) of excited-state deactivation with R-PhOH versus R-PhOD.

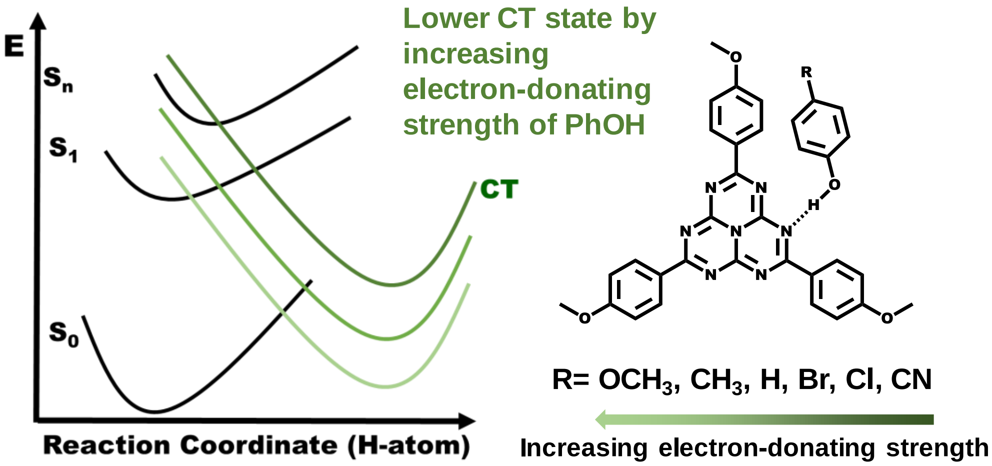

Figure 4-1. A cartoon depicting the proposed excited-state landscape.
This is depicting the landscape along the H-atom transfer coordinate from phenol (PhOH) to TAHz. As proposed previously, there exists a charge transfer (CT) state in which an electron has moved from the oxygen atom of PhOH to the heptazine core and which can drive proton motion after the CT has occurred. Previous studies with TAHz and water suggest that the CT state was accessible from the S_n states. We believe the energy curve of the CT state can be lowered by adding electron-donating groups on the H-atom donor. In this study we do this by using the series of R-PhOH derivatives shown.

As the electron-donating strength of the para-substituent, R, on R-PhOH is increased, we observe an increase in quenching rate constant accompanied by a decrease in KIE. Using *ab initio* quantum chemical calculations to examine the energy landscape for the interaction of the Hz core with the same series of PhOHs, we observe the same trend, wherein the transition state barrier for the photoinduced reaction decreases until the photon-driven reaction becomes completely barrierless for the most electron-donating PhOH. By using time-resolved photoluminescence measurements and global analysis, we can separately monitor hydrogen-bonded and free TAHz emission. Correspondingly, we observe no evidence for emission from hydrogen-bound complexes in the case of OCH_3-PhOH, consistent with barrierless excited-state reactivity. This photochemical reactivity information provides new insight that synthetic chemists and materials scientists can deploy to outline new molecular design strategies targeting Hz-based photocatalysis.

4.2 RESULTS AND DISCUSSION

I. Association constants for hydrogen-bonding

We observe evidence of hydrogen bonding in the ground-state absorption spectra of TAHz with and without PhOH present, as shown in Figure 4-2a. Upon hydrogen-bonding, we see a redshift in the bright $\pi \rightarrow \pi^*$ transition, labeled "Peak 1." At lower energies, we observe a blueshift of the weakly allowed transitions with $n \rightarrow \pi^*$ character, labeled "Peak 2." Figure 4-3b shows the magnitude of the peak shift as a function of the pKa of the PhOH derivative. PhOHs with electron-donating substituents, such as CH_3-PhOH and OCH_3-PhOH, show only small shifts whereas CN-PhOH displays a significantly larger shift at 50 mM PhOH concentrations. This suggests that the hydrogen bonding strength is not equal across the series of PhOH derivatives. The calculations (see Section IV) indeed show that the length of the hydrogen bond between the OH group of PhOH and the acceptor N-atom of Hz (R_{NH}) is 1.937 Å in the Hz-PhOH complex. R_{NH} increases to 1.943 Å for the strongest electron donating substituent (OCH_3) and decreases to 1.904 Å for the strongest electron withdrawing substituent (CN), see

Table 4-1. As is well known, the length of the hydrogen bond is a proxy for the strength (binding energy) of the latter. In order to quantify these differences from the experimental side, we determined the association constant between TAHz and each of the six PhOH derivatives. We employed the method previously used by the Hammarström group to fit the saturation behavior of the changing ground state absorption as a function of PhOH concentration.[33-34] Figure 4-2c shows the change in absorption spectra for TAHz with increasing PhOH concentrations. Figure 4-2d plots the change in optical density as a function of PhOH concentration, showing a clear saturation behavior. Fitting this data to the following equation allows us to extract a K_A value for TAHz-PhOH in the ground state.

Eq. 1:

$$\frac{\Delta A}{l} = \Delta\varepsilon_{380}\left(\frac{[TAHz]_0 + [PhOH]_0 + K_A^{-1}}{2}\right)\overset{(+)}{-}\sqrt{\left(\frac{[TAHz]_0 + [PhOH]_0 + K_A^{-1}}{2}\right)^2 - [TAHz]_0[PhOH]_0}$$

Here ΔA is the change in absorption at a given wavelength, *l* is the path length of the cuvette, $\Delta\varepsilon_{380}$ is the difference in molar absorptivity at 380 nm between the bound TAHz-PhOH complex and free TAHz chromophore, $[TAHz]_0$ and $[PhOH]_0$ are the initial concentrations of TAHz and PhOH, respectively.

We have estimated the K_A values for the six PhOH derivatives with TAHz in

Table 4-1 (see Appendix B for fits). As expected, we see an increased K_A for PhOHs with electron-withdrawing substituents with the largest being for CN-PhOH. Notably, there is a very small difference between the K_A values for PhOH, CH_3-PhOH, and OCH_3-PhOH despite there being a significant difference between the oxidation potentials of these PhOHs. The computed ground-state hydrogen-bond lengths follow the same trend.

To determine how these ground state electrochemical and hydrogen-bonding properties affect the photochemical reactivity and excited state barrier height, we turn to photoluminescence quenching and *ab initio* computational studies.

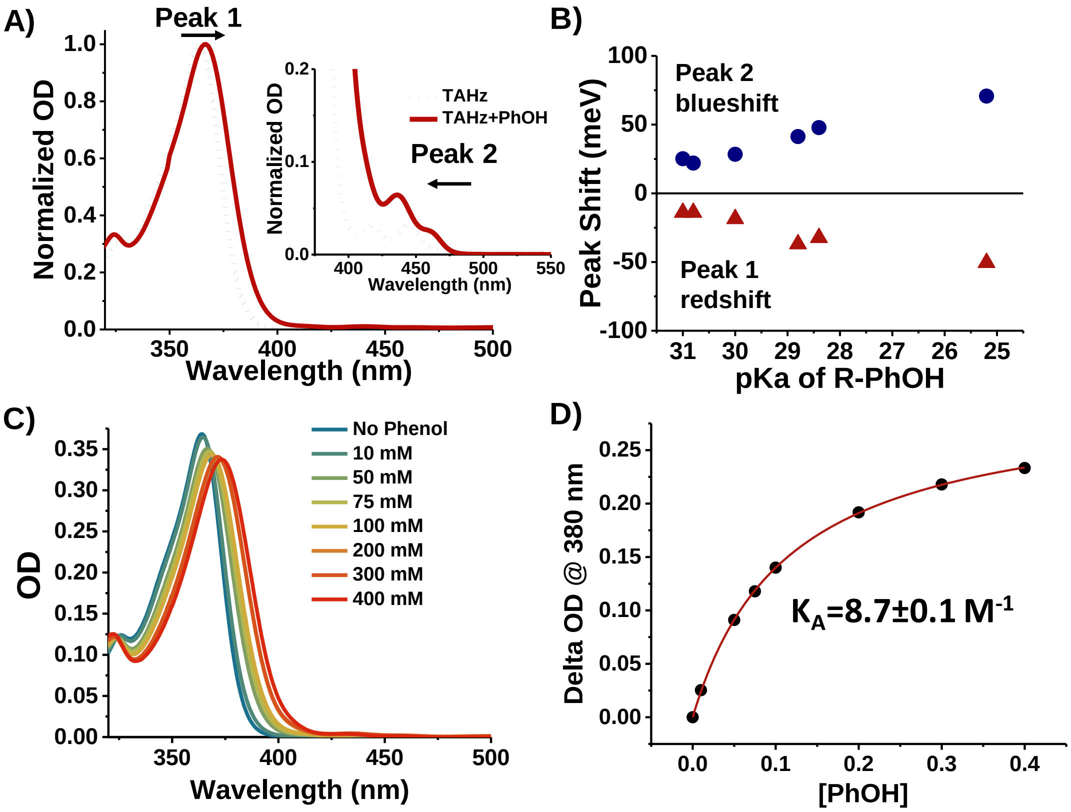

Figure 4-2. Ground state absorption shifting as a function of phenol concentration.
A) The addition of phenol (PhOH) changes the ground state absorption of TAHz in toluene, suggesting hydrogen-bonding. A distinct redshift of the main absorption can be seen from TAHz in toluene without PhOH present (black dotted line) upon the addition of 100 mM PhOH (solid red line). The weakly allowed transitions at lower energies, on the other hand, show a blueshift upon addition of PhOH, shown in the inset. B) The peak shifts of TAHz absorption with 100 mM of R-PhOH as a function of the PhOH's pKa (in DMSO) shows a largely linear trend. This suggests that different PhOHs have different hydrogen bonding strengths with TAHz. C) Absorption traces at different PhOH concentrations shows a saturation behavior towards the absorption of the TAHz-PhOH complex. D) Fit of ΔOD at 380 nm to determine K_A for TAHz and PhOH to be 8.7 M^{-1}.

II. Quenching constants for PhOH derivatives

To monitor the quenching rate of the TAHz S_1 state with varying PhOH derivatives, we performed Stern-Volmer quenching analysis using both PL intensity and lifetime quenching data, shown in Figure 4-3a and Figure 4-3b, respectively.

Table 4-1 shows all the k_Q values for the six different PhOHs (see Section SIII) and calculated KIE values for the S_1 lifetime with R-PhOH/D. As expected, increasingly anodic oxidation potentials of the R-PhOH lead to smaller k_Q values, suggesting a kinetic barrier has been introduced along the photochemical reaction pathway. This is confirmed by the increasing KIE values with decreasing $k_{Q,}$ suggesting proton motion must couple to electron motion for the reaction to proceed, most likely by a tunneling mechanism.

The calculated k_Q values from the two methods (intensity and lifetime) are close for PhOH, but the intensity quenching shows a slightly greater rate constant. We attribute this to the fact that intensity analysis can reflect both static and dynamic quenching, whereas lifetime analysis only captures the rate of dynamic quenching. We note that for PhOH derivatives with low K_A values and low oxidation potentials, we see a greater difference between the k_Q values we obtain from lifetime measurements compared with intensity measurements. One explanation could be, in this case, that complex formation is the rate determining step as opposed to ES-PCET. Whereas in the case of CN-PhOH, K_A is large but the driving force for electron transfer is low, so the rate of ES-PCET is rate determining. In this case, the intensity and lifetime quenching are the same as they both report on the rate of ES-PCET.

It is worth noting that we observe a two-component PL lifetime in the presence of PhOH, in contrast to the monoexponential decay of TAHz in neat toluene. We attribute the fast decay to the emission of hydrogen-bound complexes, as has been observed for coumarin complexes previously.[28]

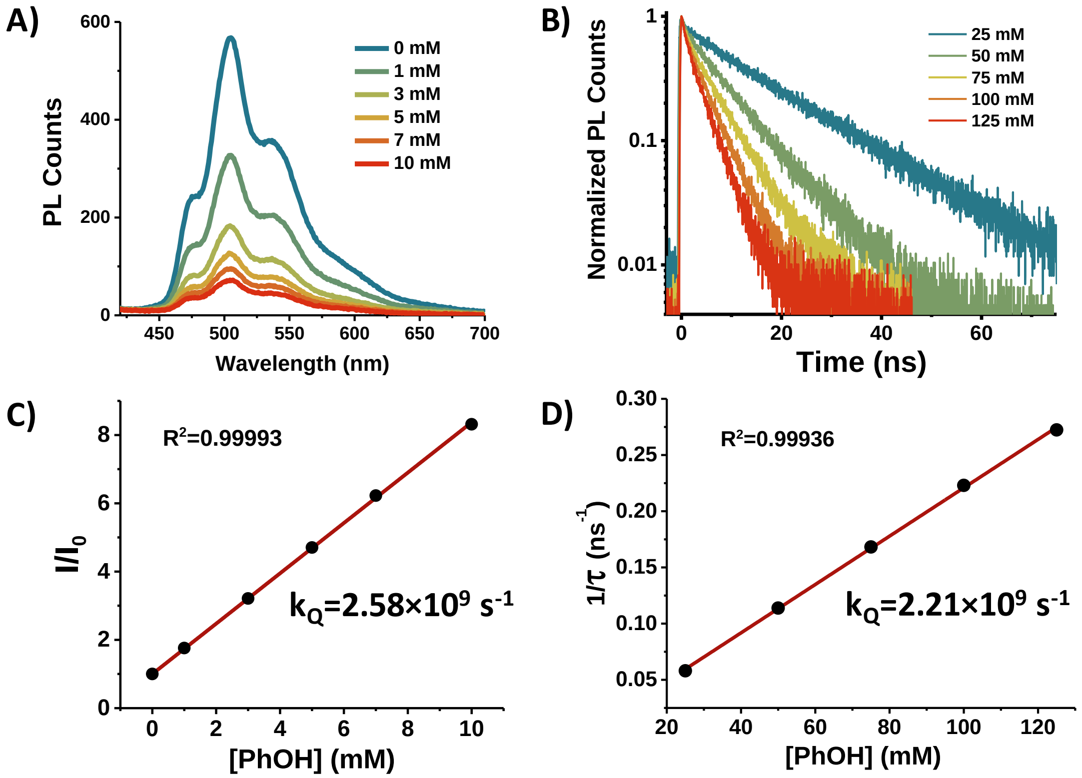

Figure 4-3. TAHz photoluminescence quenching as a function of phenol concentration.
A) Photoluminescence (PL) intensity quenching of TAHz shows significant static quenching with increasing concentrations of phenol (PhOH). B) PL lifetimes of TAHz with increasing concentrations of PhOH show dynamic quenching. Stern-Volmer analysis shows a straight line for both the (C) PL intensity quenching and (D) luminescence lifetime, fit after 5 ns.

Table 4-1. Comparison of key parameters determining hydrogen bonding and ES-PCET in complexes of TAHz or Hz with phenol (PhOH) derivatives.

R	E_0 (RPhOH$^+$/ RPhOH)[†]	pK_a PhOH[§]	k_Q (x10^9 s^{-1}) TCSPC	k_Q (x10^9 s^{-1}) PLQY	K_A (M^{-1})	S_1 KIE[*]	R_{NH} (Å)[♦]	$\Delta E^‡$ (eV)[♦]
CN	2.03	13.2	0.556	0.532	~87.4	1.9	1.904	0.369
Cl	1.88	16.75	2.78	2.80	17.2	1.4	1.924	0.169
Br	1.86	16.36	2.73	3.06	19.1	1.4	1.923	0.177
H	1.88	18.0	2.21	2.58	8.7	1.5	1.937	0.167
CH_3	1.79	18.9	4.21	5.14	8.9	1.2	1.940	0.093
OCH_3	1.68	19.1	4.26	5.23	8.9	1.1	1.943	----

[†] Versus SHE in ACN (±0.1 V)[31, 35]

[§] In DMSO[32]

[*] All R-PhOH concentrations 50 mM

[♦] From *ab initio* calculations, see Section IV

III. Time-resolved photoluminescence

Using time-resolved photoluminescence spectra in tandem with global analysis, we analyzed the nature of the fast PL decay component mentioned above. Figure 4-4a shows the PL spectral traces of TAHz in a 100 mM PhOH solution at early (500 ps) and late (5 – 7 ns) times. Though the spectral difference is small, the increased intensity near 475 nm at early times does not appear for TAHz in neat toluene (Figure B-14). Figure 4-4b clearly shows different decay rates in the spectral range 450 – 475 nm in contrast to 500 – 525 nm, indicating that at least two separate luminescent species are present.

To kinetically resolve these overlapping emission features, we apply global target analysis. We model total PL intensity $\Theta(t,\lambda)$ at time t and wavelength λ as a sum of concentration-weighted spectral components such that $\Theta(t,\lambda)=\Sigma c_i(t)\sigma_i(\lambda)$, where $c_i(t)$ and $\sigma_i(\lambda)$, respectively, correspond to the time-dependent concentration and wavelength-dependent species-associated emission spectrum (SAES) of the i^{th} emissive species.[36] Global target analysis yields two kinetically resolvable emission features, shown in Figure 4c. The spectral trace at higher energies decays at a significantly faster rate, on the order of hundreds of picoseconds. We attribute this emission spectrum to that of a hydrogen-bonded TAHz-PhOH complex. The blueshift in emission corresponds to the blueshift of the low-lying and weakly-allowed transitions that appear in the absorption spectra in Figure 4-2a. Considering the $n\pi^*$ character of these low energy transitions, we would expect to see a blueshift for the emission of this state. It is also interesting to note that the vibronic structure is more pronounced for the fast component than for the slow component, although the peak spacings appear similar.

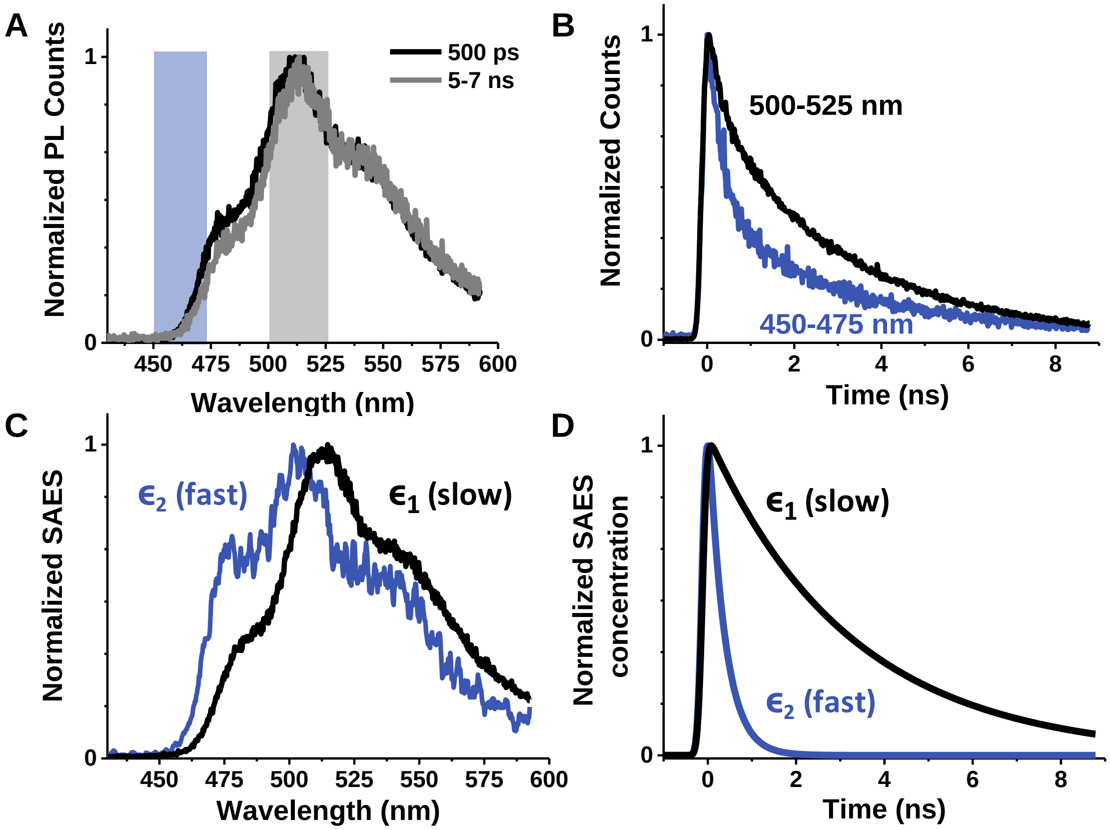

Figure 4-4. Time-resolved photoluminescence (TR-PL) measurements of TAHz with phenol. A) Spectral traces averaged over the first 500 ps (black) and 5 to 7 ns (gray) show a small spectral change. B) The kinetic decay traces averaged from 450-475 nm (blue) and 500-525 nm (black) suggest at least two kinetically distinct luminescent species. C) and D) Global target analysis of the TR-PL data shows two species associated emission spectra (SAES). Emission attributed to the S_1 state, labeled ϵ_1 (black), is the emission shape seen in steady-state measurements and has a lifetime of 3.23 ns. The second SAES, labeled ϵ_2 (blue), is seen at higher energies and decays notably faster than ϵ_1 with a lifetime of 0.36 ns. All experiments shown were done with 50 µM TAHz with 100 mM phenol.

To probe whether this state is associated with hydrogen bonding between TAHz and PhOH, we monitor the relative amplitude of the emission signal for this high energy species as a function of PhOH concentration. While Figure 4-5b shows that the spectral shape does not change for either species, Figure 4-5c reveals the relative intensity of the high energy features increases with increasing concentrations of PhOH. This intensity/concentration correlation strongly suggests that the high energy emission results from a hydrogen-bonded TAHz-PhOH complex. This distinction between hydrogen bonded and free TAHz emission allows us to monitor the two populations separately for the different PhOH derivatives. We observe and kinetically resolve high energy emission spectra for all PhOHs that we have examined, with the exception of OCH_3-PhOH, for which this emission feature is absent on our experimental timescale (more discussion in Appendix B). We attribute this absence to barrierless reactivity from the S_1 state (vide infra). Such barrierless reactivity for OCH_3-PhOH would be consistent with this derivative possessing the lowest anodic oxidation potential and exhibiting no significant KIE. In the photoexcited TAHz and OCH_3-PhOH complex, the rate of reaction far outcompetes the rate of fluorescence. Therefore, the only emission we observe is from unbonded TAHz chromophores. The quenching rate of this free TAHz then becomes diffusion limited for the chromophore and OCH_3-PhOH in the solution.

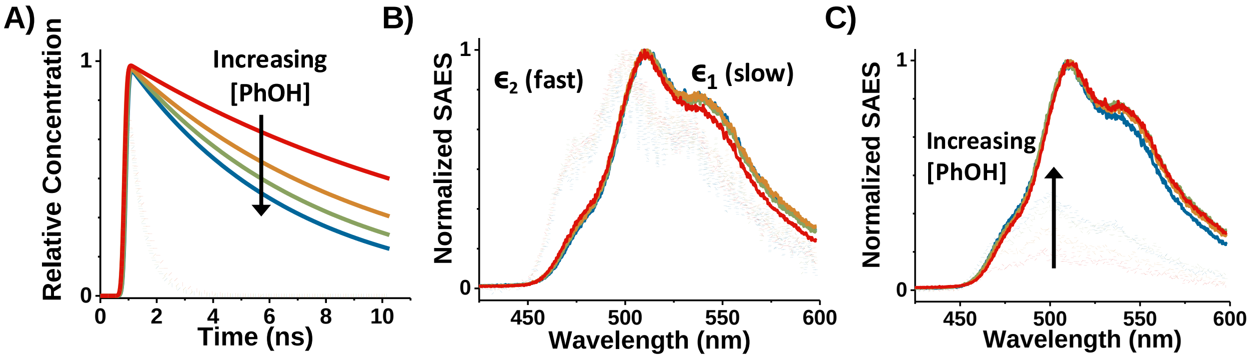

Figure 4-5. Phenol (PhOH) concentration-dependent TR-PL suggesting that the high energy emission is from a hydrogen-bonded complex.
A) Kinetic decay rates of bonded TAHz S_1 (solid) hydrogen-bonded TAHz-PhOH (dotted) with different PhOH concentrations: 25 mM (red), 50 mM (orange), 75 mM (green), and 100 mM (blue). B) Normalized SAES showing spectral shape isn't changing significantly. C) High energy emission grows in with [PhOH] relative to low-energy emission.

IV. Computational studies of Hz-PhOH complexes and their potential energy surfaces

The ground-state equilibrium geometries of the hydrogen-bonded complexes of Hz with PhOH and derivatives thereof were determined with the second-order Møller-Plesset (MP2) method. Vertical electronic excitation energies and excited state potential energy surfaces were computed with the second-order algebraic-diagrammatic-construction (ADC(2)) method.[37] ADC(2) is a wave-function based single-reference propagator method which provides, in contrast to time-dependent density functional theory (TDDFT) with various functionals, an accurate and balanced description of locally excited (LE) states and CT states, which is essential for the determination of reliable *ab initio* potential energy surfaces for ES-PCET reactions. The complex of TAHz with PhOH is too big for wave-function based excited state *ab initio* calculations. All *ab initio* calculations were therefore performed for complexes of the Hz core of TAHz with PhOH and its derivatives.

The most relevant nuclear coordinates for PCET processes are the H-atom transfer coordinate (chosen here as the OH bond length R_{OH} of the hydrogen-bonded PhOH molecule) and the distance R_{ON} between the oxygen atom of PhOH and the H-atom accepting nitrogen atom of Hz. For fixed R_{OH} and R_{ON}, the energy of the lowest excited singlet state was minimized with respect to all other nuclear coordinates of the complex. This procedure yields a two-dimensional (2D) relaxed potential energy surface for the PCET reaction. The saddle point (transition state) on this 2D relaxed surface was located and used as the starting guess for a full optimization of the transition state with the ADC(2) method. Analysis of the eigenvalues of the Hessian confirmed that there was only a single imaginary frequency, implying a first-order saddle point. The difference between the energy of the transition state and the energy minimum of the S_1 state in the Frank Condon (FC) zone defines the reaction barrier $\Delta E^{\ddagger}$. The reaction barriers are listed in Table 4-1.

Figure 4-6A shows the two-dimensional relaxed S_1 potential energy surface of the Hz-PhOH complex. For small OH distances, the H-atom is covalently bonded to the oxygen atom of PhOH and forms a hydrogen bond with a peripheral nitrogen atom of Hz. For large OH distances, on the other hand, the H-atom is covalently bonded to the nitrogen atom of Hz (forming the heptazinyl (HzH) radical) and is hydrogen bonded with the phenoxy (PhO) radical. The 2D relaxed energy surface clearly exhibits two minima. The minimum for small OH distances is the energy minimum of the LE state in the FC region (indicated by the white circle in Figure 4-6A). The second minimum at large OH distances (indicated by the white square in Figure 4-6A) represents the HzH-PhO biradical. For the ES-PCET transfer to occur, the photoexcited complex must overcome the barrier separating the two minima, which is indicated by the triangle in Figure 4-6A. At the saddle point, the wave function of the S_1 state changes from a $\pi\pi^*$ state of LE character to a $\pi\pi^*$ state of CT character. For the Hz-PhOH complex, the energy of the saddle point is 2.68 eV above the energy minimum of the S_0 state and the barrier height is 0.167 eV.

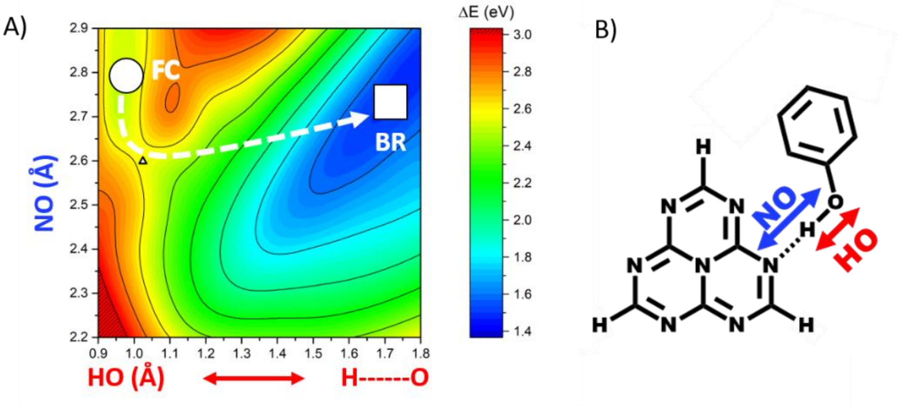

Figure 4-6. 2D relaxed potential energy surface of the S_1 excited state of the heptazine-phenol (Hz-PhOH) complex computed at the ADC(2) level.
The reaction coordinates are the OH bond length of PhOH and the distance between the O-atom of PhOH and N-atom of Hz, see (B). The circle designates the energy minimum of the locally excited (LE) state in the Frank Condon (FC) region. The square indicates the equilibrium geometry of the HzH···PhO biradical (BR) formed by H-atom transfer. A saddle point (marked by the triangle) separates the two energy minima.

Figure 4-7 shows the 2D relaxed S_1 energy surfaces of the Hz-CN-PhOH (A) and Hz-OCH_3-PhOH (B) complexes. These are the systems with the highest (Hz-CN-PhOH) and lowest (Hz-OCH_3-PhOH) barrier for the ES-PCET reaction. For CN-PhOH-Hz, the energy of the transition state is 2.89 eV above the S_0 energy minimum and the height of the barrier of the PCET reaction is 0.369 eV. The comparatively high barrier is a consequence of the electron-withdrawing character of the cyano (CN) group of the Hz-CN-PhOH complex, which leads to a blue shift of the CT state compared to the Hz-PhOH complex ($\mathbf{E}_{\mathbf{CT}}^{\mathbf{GS}}$ = 3.86 eV, see Table B-1 in Appendix B). The methoxy (OCH_3) group of the OCH_3-PhOH complex (Figure 4-7B), on the other hand, is a relatively strong electron-donating group which causes a substantial red shift of the CT state ($\mathbf{E}_{\mathbf{CT}}^{\mathbf{GS}}$ = 2.80 eV, see Table B-1 in Appendix B). The vertical excitation energies of the CT states of Hz-CN-PhOH and Hz-OCH_3-PhOH differ by the amazing amount of more than 1.0 eV. For Hz-OCH_3-PhOH, the red shift of the CT state is large enough to eliminate the barrier on the S_1 potential energy surface, see Figure 4-7B. The theoretically predicted barrierless ES-PCET reaction matches the experimental observations for OCH_3-PhOH: no observable fast PL component attributable to a hydrogen-bonded complex and no significant KIE.

Additional *ab initio* data (vertical excitation energies of the LE and CT states and vibrational stabilization energies of the LE state) are collected in Table B-1 in Appendix B. The molecular structures of the transition states of the six Hz-R-PhOH complexes are displayed in Figure B-22 in Appendix B. The lengths of the OH···N hydrogen bonds at the transition state are specified in this figure. While the vertical excitation energies of the S_1 states, E_1^{GS}, and the minimum-to-minimum excitation energies of the LE states, E_1^{min}**,** differ by merely 0.02 eV, the energies of the transition state, E_1^{TS}, vary substantially for the substituents R on PhOH, resulting in a significant variation of the barrier height $\Delta E^{\ddagger}$. The stronger the electron-donating character of the substituent, the lower the barrier. Importantly, the barrier height $\Delta E^{\ddagger}$ and the vertical excitation energy of the CT state, $\mathbf{E}_{\mathbf{CT}}^{\mathbf{GS}}$, are strongly correlated. While the latter decreases by about 1.0 eV from the CN substituent to the OCH_3 substituent, the barrier height changes by 0.37 eV. These findings imply that the vertical excitation energy of the CT state can be used as a proxy for the relative barrier height in future *ab initio* screening studies of carbon nitride photocatalysts.

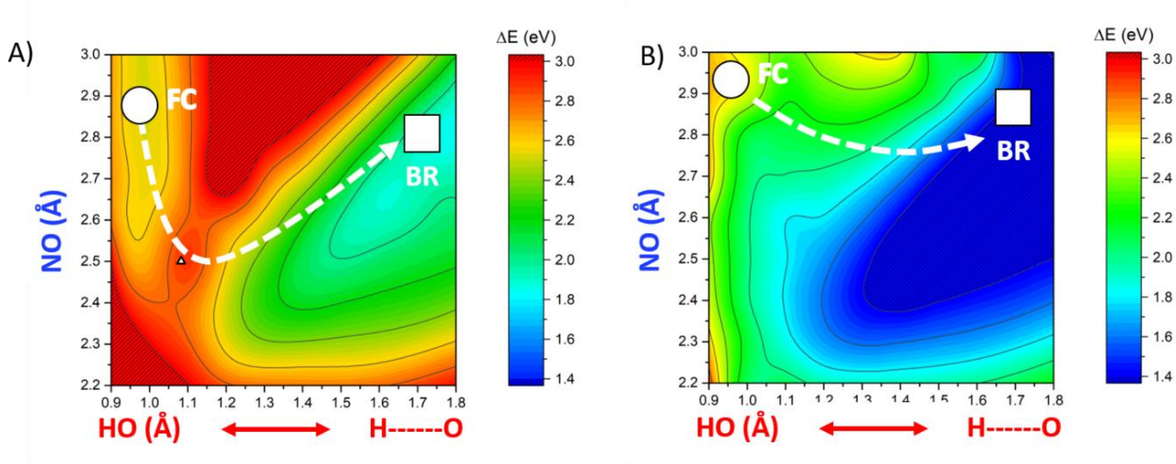

Figure 4-7. 2D relaxed potential energy surface of the S_1 excited state of the heptazine-cyanophenol complex.
(A) and the heptazine-methoxyphenol (B) complexes computed at the ADC(2) level. See caption of Figure 4-6 for the definition of the reaction coordinates. The heptazine-methoxyphenol complex (B) exhibits a barrierless S_1 potential energy surface.

V. Implications for molecular design

While the limited solubility of TAHz restricts our ability to reliably estimate pK_a and ΔG_{PCET} values, we can readily infer that proton motion must play a significant role in the photochemical reactivity of TAHz since the excited state reduction potential of the free chromophore is 1.48V vs SHE. Comparing the potentials for the isolated half reactions, this reduction potential would be insufficient to drive oxidation of any of the PhOHs in the series that we have studied here. Fortunately, we can glean critical insight by examining *ab initio* computational results for the barrier height $\Delta E^{\ddagger}$ of the ES-PCET reaction from PhOH to the Hz core. The computed $\Delta E^{\ddagger}$ values exhibit a reasonable correlation with the rate constants for excited state quenching plotted in Figure 4-8. We observe that the greater the degree of electron-donating character of the substituent on the PhOH, the lower the value of $\Delta E^{\ddagger}$, and the faster the excited-state quenching. This trend suggests that chemically inverting this effect by appending strongly electron-withdrawing moieties to the heptazine core, could significantly increase the rate constant for the ES-PCET reaction of a hydrogen-bonded Hz-water complex. However, it is interesting to note that for PhOH derivatives with similar oxidation potentials, Cl-PhOH, PhOH, and Br-PhOH, the effect of hydrogen bonding is evident. The PhOHs with lower pKa's have larger K_A values, stronger hydrogen bonds and greater quenching rate constants. Achieving efficient intermolecular ES-PCET in hydrogen-bonded aza-arene-water complexes could lay the groundwork to kick off a variety of future applications with the potential to utilize compelling reactions with these photogenerated hydroxyl and heptazinyl radical species, including hydrogen production, CO_2 reduction, and municipal waste-water decontamination.

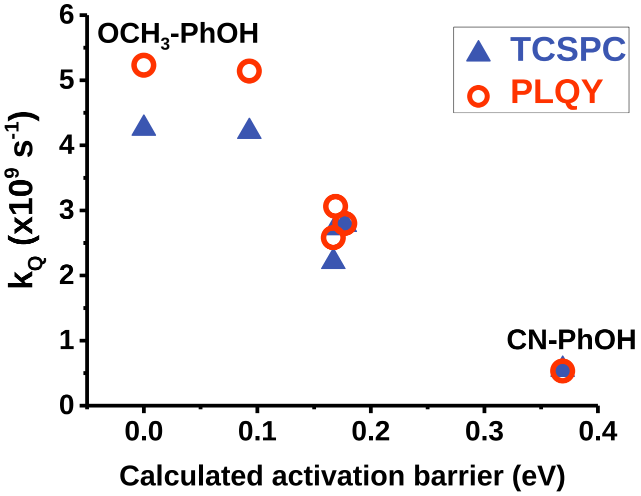

Figure 4-8. Correlation between the calculated activation barrier and the excited-state quenching rate constants.

Quenching rate constants were determined by PLQY (red open circles) and TCSPC (blue triangles). Overall, we see a significant increase in the excited-state quenching rate as the phenol substituent becomes more electron-donating. We see a greater difference between the two methods as the calculated activation barrier decreases, indicating that the rate of ES-PCET is limited by diffusion and complex formation.

4.3 CONCLUSIONS

We hypothesized that the rate of ES-PCET of heptazine chromophores and hydroxylic compounds could be controlled by tuning the excited state barrier height for H-atom abstraction. We have proposed that this tunability could be achieved by adding electron-donating groups to the hydroxylic compound (Figure 4-1). We present a combined experimental and theoretical study to assess the validity of such a design strategy by adding electron-donating groups to PhOH, acting as a model hydroxylic species. In support of our hypothesis, we observe increased quenching rate constants for PhOH derivatives with more electron-donating substituents. The ES-PCET reactivity is found to be governed by the barrier height $\Delta E^{\ddagger}$ on the potential energy surface of the long-lived S_1 state of the TAHz-PhOH complex, which in turn scales with the vertical excitation energy of the Hz-to-PhOH CT state. In the case of the most electron-donating PhOH, OCH$_3$-PhOH, we computationally predict and experimentally verify that the excited state H-atom transfer reaction becomes barrierless in the S_1 excited state of the hydrogen-bonded complex. This increased reactivity does not come at a significant cost of hydrogen-bonding as the K_A for TAHz-OCH_3-PhOH and TAHz-PhOH are essentially the same.

It is common practice in photocatalytic hydrogen evolution experiments, for example with g-C_3N_4 photocatalysts, to use sacrificial electron donors such as triethanolamine (TEOA), triethylamine (TEA), or methanol.[5] While TEOA and TEA are the most widely employed sacrificial electron donors in this context, a systematic investigation of the mechanistic role of different sacrificial electron donors apparently has not been performed. Herein, we presented a systematic and theory-supported analysis of the ES-PCET reactivity for the TAHz photocatalyst with substituted PhOHs as sacrificial electron donors. The oxidation potentials E_0 of the electron donors vary from 1.40 eV (CN-PhOH) to 1.05 eV (OCH_3-PhOH) (

Table 4-1). The *ab initio* computed reaction barriers vary from 0.369 eV for CN-PhOH to zero (no barrier) for OCH_3-PhOH, following closely the trend of the oxidation potentials. While it is comparatively easy to photo-oxidize sacrificial electron donors with low oxidation potentials, the challenge consists in the efficient photo-oxidation of water molecules with visible light. Rather than lowering the oxidation potential of the solvent, the reduction potential of the photocatalyst should be increased such that hydrogen-bonded water molecules can be oxidized in a barrierless and therefore efficient ES-PCET reaction. We conjecture that this can be achieved with Hz-based photocatalysts by adding strong electron withdrawing groups to the Hz core. Synthetic efforts guided by *ab initio* electronic structure-calculations are currently underway in our laboratories to experimentally develop this scenario. Interesting questions remain regarding the nature of the proton-transfer mechanism (tunneling vs. barrier-crossing) and the fate of the radicals that are produced.

4.4 EXPERIMENTAL METHODS

Reagents. Urea, potassium hydroxide, phosphorous oxychloride, phosphorous pentachloride, phenol, and deuterated methanol (MeOD) were all purchased from Sigma Aldrich. Anisole (99%) was purchased from Alfa Aesar. Aluminum chloride was purchased from Fischer Scientific. 4-methoxyphenol, 4-bromophenol, p-cresol (4-methylphenol), 4-chlorophenol, and 4-hydroxybenzonitrile (4-cyanophenol) were all purchased from TCI. All reagents were used without further purification.

Sample Preparation. TAHz was dissolved in toluene (100 μM) and stirred overnight before measurements were preformed to ensure minimal aggregation effects and accurate concentrations were prepared. Samples were kept in the dark until measurements were performed.

Ground State Absorption. Ground-state absorption spectra were collected with a Cary5000 UV−vis−NIR spectrometer. Within each R-PhOH series, the same TAHz stock solution was used to ensure consistent TAHz concentration with the varying phenol concentrations.

Time-Correlated Single-Photon Counting (TCSPC). Unless otherwise stated, TCSPC PL lifetimes were measured using a PicoQuant FluoTime 100 with a 375 nm laser diode excitation. Lifetimes measured out to 2 μs were triggered using an external function generator at 500 kHz.

Photoluminescence Quantum Yields. PLQY’s were measured on a Hamamatsu external quantum efficiency measurement system (C9920-12). All PLQY’s reported were excited with 365 nm light and the PL was integrated from 440 to 800 nm.

Time-Resolved Photoluminescence (TR-PL) Spectra. TR-PL spectra were collected using a Hamamatsu streak camera (C10910) with a slow-sweep unit (M10913-01) in photon counting mode. Samples were irradiated with 50 fs pulses at 365 nm and 1 kHz pump from a Coherent/Light Conversion OPerA solo optical parametric amplifier (OPA). Pump fluences were $2.7\text{x}10^{13}$ photons cm^{-3} unless otherwise stated.

Synthesis.

Graphitic carbon nitride: Briefly, urea (10 g) was heated in a porcelain crucible (20 mL) using a potter's kiln at 500 °C for 3 h, with a ramp rate of 30 °C per hour under ambient atmosphere. The light-yellow product was ground thoroughly with a mortar and pestle prior to use in further reactions.

Potassium cyamelurate: 4.5 g of graphitic carbon nitride was refluxed in KOH (3.0 M, 150 mL) for 6 h. The solution was hot filtered over a glass frit and then cooled for recrystallization. The resulting white crystals were filtered and washed with cold ethanol.

Cyameluric chloride: Phosphorous oxychloride (35 mL) was added to a flame-dried round-bottom flask with a stir bar. Phosphorous pentachloride (4.6 g) was added and allowed to stir for 5 minutes. Potassium cyamelurate (2.0 g) was added and the suspension was refluxed under N_2 at 110°C for 6 hrs. $POCl_3$ was removed under reduced pressure using a distillation set-up in the fume hood. The remaining solution was put on ice and ice water (50 mL) was added dropwise while stirring. The product was vacuum filtered and washed with ice-cold water. The resulting product was dried under vacuum for a few hours and stored in a desiccator. Safety note: $POCl_3$ and PCl_5 react with water exothermically to produce HCl gas and H_3PO_4. Always keep these reagents in a ventilated chemical fume hood and quench slowly with sodium bicarbonate.

2,5,8-tris(4-methoxyphenyl)-1,3,4,6,7,9,9b-heptaazaphenalene (TAHz): Anisole (10 mL) was purged with nitrogen for at least 15 minutes. Aluminum chloride (4.0 g) was added to the flask and allowed to stir for a few minutes at 60°C. Cyameluric chloride (1.0 g) was added slowly over

30 minutes. The reaction mixture was stirred at 60°C under nitrogen for 5 hours. Deionized water (25 mL) was added and the solution was stirred until the color changed to yellow and the large chunks dissolved. The resulting bright yellow powder was filtered and washed with ice cold water. The product was purified by slowly recrystallizing in hot DMSO. Characterization of TAHz is shown in our previous manuscript.[23]

Deuterating phenols were done according to literature precedent.[38] Briefly, 0.5 g of each phenol was dissolved in deuterated methanol (MeOD) in a dried round bottom flask and stirred for 1 hour. Methanol was removed under vacuum and the procedure was repeated a second time to give the deuterated phenol. The product was confirmed by ^{1}H-NMR to be >80% deuterated.

4.5 REFERENCES

1. Mora, S. J., et al., Proton-Coupled Electron Transfer in Artificial Photosynthetic Systems. *Acc. Chem. Res.* **2018,** *51* (2), 445-453.
2. Wang, J. L.; Xu, L. J., Advanced Oxidation Processes for Wastewater Treatment: Formation of Hydroxyl Radical and Application. *Critical Reviews in Environmental Science and Technology* **2012,** *42* (3), 251-325.
3. Pearson, R. M., et al., Organocatalyzed Atom Transfer Radical Polymerization Using N-Aryl Phenoxazines as Photoredox Catalysts. *J. Am. Chem. Soc.* **2016,** *138* (35), 11399-11407.
4. Theriot, J. C., et al., Organocatalyzed atom transfer radical polymerization driven by visible light. *Science* **2016,** *352* (6289), 1082-6.

5. Ong, W.-J., et al., Graphitic Carbon Nitride (g-C3N4)-Based Photocatalysts for Artificial Photosynthesis and Environmental Remediation: Are We a Step Closer To Achieving Sustainability? *Chem. Rev.* **2016,** *116* (12), 7159-7329.

6. Concepcion, J. J., et al., Excited-State Quenching by Proton-Coupled Electron Transfer. *Journal of the American Chemical Society* **2007,** *129* (22), 6968-6969.

7. Weinberg, D. R., et al., Proton-Coupled Electron Transfer. *Chem. Rev.* **2012,** *112* (7), 4016-4093.

8. Lennox, J. C., et al., Excited-State Proton-Coupled Electron Transfer: Different Avenues for Promoting Proton/Electron Movement with Solar Photons. *ACS Ener. Lett.* **2017,** *2* (5), 1246-1256.

9. Damrauer, N. H., et al., Observation of Proton-Coupled Electron Transfer by Transient Absorption Spectroscopy in a Hydrogen-Bonded, Porphyrin Donor−Acceptor Assembly. *Journal of Physical Chemistry B* **2004,** *108* (20), 6315-6321.

10. Eisenhart, T. T.; Dempsey, J. L., Photo-induced Proton-Coupled Electron Transfer Reactions of Acridine Orange: Comprehensive Spectral and Kinetics Analysis. *J. Am. Chem. Soc.* **2014,** *136* (35), 12221-12224.

11. Liu, X., et al., Photocatalytic Water Splitting with the Acridine Chromophore: A Computational Study. *Journal of Physical Chemistry B* **2015,** *119* (33), 10664-72.

12. Reimers, J. R.; Cai, Z.-L., Hydrogen bonding and reactivity of water to azines in their S1 (n,pi*) electronic excited states in the gas phase and in solution. *Phys. Chem. Chem. Phys.* **2012,** *14* (25), 8791-8802.

13. Whitten, D. G.; Lee, Y. J., Photochemistry of aza aromatics. Identification of the reactive intermediate in the photoreduction of acridine. *J. Am. Chem. Soc.* **1971,** *93* (4), 961-966.

14. Peon, J., et al., Excited State Dynamics of Methyl Viologen. Ultrafast Photoreduction in Methanol and Fluorescence in Acetonitrile. *J. Phys. Chem. A* **2001,** *105* (24), 5768-5777.

15. Stermitz, F. R., et al., Photochemistry of n-heterocycles. V. Photochemistry of quinoline and some substituted quinoline derivatives. *J. Am. Chem. Soc.* **1970,** *92* (9), 2745-2752.

16. Arias-Rotondo, D. M.; McCusker, J. K., The photophysics of photoredox catalysis: a roadmap for catalyst design. *Chem. Soc. Rev.* **2016,** *45* (21), 5803-5820.

17. Corp, K. L.; Schlenker, C. W., Ultrafast Spectroscopy Reveals Electron-Transfer Cascade That Improves Hydrogen Evolution with Carbon Nitride Photocatalysts. *J. Am. Chem. Soc.* **2017,** *139* (23), 7904-7912.

18. Zhang, G., et al., Ionothermal Synthesis of Triazine–Heptazine-Based Copolymers with Apparent Quantum Yields of 60 % at 420 nm for Solar Hydrogen Production from "Sea Water". *Angew. Chem. Int. Ed.* **2018,** *57* (30), 9372-9376.

19. Wang, X., et al., A metal-free polymeric photocatalyst for hydrogen production from water under visible light. *Nat. Mater.* **2008,** *8,* 76.

20. Ullah, N., et al., Photoinduced Water–Heptazine Electron-Driven Proton Transfer: Perspective for Water Splitting with g-C3N4. *The Journal of Physical Chemistry Letters* **2019,** *10* (15), 4310-4316.

21. Domcke, W., et al., Solar Energy Harvesting with Carbon Nitrides and N-Heterocyclic Frameworks: Do We Understand the Mechanism? *Chem. Photo. Chem.* **2019,** *3* (1), 10-23.

22. Ehrmaier, J., et al., Mechanism of Photocatalytic Water Splitting with Graphitic Carbon Nitride: Photochemistry of the Heptazine–Water Complex. *J. Phys. Chem. A* **2017,** *121* (25), 4754-4764.

23. Rabe, E. J., et al., Proton-Coupled Electron Transfer from Water to a Model Heptazine-Based Molecular Photocatalyst. *J. Phys. Chem. Lett.* **2018,** *9* (21), 6257-6261.

24. Caspar, J. V.; Meyer, T. J., Photochemistry of tris(2,2'-bipyridine)ruthenium(2+) ion (Ru(bpy)32+). Solvent effects. *J. Am. Chem. Soc.* **1983,** *105* (17), 5583-5590.

25. McCusker, J. K., Electronic structure in the transition metal block and its implications for light harvesting. *Science* **2019,** *363* (6426), 484-488.

26. Turro, N. J., et al., *Principles of Molecular Photochemistry: An Introduction*. University Science Books Sausalito, California, 2009.

27. Ehrmaier, J., et al., Singlet-Triplet Inversion in Heptazine and in Polymeric Carbon Nitrides. *The journal of physical chemistry. A* **2019,** *123* (38), 8099-8108.

28. Barman, N., et al., Fluorescence Quenching of Hydrogen-Bonded Coumarin 102-Phenol Complex: Effect of Excited-State Hydrogen Bonding Strength. *The Journal of Physical Chemistry A* **2013,** *117* (19), 3945-3953.

29. Hossen, T.; Sahu, K., New Insights on Hydrogen-Bond-Induced Fluorescence Quenching Mechanism of C102–Phenol Complex via Proton Coupled Electron Transfer. *J. Phys. Chem. A* **2018,** *122* (9), 2394-2400.

30. Bronner, C.; Wenger, O. S., Proton-Coupled Electron Transfer between 4-Cyanophenol and Photoexcited Rhenium(I) Complexes with Different Protonatable Sites. *Inorganic chemistry* **2012,** *51* (15), 8275-8283.

31. Bronner, C.; Wenger, O. S., Kinetic Isotope Effects in Reductive Excited-State Quenching of Ru(2,2′-bipyrazine)32+ by Phenols. *J. Phys. Chem. Lett.* **2012,** *3* (1), 70-74.

32. Warren, J. J., et al., Thermochemistry of Proton-Coupled Electron Transfer Reagents and its Implications. *Chem. Rev.* **2010,** *110* (12), 6961-7001.

33. Dongare, P., et al., Analysis of Hydrogen-Bonding Effects on Excited-State Proton-Coupled Electron Transfer from a Series of Phenols to a Re(I) Polypyridyl Complex. *The Journal of Physical Chemistry C* **2017,** *121* (23), 12569-12576.

34. Petersson, J.; Hammarström, L., Ultrafast Electron Transfer Dynamics in a Series of Porphyrin/Viologen Complexes: Involvement of Electronically Excited Radical Pair Products. *The Journal of Physical Chemistry B* **2015,** *119* (24), 7531-7540.

35. Yamaji, M., et al., Verification of the electron/proton coupled mechanism for phenolic H-atom transfer using a triplet π,π∗ carbonyl. *Chem. Phys. Lett.* **2009,** *475* (4-6), 235-239.

36. Snellenburg, J. J., et al., Glotaran: A Java-Based Graphical User Interface for the R Package TIMP. *J. Stat. Softw.* **2012,** *49* (3), 1-22.

37. Schirmer, J., Beyond the random-phase approximation: A new approximation scheme for the polarization propagator. *Phys. Rev. A* **1982,** *26* (5), 2395-2416.

38. Bronner, C.; Wenger, O. S., Kinetic Isotope Effects in Reductive Excited-State Quenching of Ru(2,2′-bipyrazine)32+ by Phenols. *J. Phys. Chem. Lett.* **2012,** *3* (1), 70-74.

Chapter 5. Dynamics of H-atom Abstraction in Heptazine:Phenol Complexes Monitored with Ultrafast Pump-Push-Probe Spectroscopy

5.1 INTRODUCTION

Photochemical reactions occur on timescales of milliseconds to minutes. However, reaction yields are controlled by branching among photophysical pathways that occurs on much faster timescales (femtoseconds to nanoseconds). Unfortunately, it is not generally well-understood how these timescales are coupled. Competition among decay processes such as fluorescence, phosphorescence, internal conversion, intersystem crossing, charge transfer, surface hopping and H-atom tunneling ultimately determine the overall reaction efficiency. Understanding how to manipulate the branching ratios among these excited-state relaxation pathways is likely the key to directing reactivity in photochemical transformations such as CO_2 reduction,[1] water remediation,[2-3] acid/base photochemistry,[4-5] and artificial photosynthesis.[6]

Photochemical reaction mechanisms of aza-aromatics have been heavily debated in the literature for decades, yet little consensus has been reached concerning how intermolecular hydrogen bonding with H-atom donors can control the reactivity of these molecules.[7-9] Many aza-aromatics engage in addition, reduction, and substitution reactions when they absorb light in the presence of an appropriate H-atom donor.[10-14] Perhaps surprisingly, the mechanisms for these photochemical reactions remain poorly understood, despite an intense research effort beginning in the 1950s that continues to the present day.

Historically, the rich photochemistry of these *N*-heteroaromatics, such as acridines, purines, and quinolines in protic media was assumed to proceed directly from low-lying local molecular excited states of the heteroaromatic.[10, 14-15] By local molecular excited states, here we mean those involving only the orbitals of the chromophore, with no contribution from neighboring solvent molecules. Remarkably, until recently, even the electronic configuration of the reactive excited state of acridine, a model nitrogenous heteroaromatic whose photochemistry has been extensively studied for over 70 years,[15-20] continued to be a contentious issue in the literature. Some reports claim that any one of the individual $^1\pi\pi^*$, $^3\pi\pi^*$, $^1n\pi^*$, or $^3n\pi^*$ states is the reactive species, while others provide respective counter arguments rejecting them.[15-20]

In 2014, Eisenhart and Dempsey showed a proton-coupled electron transfer (PCET) mechanism by which the local triplet excited state drives H-atom transfer from phenol to acridine orange.[21] Using computational methods, Domcke demonstrated that this H-atom abstraction reaction with acridine involves a manifold of states comprising both aza-aromatic and hydroxylic orbitals of the H-bonded intermolecular complex.[22]

More recently, Domcke et al. predicted that heptazine-based materials and molecules engage in photochemistry analogous to that of acridine.[23-24] Heptazine-based materials, such as carbon nitride, have garnered intense interest for photocatalytic hydrogen evolution and water splitting in recent years.[3, 25-32] One factor driving research interest in graphitic carbon nitrides is that these materials can be prepared easily at scale with abundant, metal-free precursors, such as urea.[33-37] While the synthesis is straightforward, the chemical structures are ambiguous and therefore the underlying photophysical and photochemical processes of these catalysts are typically harrowing to control and remain poorly understood.

To clarify the fundamental photophysics of heptazine-based materials, we recently synthesized the anisole-substituted model heptazine derivative 2,5,8-tris(4-methoxyphenyl)-1,3,4,6,7,9,9b-heptaazaphenalene (TAHz), Figure 5-1a.[38] Using TAHz as a model system, we previously demonstrated that fluorescence from the excited-state hydrogen-bonded complex can be spectroscopically observed and that the complex photochemically reacts to liberate hydroxyl radicals, which can be scavenged by terephthalic acid to form luminescent 2-hydroxy-terephthalate.[38] Based upon the excited-state reduction potential of TAHz, the single electron water oxidation to hydroxyl radicals would not at first glance, appear to be a thermodynamically accessible process (+2.7 V vs SHE). However, *ab initio* computational results reveal that the coupling of proton and electron motion can provide a pathway to propel the system along the H-atom transfer coordinate.[39] Evidently, the H-bonding interaction modulates the energy of the reacting species via orbital mixing and fluctuation of the proton's position along the H-atom axis.

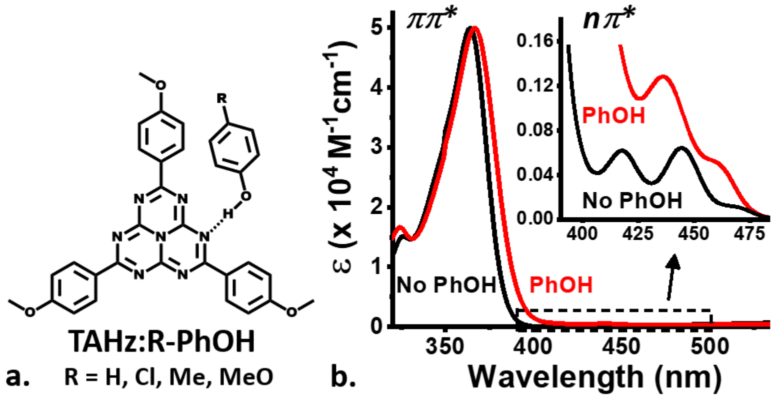

Figure 5-1. (a) Molecular structure and (b) ground state absorption spectrum of 2,5,8-tris(4-methoxyphenyl)-1,3,4,6,7,9,9b-heptaazaphenalene, TAHz, in toluene with and without PhOH (100 mM).

While photoinduced PCET of heptazine-based materials holds potential implications for future energy conversion and storage systems, the carbon nitride literature has focused almost exclusively on proton reduction reactions to form H_2.[25-28, 40-41] However, as stated above, there is limited knowledge of the underlying photochemical dynamics that control reactions such as H-atom abstraction.[24, 42-43] Therefore, it is compelling to examine how intermolecular excitations can serve as gateways to photochemical reactions, such as a single electron oxidation of hydroxylic compounds, to outline design rules for tuning the excited-state energetic landscape that controls this photochemical reactivity.

In this manuscript, we show the effect of transient intermolecular excitations on the excited-state branching ratio of TAHz in the presence of four phenol derivatives. We employ a series of substituted phenols, R-PhOH, to mimic the change in photochemistry, which would be analogous to that of installing electron withdrawing groups on the heptazine core. We chose this system based on two criteria, 1) the improved solubility of TAHz in toluene vs. water and 2) the ease with which we could tune the energy of the intermolecular charge transfer (CT) state by varying the electron donating/withdrawing character on the proton source (i.e., R-PhOH). Using ultrafast pump-push-probe spectroscopy, we show that the relative decrease of the induced absorption (ΔΔOD) from the hydrogen-bonded complex upon the arrival of the push pulse exhibits an anticorrelation with the photochemical reactivity of TAHz:R-PhOH. That is, the effect of the push pulse decreases as the driving force for electron transfer increases. These results indicate that the coupled ultrafast motion of electrons and protons may control the fundamental photochemical reactivity of heptazine-based materials.

5.2 RESULTS AND DISCUSSION

Previously, for the TAHz:R-PhOH system we explored trends in the kinetic isotope effect, ground state association constants, and barrier heights to the CT state and the roles of these characteristics in fluorescence quenching of the complex.[39] While that study was extremely informative for assessing the reactivity of the lowest energy hydrogen-bonded excited state, it provided no handle for studying the upper excited-state dynamics that may strongly influence the branching among photochemical reaction pathways. As a result, it remains unclear what role the upper excited states may play in propelling the photoexcited complex along the reactive CT state trajectories.[44] Herein we perform ultrafast spectroscopic characterization of TAHz in the presence and absence of four R-PhOH derivatives and correlate the response to an additional "push" pulse and the reactivity of these hydrogen-bonded complexes.

Figure 5-1a shows the structure of TAHz hydrogen-bonded to R-PhOH. The absorption spectrum of TAHz in toluene exhibits a redshift in the ππ* absorption as well as a blueshift in the nπ* transitions in the presence of PhOH, shown in Figure 5-1b. This shift results from the ground-state hydrogen-bonding interaction between the peripheral nitrogens on TAHz and the hydrogen of the hydroxyl moiety on PhOH, denoted by a dotted line in Figure 5-1a.

The approximate oxidation potentials of the R-PhOH used in this study are shown in Figure 5-2a.[45-48] Increasing the strength of the electron donating substitution on R-PhOH shifts the oxidation potential cathodically, which stabilizes the reactive CT curve relative to the unreactive mixed nπ* excited-state hydrogen-bonded TAHz complex, denoted as EA_{dark*} in Figure 5-2a. Figure 5-2b schematically depicts potential energies of the hydrogen-bonded TAHz:R-PhOH complex as a function of H-atom distance. This cartoon potential energy diagram reflects the barrier to the CT state, which decreases with the increasing electron donating strength of the substituent on phenol.[39] Previous computational results show that the reaction actually becomes barrierless for the case of MeO-PhOH to proceed to the CT state,[39] suggesting more significant formation of biradicals with the initial excitation.

Verification of increased formation of biradical in the case of TAHz:MeO-PhOH, following the barrier height calculations, can be seen in Figure 5-3. Here electron paramagnetic resonance (EPR) spectroscopy shows a larger population of phenoxyl radicals with stronger electron-donating substituents, R, on PhOH upon 365 nm illumination. This confirmation of increased radical generation suggests changing the excited-state energy landscape does in fact have a large effect on the branching ratios post-excitation and therefore the reaction yield. However, this is only an indirect measure of the energy and interconversion of upper excited states. Figure C-1 shows EPR spectra taken in this work match literature precedent.[49]

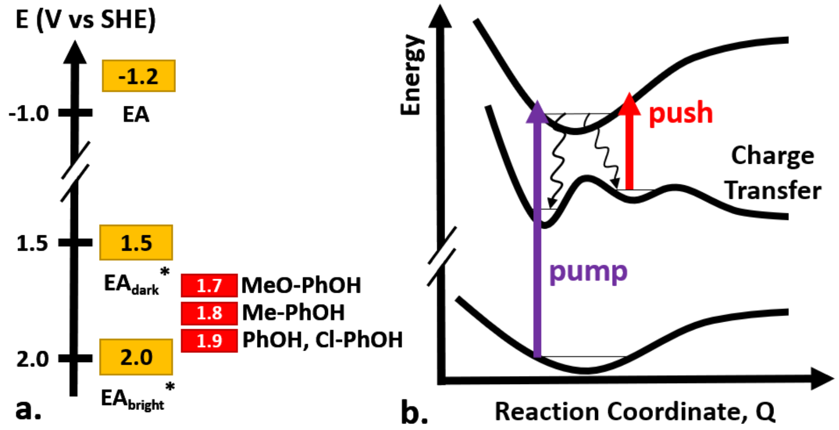

Figure 5-2. (a) Approximate energy landscape of TAHz and four phenol derivatives.
As the phenol oxidation potential shifts cathodically, the thermodynamics for charge transfer after a heptazine-localized excitation become more favorable. (b) Cartoon potential energy diagram with a possible photochemical charge transfer. The push pulse populates high lying excited states which can result in partial relaxation to the charge transfer state.

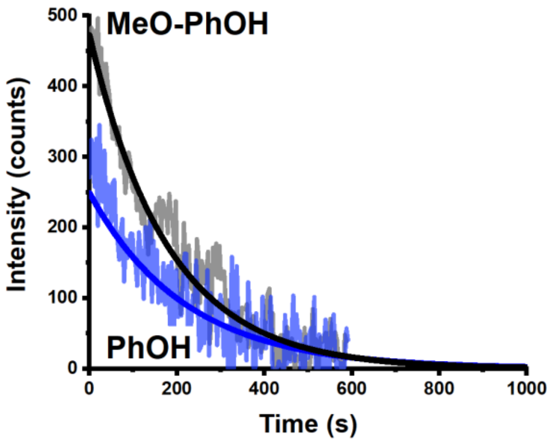

Figure 5-3. Decay of EPR signal from phenoxyl radical/DMPO adduct after excitation with 365 nm light with TAHz in air-free toluene. TAHz:MeO-PhOH shows nearly double the intensity value, proportional to concentration, at time zero compared to TAHz:PhOH indicating stronger electron-donating substituents on phenol increase the photochemical reactivity.

We use transient absorption spectroscopy to probe the upper excited-state manifold. Figure 5-4a shows the transient absorption spectrum for TAHz in toluene from 400-1400 nm. The majority of the signal is an induced absorption spanning almost all available probe wavelengths.

To identify the nature of the broad induced absorption, seen in Figure 5-4a, we focus on the NIR portion of the transient absorption spectrum. We compare the lifetime of the luminescence from S_1 and the lifetime of the excited-state absorption in neat toluene (without the presence of an H-atom donor) in Figure C-2. We see virtually indistinguishable decay kinetics for the photoluminescence and NIR induced absorption for TAHz in neat toluene with a monoexponential lifetime of about 300 ns. Based on these results, we associate the induced absorption signal in Figure 5-4 with the lowest lying singlet excited state, S_1.

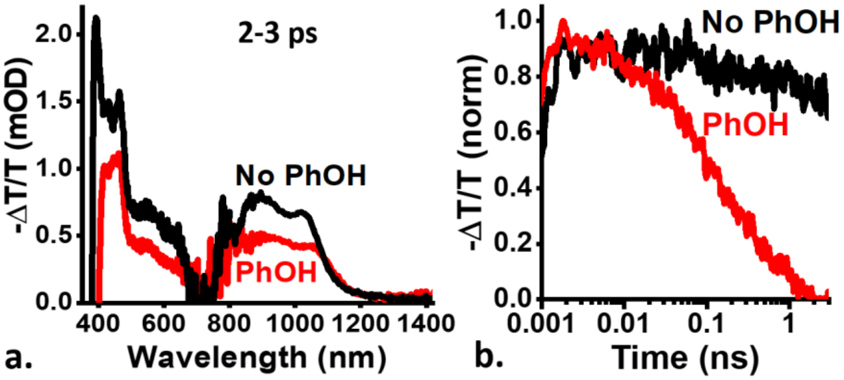

Figure 5-4. (a) Transient absorption spectra from the ultraviolet to near infrared (averaged from 2 – 3 ps) and (b) decay traces of TAHz (15 μM) with and without phenol (1.0 M) averaged over 900 – 1000 nm.

Figure 5-4 also shows static (a) and dynamic (b) quenching of the excited-state absorption of TAHz in the presence of PhOH. This dynamic quenching is likely due to a new relaxation pathway, which leads to •TAHzH/PhO• biradicals as we have seen previously in luminescence quenching.[39] In addition to quenching, the excited state absorption changes shape slightly. Notable changes include the redshift of the bleach in the UV, which is expected from the ground state absorption shift seen in Figure 5-1, and the slight redshift at low energies, more clearly seen in Figure C-3. This shift is due to hydrogen-bonded TAHz as opposed to free TAHz molecules in solution.

In the presence of PhOH, the decay of the induced absorption contains a noticeable sub-nanosecond component, as well as a longer-lived component (Figure 5-4). We use global analysis to kinetically resolve these features and recover the evolution associated difference spectra, EADS, shown in Figure 5-5. Using global analysis, we take the overall spectrum, $\psi(t,\lambda)$, to be a linear combination of a time-dependent concentrations, $c_i(t)$, of the associated species with a wavelength-dependent spectrum, $\sigma_i(\lambda)$, for the i^{th} species, such that $\psi(t,\lambda) = \sum c_i(t)\sigma_i(\lambda)$. Figure 5-5 shows (a) the EADS of the NIR transient absorption spectrum (850 nm – 1400 nm) and (b) their decay traces in the presence of PhOH (1.0 M). We recover two distinct EADS, one with a decay constant of roughly 620 ps and the second with a decay constant of roughly 75 ps. The spectrum at early times is redshifted compared to the longer-lived evolution associated spectrum. Figure C-4 shows the luminescence of TAHz in a similar H-bonded environment which has almost identical evolution associated decay constants.

We regard the hydrogen-bonded state as a relaxation pathway from S_n that can serve as a gateway to the reactive CT state and •TAHzH/PhO• biradical state, seen in Figure 5-2. As stated above, the barrier height to reach the CT state is predicted to be lowered by either increasing the electron donating character of the H-atom donor or by increasing the electron withdrawing character of the substituents on the heptazine core.[39] This study focuses on changing the electron donating character of the H-atom donor, R-PhOH.

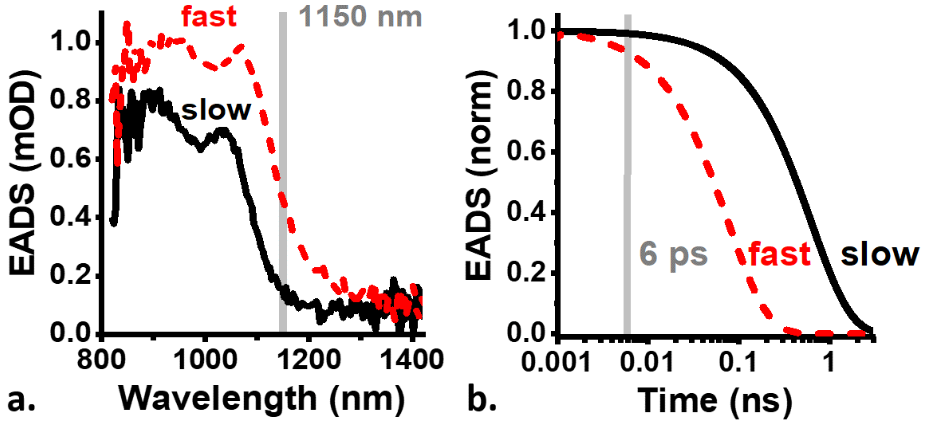

Figure 5-5. Global analysis (a) spectra and (b) kinetics of the NIR transient absorption feature of TAHz (15 µM) in the presence of PhOH (1.0 M).
From the evolution associated difference spectra (EADS), the push pulse was chosen to be 1150 nm to preferentially excite the short-lived hydrogen-bonded state (75 ps decay constant). The long-lived hydrogen-bonded state has a decay constant of 620 ps.

Additionally, we hypothesize that the upper excited states, S_n, (populated upon 365 nm excitation) may provide a pathway to the reactive CT state and, by extension, the H-atom transfer reaction leading to radical generation. Unfortunately, these high lying excited states are extremely short lived (<200 fs), see Figure C-5, implying the biradical product yield will be intrinsically low if this were the only excited-state PCET reactivity pathway.

To reveal the influence of the excited-state curve crossing on photochemical H-atom abstraction reactions between TAHz and phenol derivatives, we employ a multi-pulse ultrafast transient absorption technique, wherein we introduce a NIR laser pulse, denoted “push,” which temporally follows the pump pulse. A simplified experimental setup and pulse sequence of this technique are found in Figure 5-6 and Figure C-6, respectively. We use this pump-push-probe spectroscopic technique to glean additional information about higher-lying excited states and charge separated species that may result in photochemical products. Pump-push-probe spectroscopy has recently been utilized by a number of authors to monitor charge separation dynamics in organic materials often used in solar cells.[50-57] Such results have demonstrated that photocurrent generation efficiency is governed by access to delocalized intermolecular charge separated states. In the case of thin-film heterojunction organic solar cells, the role of the push pulse is to impart additional energy to overcome the activation barrier for accessing the delocalized charge separated states.

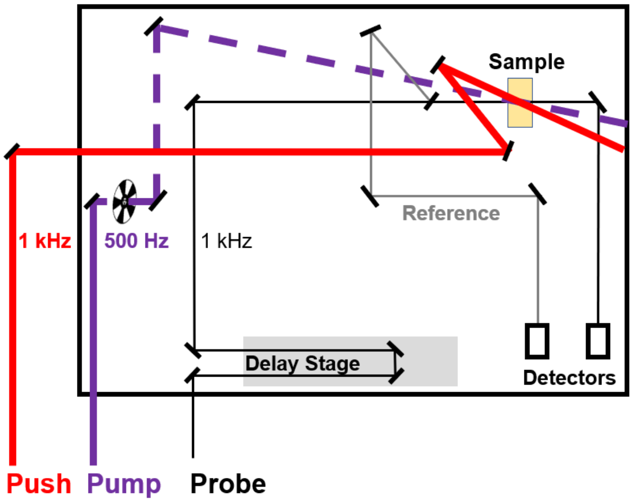

Figure 5-6. Schematic of pump-push-probe spectroscopy.
The pump pulse (500 Hz) is first incident on the sample, followed by the push pulse (1 kHz) ~6 ps later. The probe pulse (1 kHz) is on an adjustable delay stage (-1.0 to 12 ps for these experiments).

In the context of photochemical reactivity, pump-push-probe spectroscopy allows us to infer information concerning the role of the mixed nπ* excitations of the H-bonded complex in propelling the system toward the reactive CT state. In some cases, following the initial pump pulse (365 nm), the excited states can be further excited by the energy of the push pulse (1150 nm). The photon energy of the push pulse was chosen, based upon the EADS in Figure 5-5, to impart a nearly-resonant perturbation to the H-bonded excited state complex at 6 ps.

Using a third laser pulse (broadband probe), we are able to monitor the sample’s dynamic response to the pump and push pulse by recording time-dependent changes in transmission. Figure

5-7a shows the transient absorption spectra with and without the push pulse (both averaged from 6.5 – 8.0 ps) for TAHz in the presence of PhOH. The spectral evolution following the push pulse reveals a decrease (bleach) in the excited state signal amplitude.

Interestingly, the bleach seen in Figure 5-7a is persistent in the presence of PhOH. Figure 5-7b and Figure 5-7c show the transient absorption signal probed from 700 – 750 nm and 900 – 1000 nm, respectively. The signal bleaches and never exhibits a complete recovery on the timescale of our experiment. This persistent bleaching suggests that, following the push arrival, the system is propelled into a higher-lying excited state, which, upon coupling to the CT electronic manifold, can relax along the H-atom reactivity coordinate toward the •TAHzH/PhO• biradical state.

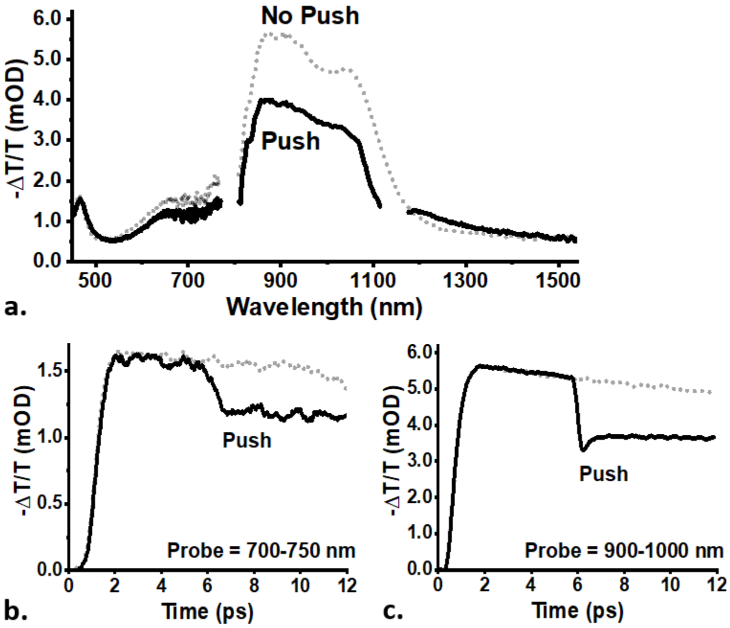

Figure 5-7. (a) Transient absorption spectra of TAHz (50 μM) in toluene and PhOH (1.0 M) with the push pulse (solid lines) and without the push pulse (dotted lines) averaged from 6.5 – 8.0 ps. Temporal traces averaged over (b) 700 – 750 nm and (c) 900 – 1000 nm. The system was pumped at 365 nm and pushed at 1150 nm. The sample was stirring throughout the experiment.

To verify that the system responds linearly to the arrival of the push, we performed a push pulse power dependence study, the results of which are shown in Figure C-7. The effect of the push pulse is indeed linear with increasing power over the range used in this work. Therefore, the push pulse does not itself appear to be driving any two-photon processes under NIR excitation.

Figure 5-8a shows the transient absorption spectrum of TAHz in neat toluene overlaid with the spectra of TAHz in the presence of PhOH, Cl-PhOH, Me-PhOH and MeO-PhOH with and without the push pulse (averaged from 6.5 – 8.0 ps). We observe static quenching of the TA signal with the addition of each R-PhOH derivatives. The magnitude of this quenching increases with the electron donating character of the substituent on R-PhOH. After the push pulse, many of the spectra exhibit a decrease (bleach) in the signal amplitude, as demonstrated in Figure 5-7a. The change in spectral shape is least significant, almost non-existent, for TAHz:MeO-PhOH, suggesting that the excited-state population is not significantly altered by the push pulse in this case. This could be due to the high reactivity of the TAHz:MeO-PhOH complex, producing radicals readily without the assistance of the additional energy provided by the push pulse. The spectra in Figure 5-8a are overlaid in Figure C-8 for closer comparison.

Figure 5-8b shows how the push pulse influences the dynamics in the 700 – 750 nm region of the TA spectrum on the picosecond timescale for the series of TAHz:R-PhOH complexes, in contrast to the excited-state push response of TAHz in neat toluene. Similar to Figure 5-7c, Figure 5-8b demonstrates the persistent bleaching of the hydrogen-bonded excited state in the presence of R-PhOH, thus, we observe virtually no recovery of the induced absorption after the push pulse which suggests additional reactivity toward the •TAHzH/R-PhO• biradical state.

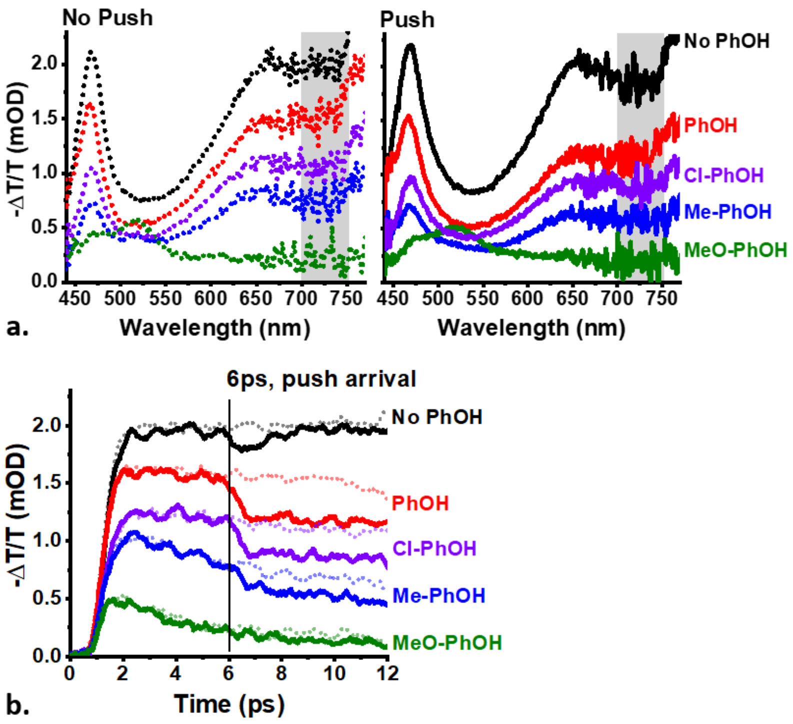

Figure 5-8. Pump-push-probe spectra and kinetics of TAHz with and without phenol.
(a) Pump-push-probe spectra of TAHz (50 μM) in toluene with and without R-PhOH, with (solid) and without (dotted) the push pulse, averaged from 6.5 – 8.0 ps. (b) Decay of the population probed from 700 – 750 nm, shaded in grey in (a), with (solid) and without (dotted) the push pulse. The system was pumped at 365 nm and pushed at 1150 nm at 6 ps.

The response we observe in Figure 5-8c for TAHz in neat toluene contrasts significantly with the results we observe for the TAHz:R-PhOH complexes. When PhOH is present, there is an irrecoverable loss of the transient absorption signal after the arrival of the push pulse. The PhOH exhibits the largest signal loss (~25%) and MeO-PhOH shows the smallest push-induced signal bleaching (<5%). However, without R-PhOH present (i.e., the “No PhOH” case), a small fraction of the S_1 population is pushed to a higher-lying state, which induces a transient bleaching of the absorption intensity in the 700 – 750 nm region. Yet this TA signal rapidly recovers, roughly within the duration of our push pulse (< 200 fs), and the signal magnitude after 8 ps with the push pulse is virtually indistinguishable from that without the push pulse.

Further investigation shows the dynamic response to the push pulse in the 500 – 550 nm spectral regions with and without R-PhOH, Figure C-9. In this region, we observe an increase in the amplitude of the induced absorption signal, which we associate with an upper excited state absorption, since it rapidly decays within the duration of the push pulse, consistent with internal conversion of the free TAHz chromophore. This data supports our hypothesis that the push pulse excites the hydrogen bonded complex into an upper excited state and, depending on the presence and type of phenol, a fraction of the excitations relaxes into the CT state and, subsequently, yield radical products. In the case of MeO-PhOH, the push pulse does not significantly influence the amplitude of the TA signal. This result suggests that in the case of MeO-PhOH the initial excitation already proceeds along a trajectory toward radical products without the additional energy imparted by the push pulse. These results appear to be consistent with prior predictions of barrierless excited state reactivity in the TAHz:MeO-PhOH complex.[39]

5.3 COMPUTATIONAL DISCUSSION

To assess the role of the push pulse in controlling the photochemical reactivity of hydrogen-bonded TAHz:R-PhOH complexes, we turned to ab initio quantum chemical calculations. The vertical transition energy (ΔE, eV) and oscillator strength (f) from the ground state (S_0) and from the lowest excited state (S_1) were determined with the second-order algebraic-diagrammatic-construction (ADC(2)) method,[58] shown in Table 5-1 and Table 5-2, respectively. ADC(2) is a wave-function based single-reference propagator method which provides, in contrast to time-dependent density functional theory (TD-DFT) with various functionals, an accurate and balanced description of locally excited states and CT states, which is essential for the determination of reliable vertical excitation energies for excited state PCET reactions.

Table 5-1 shows the calculated excitation spectrum of TAHz:R-PhOH from the S$_0$ state. The intermolecular ππ* CT state (from R-PhOH to TAHz) is marked in blue and the three intramolecular ππ* CT states (from anisole, A, to Hz) are marked in red. While the intermolecular CT state is dark, the intramolecular CT states are very bright. The lowest two intramolecular CT states have the highest oscillator strengths and are the absorbing states seen experimentally.

Table 5-1. Transition energy (ΔE/eV) and oscillator strength (f) from the ground state (S$_0$), and dipole moment (μ/Debye) of TAHz with R-PhOH, computed with the ADC(2)/cc-pVDZ method at the ground-state MP2/cc-pVDZ equilibrium geometry.
The intermolecular ππ* CT state (from R-PhOH to Hz) is marked in blue. The intramolecular ππ* CT states (from anisole, A, to TAHz) are marked in red.

State	R											
	Cl			H			CH$_3$			OCH$_3$		
	ΔE	f	μ	ΔE	f	μ	ΔE	f	μ	ΔE	f	μ
1ππ* LE Hz	2.65	0.004	5.19	2.65	0.003	3.27	2.64	0.003	2.99	2.64	0.003	2.12
1ππ* A → Hz	3.45	1.112	4.83	3.45	1.170	5.00	3.46	1.049	5.82	3.46	1.113	6.26
1ππ* A → Hz	3.60	0.802	3.01	3.62	0.793	1.43	3.62	0.791	1.46	3.62	0.792	2.58
1ππ* CT	3.64	0.000	10.1	3.63	0.000	13.9	3.43	0.065	20.5	3.09	0.001	24.3
1ππ* A → Hz	4.11	0.567	11.5	4.12	0.578	8.87	4.12	0.580	7.83	4.13	0.552	7.31

The energy and transition moment of the three lowest lying excited states do not significantly depend on R-PhOH. However, the intermolecular CT state is moderately stabilized by Me-PhOH and drastically stabilized by MeO-PhOH and as a result the intermolecular CT state is vertically below the absorbing state. This indicates spontaneous (ultrafast) electron transfer after the pump pulse (365 nm) and thus the push pulse is not necessary to reach the intermolecular CT state. These computations are consistent with the results of the pump push probe experiment shown in Figure 5-8c and previous results.[39]

Table 5-2 shows the calculated excitation spectrum of TAHz:R-PhOH from the lowest lying excites state (S_1) to model the experimental excitation by the push pulse after relaxation from S_n. The two lowest excited states when exciting from S_1 are the intramolecular $n\pi^*$ and $\pi\pi^*$ CT states. This energy is independent of R-PhOH and is commensurate with the observed broad induced absorption near 1100 nm, Figure 5-4a. Interestingly, just above the intramolecular CT states there is an intermolecular CT state with nonzero oscillator strength. In the case of PhOH, Cl-PhOH, and Me-PhOH we experimentally saw a persistent decrease in the S_1 population after exciting with the push pulse, suggesting the push was exciting to the intermolecular CT state, Figure 5-8c. These calculations show that this direct excitation from S_1 to the intermolecular CT state is, in fact, possible at similar energies to the experiment.

Table 5-2. Transition energy (ΔE^*/eV) and oscillator strength (f^*) from the first singlet excited state (S_1), and dipole moment (μ/Debye) of TAHz with R-PhOH computed with the ADC(2)/cc-pVDZ method at the first singlet excited-state ADC(2)/cc-pVDZ equilibrium geometry.
The intermolecular $\pi\pi^*$ CT state (from R-PhOH to TAHz) is marked in blue. The intramolecular $n\pi^*$ and $\pi\pi^*$ CT states (from anisole, A, to Hz) are marked in red.

State	R											
	Cl			H			CH_3			OCH_3		
	ΔE*	f*	μ	ΔE*	f*	μ	ΔE*	f*	μ	ΔE*	f*	μ
$1n\pi^*$ $n \rightarrow Hz$	1.08	0.003	4.41	1.08	0.001	3.28	1.12	0.001	2.63	1.09	0.004	1.93
$1\pi\pi^*$ $A \rightarrow Hz$	1.09	0.004	3.34	1.10	0.007	4.74	1.09	0.005	1.56	1.11	0.003	3.09
$1\pi\pi^*$ $A \rightarrow Hz$	1.25	0.015	4.58	1.26	0.013	2.18	1.26	0.012	1.89	1.26	0.012	2.38
$1\pi\pi^*$ CT	1.27	0.007	15.6	1.26	0.006	11.86	1.00	0.007	19.06	0.67	0.009	24.6
$1\pi\pi^*$ $A \rightarrow Hz$	1.81	0.010	12.2	1.83	0.018	10.09	1.83	0.021	9.67	1.82	0.037	6.54

5.4 CONCLUSIONS

Aza-aromatic photochemistry has been studied extensively since the mid 1900's, however, the underlying processes of coupled proton and electron motion, specifically in heptazine-based systems, is not well understood. Here we examine the coupled proton and electron motion in the TAHz:R-PhOH complex and the correlation between ultrafast intermolecular charge transfer and the photochemical reactivity resulting in phenoxyl radicals. This connection between femtosecond – nanosecond dynamics and millisecond – minute chemical reactions has the potential to provide insight into materials design rules to manipulate photoinduced PCET reactions.

We demonstrated that altering the excited-state landscape of the proton and electron donor can dramatically change the photochemical branching ratios after the initial excitation. Our data suggest that the fraction of excitations that underwent photoinduced PCET upon the initial 365 nm pulse was correlated with the increasing electron donating strength of the substituent, R, on R-PhOH. In the presence of TAHz:MeO-PhOH the push pulse caused little to no change in the excited state dynamics. These results suggest the trajectory of these photochemical reactions is likely decided at a rate that approaches the sub-ps timescale.

Our time-resolved multi-pulse spectroscopy results provide synthetic chemists and materials scientists with new insight into photoreaction pathways that are germane to engineering new materials for solar fuel generation. Experimental efforts are underway in our lab to shift the heptazine-localized excited state closer to the oxidation potential of water to favor photoinduced PCET without the need of additional energy from push pulses. We are installing electron withdrawing groups onto the heptazine core, which should mimic the effect from strong electron donating substituents on phenol. We hypothesize this installation will shift the lowest lying hydrogen-bonded state closer to the CT state, possibly creating a barrier-less transition, which would increase the efficiency of the photo-initiated one electron oxidation of water.

5.5 EXPERIMENTAL METHODS

Reagents. Urea, potassium hydroxide, phosphorous oxychloride, phosphorous pentachloride, toluene, and phenol were purchased from Sigma Aldrich. Anisole (99%), methylphenol, and methoxyphenol were purchased from Alfa Aesar. Aluminum chloride was purchased from Fischer Scientific. All reagents were used without further purification, except toluene was dried with molecular sieves.

Synthesis. *Graphitic carbon nitride:* Briefly, urea (10 g) was heated in a porcelain crucible (20 mL) using a potter's kiln at 500 °C for 3 h, with a ramp rate of 30 °C per hour under ambient atmosphere. The light-yellow product was ground thoroughly with a mortar and pestle.

Potassium cyamelurate: 4.5 g of graphitic carbon nitride was refluxed in KOH (3.0 M, 150 mL) for 6 h. The solution was hot filtered over a glass frit and then cooled for recrystallization. The resulting white crystals were filtered and washed with cold ethanol.

Cyameluric chloride: Phosphorous oxychloride (35 mL) was added to a flame-dried round-bottom flask with a stir bar. Phosphorous pentachloride (4.6 g) was added and allowed to stir for 5 minutes. Potassium cyamelurate (2.0 g) was added and the suspension was refluxed under N_2 at 110°C for 6 hrs. $POCl_3$ was removed under reduced pressure using a distillation set-up in the fume hood. The remaining solution was put on ice and ice water (50 mL) was added dropwise while stirring. The product was vacuum filtered and washed with ice-cold water. The resulting product was dried under vacuum for a few hours and stored in a desiccator. Safety note: $POCl_3$ and PCl_5 react with water exothermically to produce HCl gas and H_3PO_4. Always keep these reagents in a ventilated chemical fume hood and quench slowly with sodium bicarbonate.

2,5,8-tris(4-methoxyphenyl)-1,3,4,6,7,9,9b-heptaazaphenalene (TAHz): Anisole (10 mL) was purged with nitrogen. Aluminum chloride (4.0 g) was added to the flask and allowed to stir for a few minutes at 60°C. Cyameluric chloride (1.0 g) was added slowly over 30 minutes. The reaction mixture was stirred at 60°C under nitrogen for 5 hours. Deionized water (25 mL) was added and the solution was stirred until the color changed to yellow and the large chunks dissolved. The resulting bright yellow powder was filtered and washed with water. The product was purified by slowly recrystallizing in hot DMSO (3 mg/mL). Characterization of TAHz is shown in our previous manuscript.[38]

Time-Resolved Photoluminescence Spectra. Time-resolved photoluminescence spectra were collected using a Hamamatsu streak camera (C10910) with a slow-sweep unit (M10913-01) in photon counting mode. Samples were irradiated with 50 fs pulses at 365 nm and 1 kHz pump from a Coherent/Light Conversion OPerA solo optical parametric amplifier (OPA). Pump fluences were ~1 x 10^{13} photons/cm^3.

Laser Beam Characterization. The pump beam profile was characterized at the sample position using the BC106N-VIS CCD Camera Beam Profiler purchased from Thorlabs. Spatial beam images and spot size calculations were obtained from Thorlabs' standard beam profiler software package. Average power was measured using the Coherent FieldMate laser power meter equipped with the OP-2 VIS high sensitivity sensor purchased from Edmond Optics.

Transient Absorption Spectroscopy. Samples were irradiated with the 365 nm (~3 x 10^{14} photons/cm^3/pulse) output of a Coherent, Inc./Light Conversion OPerA Solo OPA that was pumped with 50 fs pulses from a 1 kHz Ti:sapphire amplifier (Libra-HE, Coherent, Inc.). Supercontinuum probe pulses (∼200 fs) were generated by focusing a fraction of the 800 nm amplifier output onto CaF_2 or sapphire plates. The probe beam was temporally delayed from the pump using a mechanical delay line (Ultrafast Systems). Spectra were collected with a CMOS sensor and InGaAs fiber-coupled multichannel photodiode array spectrometer and plotted as the differential optical density, $\Delta OD(\lambda, t) = Pump_{on}(\lambda,t) - Pump_{off}(\lambda,t)$. A reference line was monitored to account for fluctuations in the probe beam. Spectra were measured in a 2 mm path length quartz cuvette with continuous stirring.

Global analysis. To deconvolute time-resolved spectra, global analysis was performed using Glotaran, a graphical user interface for the R-package TIMP.[59] The analysis performed here contained two spectral components, according to the singular value decomposition, each with their respective decay constants. No parameters were constrained.

Pump-Push-Probe Spectroscopy. Samples were pumped with the 365 nm (500 Hz) output of a Coherent, Inc./Light Conversion OPerA Solo OPA, and then pushed with the 1150 nm (1000 Hz) output of a Coherent, Inc./Light Conversion Topas OPA. The delay of the push was fixed 6 ps after the pump pulse. At various delays after the pump, the sample was probed (1000 Hz) with a white light continuum and the difference signal was collected and plotted as the differential optical density, $\Delta OD(\lambda, t) = Pump_{on}Push_{on}(\lambda,t) - Pump_{off}Push_{on}(\lambda,t)$.

Electron Paramagnetic Resonance Spectroscopy. Samples were prepared in an argon glovebox. Air-free toluene was used to prepare stock solutions of TAHz, DMPO, and phenols. Sample solutions (100 uM TAHz, 50 mM DMPO and 45 mM phenols) were prepared from the stock solutions just prior to the measurements. Electron paramagnetic resonance spectra were collected on a Bruker EMXnano X-band spectrometer with a 100 kHz magnetic field modulation and a 9.64 GHz microwave source equipped with Bruker Xenon software for data acquisition. Samples were under irradiation with 365 nm LED’s for 15 minutes prior to data acquisition.

5.6 REFERENCES

1. Wang, S.; Wang, X., Imidazolium Ionic Liquids, Imidazolylidene Heterocyclic Carbenes, and Zeolitic Imidazolate Frameworks for CO2 Capture and Photochemical Reduction. *Angew. Chem. Int. Ed.* **2016,** *55* (7), 2308-2320.
2. Kumar, S., et al., Two-dimensional carbon-based nanocomposites for photocatalytic energy generation and environmental remediation applications. *Beilstein J. Nanotech.* **2017,** *8*, 1571-1600.
3. Ong, W.-J., et al., Graphitic Carbon Nitride (g-C3N4)-Based Photocatalysts for Artificial Photosynthesis and Environmental Remediation: Are We a Step Closer To Achieving Sustainability? *Chem. Rev.* **2016,** *116* (12), 7159-7329.
4. Roy, S., et al., 5-Methoxyquinoline Photobasicity Is Mediated by Water Oxidation. *J. Phys. Chem. A* **2019,** *123* (31), 6645-6651.
5. Hunt, J. R.; Dawlaty, J. M., Photodriven Deprotonation of Alcohols by a Quinoline Photobase. *The Journal of Physical Chemistry A* **2018,** *122* (40), 7931-7940.
6. Wasielewski, M. R., Photoinduced electron transfer in supramolecular systems for artificial photosynthesis. *Chem. Rev.* **1992,** *92* (3), 435-461.
7. Herkstroeter, W. G.; Hammond, G. S., Mechanisms of Photochemical Reactions in Solution. XXXIX.1 Study of Energy Transfer by Kinetic Spectrophotometry. *J. Am. Chem. Soc.* **1966,** *88* (21), 4769-4777.
8. Weinberg, D. R., et al., Proton-Coupled Electron Transfer. *Chem. Rev.* **2012,** *112* (7), 4016-4093.
9. Gagliardi, C. J., et al., Integrating proton coupled electron transfer (PCET) and excited states. *Coord. Chem. Rev.* **2010,** *254* (21), 2459-2471.

10. Stermitz, F. R., et al., Photochemistry of n-heterocycles. V. Photochemistry of quinoline and some substituted quinoline derivatives. *J. Am. Chem. Soc.* **1970,** *92* (9), 2745-2752.

11. Stermitz, F. R.; Wei, C. C., Photochemistry of aromatic N-heterocycles. IV. McLafferty rearrangement and type II photocleavage comparisons in a new system. 2-Substituted quinolines. *J. Am. Chem. Soc.* **1969,** *91* (11), 3103-3104.

12. Chapman, O. L.; Editor, *Organic Photochemistry, Vol. 2*. Dekker: 1969; p 230 pp.

13. Connolly, J. S.; Linschitz, H., Photoaddition of alcohols to purine. *Photochem. Photobiol.* **1968,** *7* (6), 791-806.

14. Whitten, D. G.; Lee, Y. J., Reactions of Hidden n, π* Excited States in N-Heteroaromatics. Photoreduction and Photoaddition. *J. Am. Chem. Soc.* **1970,** *92* (2), 415-416.

15. Whitten, D. G.; Lee, Y. J., Photochemistry of aza aromatics. Identification of the reactive intermediate in the photoreduction of acridine. *J. Am. Chem. Soc.* **1971,** *93* (4), 961-966.

16. Kellmann, A.; Dubois, J. T., Photoreactive State of Acridine in Solution. *J. Chem. Phys.* **1965,** *42* (7), 2518-2522.

17. Kikuchi, K., et al., Reaction and deactivation of excited acridine in ethanol. *J. Phys. Chem.* **1985,** *89* (5), 868-871.

18. Donckt, E. V.; Porter, G., Role of the 3(n—π*) State in the Photoreduction of Acridine. *J. Chem. Phys.* **1967,** *46* (3), 1173-1175.

19. Wilkinson, F.; Dubois, J. T., Reactive State in the Photoreduction of Acridine in Ethanol. *J. Chem. Phys.* **1968,** *48* (6), 2651-2654.

20. Koizumi, M., et al., Reactive State of Acridine in the Photoreduction in Alcohols. *J. Chem. Phys.* **1968,** *48* (4), 1869-1870.

21. Eisenhart, T. T.; Dempsey, J. L., Photo-induced Proton-Coupled Electron Transfer Reactions of Acridine Orange: Comprehensive Spectral and Kinetics Analysis. *J. Am. Chem. Soc.* **2014,** *136* (35), 12221-12224.

22. Liu, X., et al., Photocatalytic Water Splitting with the Acridine Chromophore: A Computational Study. *J. Phys. Chem. B* **2015,** *119* (33), 10664-10672.

23. Ehrmaier, J., et al., Mechanism of Photocatalytic Water Splitting with Graphitic Carbon Nitride: Photochemistry of the Heptazine-Water Complex. *J. Phys. Chem. A* **2017,** *121* (25), 4754-4764.

24. Ehrmaier, J., et al., Mechanism of photocatalytic water splitting with triazine-based carbon nitrides: insights from ab initio calculations for the triazine-water complex. *Phys. Chem. Chem. Phys.* **2018,** *20* (21), 14420-14430.

25. Liu, J., et al., Water splitting. Metal-free efficient photocatalyst for stable visible water splitting via a two-electron pathway. *Science* **2015,** *347* (6225), 970-4.

26. Moniz, S. J. A., et al., Visible-light driven heterojunction photocatalysts for water splitting - a critical review. *Energy Environ. Sci.* **2015,** *8* (3), 731-759.

27. Rahman, M. Z., et al., Carbon, nitrogen and phosphorus containing metal-free photocatalysts for hydrogen production: progress and challenges. *J. Mater. Chem. A* **2018,** *6* (4), 1305-1322.

28. Wen, J. Q., et al., A review on g-C3N4-based photocatalysts. *Appl. Surf. Sci.* **2017,** *391*, 72-123.

29. Ye, S., et al., A review on g-C3N4 for photocatalytic water splitting and CO2 reduction. *Appl. Surf. Sci.* **2015,** *358*, 15-27.

30. Zhu, B., et al., First-principle calculation study of tri- s -triazine-based g-C 3 N 4 : A review. *Appl. Catal. B* **2018,** *224*, 983-999.

31. Liu, X.; Dai, L., Carbon-based metal-free catalysts. *Nat. Rev. Mater.* **2016,** *1*, 16064.

32. Xinchen, W., et al., A metal-free polymeric photocatalyst for hydrogen production from water under visible light. *Nat. Mater.* **2009,** *8*, 76-80.

33. Liu, J. H., et al., Simple pyrolysis of urea into graphitic carbon nitride with recyclable adsorption and photocatalytic activity. *J. Mater. Chem.* **2011,** *21* (38), 14398-14401.

34. Lau, V. W. H., et al., Urea-Modified Carbon Nitrides: Enhancing Photocatalytic Hydrogen Evolution by Rational Defect Engineering. *Adv. Energy Mater.* **2017,** *7* (12), 1602251-n/a.

35. Liu, J., et al., Self-regenerated solar-driven photocatalytic water-splitting by urea derived graphitic carbon nitride with platinum nanoparticles. *Chem. Commun.* **2012,** *48* (70), 8826-8.

36. Kharlamov, A., et al., Features of the synthesis of carbon nitride oxide (g-C3N4)O at urea pyrolysis. *Diam Relat Mater* **2016,** *66* (Copyright (C) 2016 American Chemical Society (ACS). All Rights Reserved.), 16-22.

37. Shi, L., et al., Higher Yield Urea-Derived Polymeric Graphitic Carbon Nitride with Mesoporous Structure and Superior Visible-Light-Responsive Activity. *ACS Sustain. Chem. Eng.* **2015,** *3* (12), 3412-3419.

38. Rabe, E. J., et al., Proton-Coupled Electron Transfer from Water to a Model Heptazine-Based Molecular Photocatalyst. *J. Phys. Chem. Lett.* **2018,** *9* (21), 6257-6261.

39. Rabe, E. J., et al., Barrierless Heptazine-Driven Excited-State Proton-Coupled Electron Transfer: Implications for Controlling Photochemistry of Carbon Nitrides and Aza-Arenes. *J. Phys. Chem. C.* **2019,** *10.1021/acs.jpcc.9b08842*.

40. Zhang, J., et al., Co-monomer control of carbon nitride semiconductors to optimize hydrogen evolution with visible light. *Angew. Chem. Int. Ed.* **2012,** *51* (13), 3183-7.

41. Schroder, M., et al., Hydrogen Evolution Reaction in a Large-Scale Reactor using a Carbon Nitride Photocatalyst under Natural Sunlight Irradiation. *Energy Technol-Ger* **2015,** *3* (10), 1014-1017.

42. Corp, K. L.; Schlenker, C. W., Ultrafast Spectroscopy Reveals Electron-Transfer Cascade That Improves Hydrogen Evolution with Carbon Nitride Photocatalysts. *J. Am. Chem. Soc.* **2017,** *139* (23), 7904-7912.

43. Domcke, W., et al., Solar Energy Harvesting with Carbon Nitrides and N-Heterocyclic Frameworks: Do We Understand the Mechanism? *Chem. Photo. Chem.* **2019,** *3* (1), 10-23.

44. Ullah, N., et al., Photoinduced Water–Heptazine Electron-Driven Proton Transfer: Perspective for Water Splitting with g-C3N4. *J. Phys. Chem. Lett.* **2019**, 4310-4316.

45. Yamaji, M., et al., Verification of the electron/proton coupled mechanism for phenolic H-atom transfer using a triplet π,π∗ carbonyl. *Chem. Phys. Lett.* **2009,** *475* (4-6), 235-239.

46. Osako, T., et al., Oxidation Mechanism of Phenols by Dicopper−Dioxygen (Cu2/O2) Complexes. *J. Am. Chem. Soc.* **2003,** *125* (36), 11027-11033.

47. Bronner, C.; Wenger, O. S., Kinetic Isotope Effects in Reductive Excited-State Quenching of Ru(2,2′-bipyrazine)32+ by Phenols. *J. Phys. Chem. Lett.* **2012,** *3* (1), 70-74.

48. Warren, J. J., et al., Thermochemistry of Proton-Coupled Electron Transfer Reagents and its Implications. *Chem. Rev.* **2010,** *110* (12), 6961-7001.

49. Pinteala, M.; Schlick, S., Direct ESR detection and spin trapping of radicals generated by reaction of oxygen radicals with sulfonated poly(ether ether ketone) (SPEEK) membranes. *Polymer Degradation and Stability* **2009,** *94* (10), 1779-1787.

50. Bakulin, A. A., et al., The Role of Driving Energy and Delocalized States for Charge Separation in Organic Semiconductors. *Science* **2012,** *335* (6074), 1340-1344.

51. Bakulin, A. A., et al., Ultrafast Spectroscopy with Photocurrent Detection: Watching Excitonic Optoelectronic Systems at Work. *J. Phys. Chem. Lett.* **2016,** *7* (2), 250-258.

52. Dimitrov, S. D., et al., On the energetic dependence of charge separation in low-band-gap polymer/fullerene blends. *J. Am. Chem. Soc.* **2012,** *134* (44), 18189-92.

53. Mangold, H., et al., Control of charge generation and recombination in ternary polymer/polymer:fullerene photovoltaic blends using amorphous and semi-crystalline copolymers as donors. *Phys. Chem. Chem. Phys.* **2014,** *16* (38), 20329-20337.

54. Tan, Z. K., et al., Suppressing recombination in polymer photovoltaic devices via energy-level cascades. *Adv. Mater.* **2013,** *25* (30), 4131-8.

55. Zhang, J., et al., On the energetics of bound charge-transfer states in organic photovoltaics. *J. Mater. Chem. A* **2017,** *5* (23), 11949-11959.

56. Cabanillas-Gonzalez, J., et al., Pump-Probe Spectroscopy in Organic Semiconductors: Monitoring Fundamental Processes of Relevance in Optoelectronics. *Adv. Mater.* **2011,** *23* (46), 5468-5485.

57. Paternò, G. M., et al., Pump–Push–Probe for Ultrafast All-Optical Switching: The Case of a Nanographene Molecule. *Adv. Funct. Mater.* **2019,** *29* (21), 1805249.

58. Schirmer, J., Beyond the random-phase approximation: A new approximation scheme for the polarization propagator. *Phys. Rev. A* **1982,** *26* (5), 2395-2416.

59. Snellenburg, J. J., et al., Glotaran: A Java-Based Graphical User Interface for the R Package TIMP. *J. Stat. Softw.* **2012,** *49* (3), 22.

Appendix A: Supplementary Information for Chapter 3

Figure A-1 shows transient induced absorption decays near 1000 nm for graphitic and exfoliated carbon nitride. The transient kinetics suggests that the lifetime of any exciton or charged intermediate states, such as geminate charge transfer states, non-geminate charge separated species, polaron pairs, or exciplex states, are shorter than what we observe for electrons on graphitic carbon nitride. If one assumes that the electron absorption of exfoliated carbon nitride resides in a similar spectral region to that of graphitic carbon nitride, these data suggest that the photogenerated electrons of graphitic carbon nitride persist on significantly longer timescales than their exfoliated counterparts. Note that the amplitude of the graphitic carbon nitride signal is also nearly an order of magnitude larger than the amplitude of the TA signal in the same spectral region for the exfoliated carbon nitride. This mismatch in signal magnitude can be clearly seen in Figure A-6. The faster decay and the significantly suppressed TA signal magnitude exhibited by exfoliated carbon nitride suggests that this material does not independently sustain long-lived photoinduced charge separation when compared with graphitic carbon nitride. Our catalytic studies show that the mixture of graphitic carbon nitride and exfoliated carbon nitride outperforms either individual component. However, chemically exfoliated carbon nitride appears to be photocatalytically dormant on its own. Our spectroscopic results suggest that poor charge generation efficiency and rapid decay dynamics work in concert to effectively limit the reducing equivalents that can be provided solely by exfoliated carbon nitride on timescales relevant for proton reduction.

To illustrate the increase in tail state absorption, the ground state absorption is plotted on a semi-log scale in Figure A-2. After exfoliation the defect states are more pronounced. These defect states could be responsible for the catalytic activity,[1-3] however without significant charge generation after exfoliation, the catalyst cannot produce comparable amount of hydrogen.

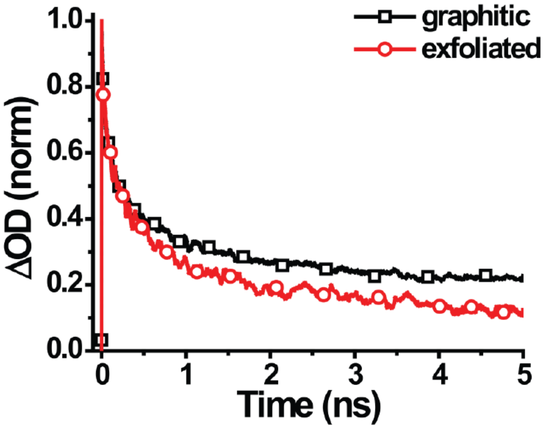

Figure A-1. Transient absorption kinetics of graphitic and exfoliated carbon nitride.
Transient absorption kinetics of graphitic carbon nitride and exfoliated carbon nitride averaged over 1000-1050 nm. Samples were excited with a 365 nm pump (1.6×10^{15} photons/cm^3/pulse). Spectra were collected in the absence of charge scavengers and without a platinum co-catalyst.

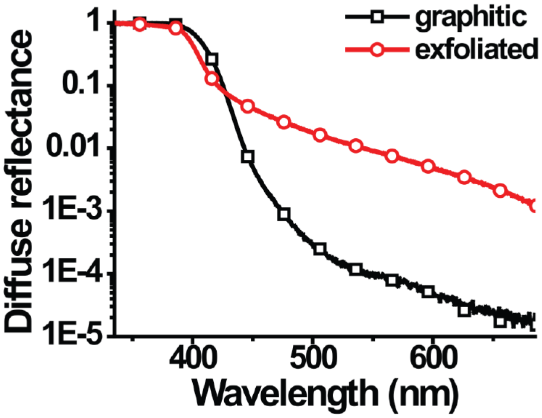

Figure A-2. Ground state absorption of graphitic and exfoliated carbon nitride
Ground state absorption of graphitic and exfoliated carbon nitride plotted on a semi-log scale. Spectra were collected in the absence of charge scavengers and without a platinum co-catalyst.

Figure A-3 demonstrates the decrease in size of regions of contrast in the transmission electron micrograph, corresponding to particle size, after exfoliation of graphitic carbon nitride.

The X-ray photoelectron spectroscopy (XPS) survey scan in Figure A-4 shows an increase in oxidative defects after exfoliation of graphitic carbon nitride. Oxygen content increases from 7% in graphitic carbon nitride to 17% in exfoliated carbon nitride, as shown in Table A-1. There is also a relative decrease in the number of carbon-carbon bonds (Figure A-5) relative to the number of tertiary carbon bonds, suggesting that some fraction of the heptazine ring units are severed but the nitrogen linkers between heptazine units remain largely intact during the exfoliation process.

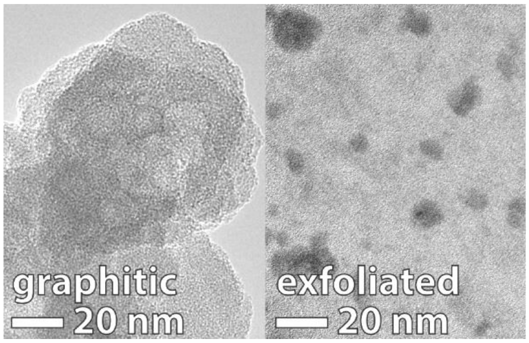

Figure A-3. TEM of graphitic and exfoliated carbon nitride.
Samples were not doped with platinum.

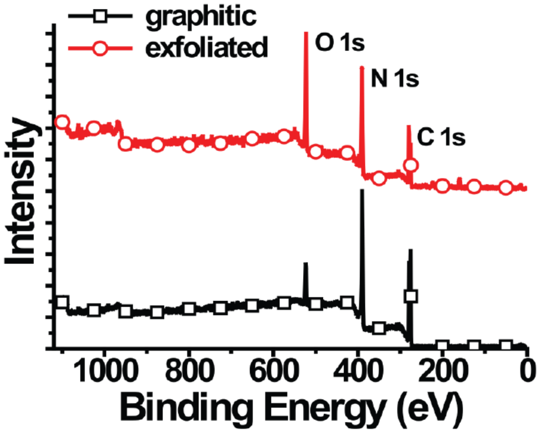

Figure A-4. XPS survey spectra of graphitic and exfoliated carbon nitride.
Samples were not doped with platinum.

Table A-1. XPS elemental analysis of graphitic and exfoliated carbon nitride species.

	Carbon	*Nitrogen*	*Oxygen*
Graphitic	60.6%	32.4%	7%
Exfoliated	42%	41%	17%

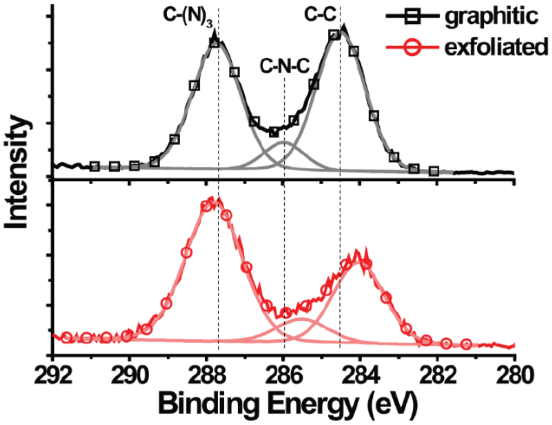

Figure A-5. XPS carbon 1s spectra of graphitic and exfoliated carbon nitride.
XPS carbon 1s spectra for graphitic (black) and exfoliated carbon nitride (red) with approximate deconvolutions of individual carbon peaks (grey and light red). Open symbols are the fitted peak envelop. Samples were not doped with platinum.

Figure A-6 demonstrates the correlation of the ground state absorption spectrum with the bleach of the ground state in the differential absorption spectrum obtained under cathodic conditions by spectroelectrochemistry. In Figure A-6 we also present the correlation between the singlet exciton emission from photoluminescence and the stimulated emission peak that we observe in the transient absorption signal.

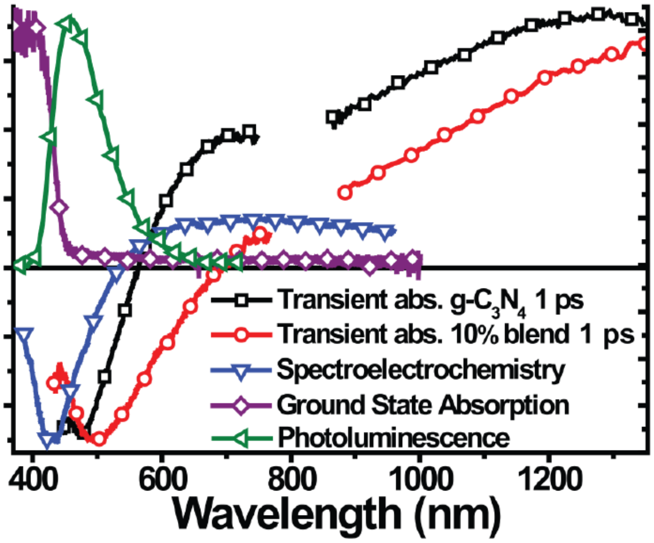

Figure A-6. Ground and excited-state spectra overlapped for reference.
Transient absorption, reductive (-0.5 V vs NHE) spectroelectrochemistry, ground state absorption, and photoluminescence spectra of graphitic carbon nitride plotted together for reference. Spectra were collected in the absence of charge scavengers and without a platinum co-catalyst.

In Figure A-7 we compare the transient absorption spectra of graphitic carbon nitride and chemically exfoliated carbon nitride collected under comparable excitation densities. There is nearly one order of magnitude decrease in the signal following exfoliation, which suggests that photoinduced charge generation is considerably less efficient in exfoliated carbon nitride when compared to graphitic carbon nitride.

Figure A-8 demonstrates the quenching of the electron absorption feature in graphitic carbon nitride after addition of persulfate or nitrate ions. The negative feature from 900 – 1100 nm that arises after the addition of sodium persulfate is likely due stimulated emission from low-energy tail states or aggregates.

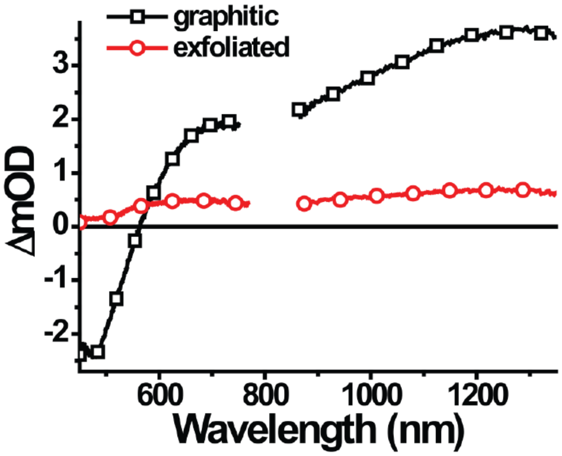

Figure A-7. Transient absorption spectra of graphitic and exfoliated carbon nitride.

Transient absorption spectra comparing signal magnitudes (both pumped at 365 nm, 1.6×10^{15} photons/cm^3/pulse). Spectra were collected in the absence of charge scavengers and without a platinum co-catalyst.

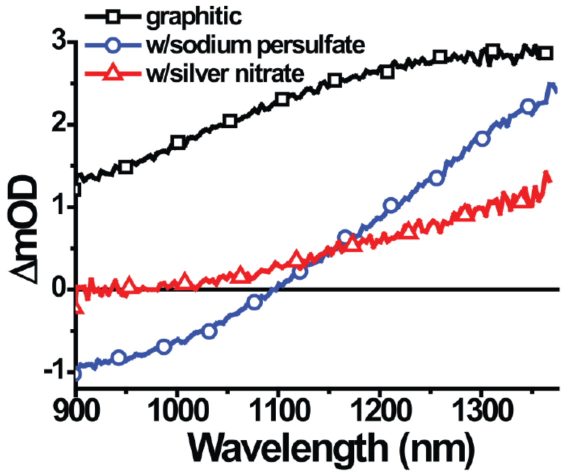

Figure A-8. Transient absorption spectra of graphitic carbon nitride with e$^-$ scavengers.

Transient absorption spectra of graphitic carbon nitride with two different electron scavengers at 1 ps after stimulated with a 365 nm pulse (1.6×10^{15} photons/cm^3/pulse). Spectra were collected in the absence of a hole scavenger and without a platinum co-catalyst.

Transient absorption quenching experiments demonstrate that the induced absorption feature at 1000 – 1050 nm that we associated with carbon nitride electron absorption is dynamically quenched in the presence of various electron scavengers and exfoliated carbon nitride but not in the presence of a hole scavenger, such as triethanolamine, methanol and oxalate (Figure 3-5 and Figure 3-5c). Conversely, the kinetics from 1275 – 1325 nm are insensitive to the presence of electron scavengers or exfoliated carbon nitride (Figure A-9), suggesting that the main species that absorbs near 1275 nm is not the electron on graphitic carbon nitride.

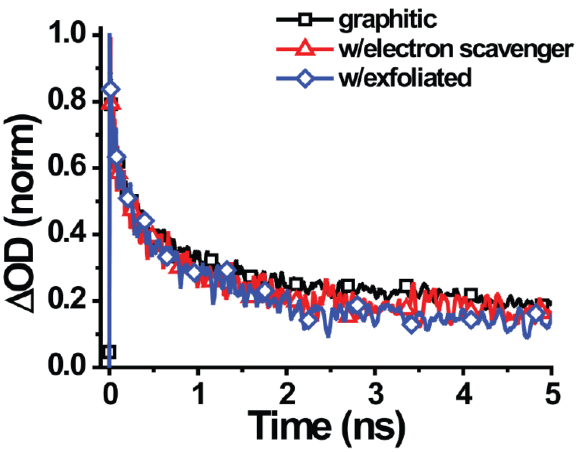

Figure A-9. Transient absorption kinetics of graphitic carbon nitride monitored from 1275 – 1325 nm with an electron scavenger or exfoliated carbon nitride.
Samples were pumped at 365 nm (1.6×10^{15} photons/cm^3/pulse). Spectra were collected in the absence of a hole scavenger and without a platinum co-catalyst.

When we add various electron scavengers (e.g. nitrate, persulfate, or sulfate) to suspensions of g-C_3N_4 we observe rapid (ps – ns timescale) quenching of the transient absorption (TA) signal in the 600 nm – 1100 nm spectral region (Figure 3-5 and Figure A-8). However, within the same time window, we observe no significant quenching of any portion of the TA signal (Figure 3-5b) upon adding common hole scavengers (e.g. methanol, triethanolamine, or oxalate). This suggests sluggish kinetics for the hole transfer process if the hole absorption is within our spectral window. In order to monitor hole quenching on much longer timescales, we used quasi-cw photomodulation methods. Photoinduced absorption (PIA) spectroscopy is a photomodulation technique that allows us to probe the spectra of transient species with relatively long μs – ms lifetimes. To perform PIA spectroscopy measurements, we used mechanically chopped monochromatic illumination from a 365 nm LED source as the pump light to photoexcite aqueous suspensions of g-C_3N_4 alone or g-C_3N_4 with a hole scavenger (oxalate in Figure A-10). We recorded the resulting change in probe light transmitted through the sample from a monochromated halogen lamp using a two-color Si/InGaAs detector coupled through a current preamplifier to a multimeter and a lock-in amplifier. Based on the normalized differential transmittance ($\Delta T/T$) that we measure as a function of probe wavelength (λ), we calculate the change in optical density of the sample upon photoexcitation as $\Delta \mu OD = -\log(1 + \Delta T/T) \times 10^6$. Oxalate is a common hole scavenger for both transient absorption studies[4] and steady state photochemical reduction reactions.[5] It has also been shown to be a more kinetically competent hole scavenger than methanol or triethanolamine as a sacrificial electron donor for carbon nitride during photocatalytic hydrogen evolution.[6] In Figure A-10 we show the pronounced quenching of the long-lived PIA signal intensity at probe wavelengths $\lambda > 1200$ nm that results upon adding oxalate to a suspension of g-C_3N_4. We do not observe quenching of this signal on faster timescales using oxalate or any other hole scavenger that we have studied, indicating that the charge transfer kinetics for this process appear to be orders of magnitude slower than those that we observe for photoinduced electron quenching. The kinetics in the 1275-1325 nm region of the TA spectrum exhibit marked fluence-dependence, with faster decay at higher excitation densities that we typically associate with non-geminate, bimolecular, and second-order decay processes. Therefore, this optical signal does not appear to be associated with a neutral excitonic species or a geminate charge transfer state, either of which would exhibit quasi-first order decay kinetics. The marked fluence-dependence and insensitivity to the presence of known electron scavengers suggest that the species near 1275 nm arises due to the presence of a positive charge carrier (hole) on graphitic carbon nitride. The quenching of the long-lived μs – ms PIA component in Figure A-10 is consistent with our assignment of the induced absorption feature near $\lambda = 1275$ nm in our TA measurements as that of holes on g-C_3N_4.

We also measured the transient absorption signal for the electron lifetime on intermediate timescales on the order of several tens of nanoseconds for graphitic carbon nitride in the presence of electron and hole scavengers. As we show in Figure A-11, the rapid electron quenching for the electron signal at 700-750 nm is consistent with our early-time picosecond to nanosecond measurements. Additionally, on this intermediate timescale we also observe that the electron decay becomes slightly delayed in the presence of oxalate, consistent with inhibited electron/hole recombination upon the removal of photoinduced holes from carbon nitride via the oxidation of sacrificial $C_2O_4^{-2}$ ions. Based on our spectroscopic results, the rates of nitrate, persulfate, or sulfate reduction (as well as exfoliated carbon nitride) by photoinduced electron transfer from g-C_3N_4 appear to be orders of magnitude faster than the oxidation rates of oxalate ions, triethanolamine, or methanol. These observations that suggest slow photoinduced hole transfer rates are consistent with the fact that we observe no significant quenching of the 1275 nm TA signal on short (ps – ns) timescales.

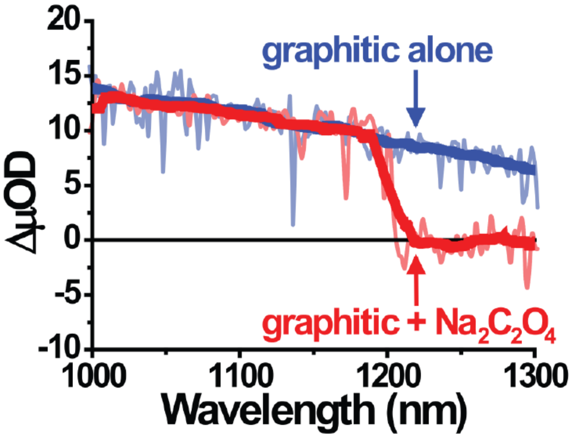

Figure A-10. Photoinduced absorption (PIA) spectroscopy shows quenching of photogenerated holes in graphitic carbon nitride by sodium oxalate on millisecond timescales.
In the absence of sodium oxalate ($Na_2C_2O_4$), g-C_3N_4 alone (translucent blue trace) exhibits a broad induced absorption feature that spans the near-infrared region of the quasi-cw PIA spectrum. Adding oxalate as a hole scavenger (translucent red trace) selectively quenches the low-energy spectral signal ($\lambda > 1200$ nm) of the long-lived PIA component that we observe for g-C_3N_4. Bold solid lines serve as a guide to the eye and represent adjacent averaging of the measured data (translucent traces). PIA spectra were collected with 365 nm pump at 187 Hz modulation frequency without platinum doping.

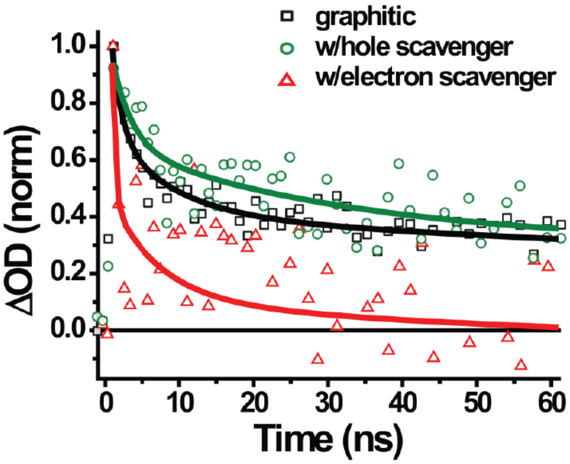

Figure A-11. Nanosecond transient absorption kinetics of carbon nitride with charge scavengers.
Intermediate timescale transient absorption kinetics monitored from 700-750 nm of graphitic carbon nitride in the presence of an electron scavenger or a hole scavenger. The data is plotted with trend lines since the long timescale transient absorption measurement is quite noisy. Samples were pumped at 365 nm (1.4×10^{16} photons/cm^3/pulse) and spectra were collected in the absence of platinum loading.

REFERENCES

1. Zhang, H., et al., Pyridine derivative/graphene nanoribbon composites as molecularly tunable heterogeneous electrocatalysts for the oxygen reduction reaction. *Phys Chem Chem Phys* **2016,** *18* (6), 5040-7.
2. Wang, W., et al., g-C3N4 quantum dots: direct synthesis, upconversion properties and photocatalytic application. *Chemical Communications* **2014,** *50*, 10148-10150.
3. Lau, V. W., et al., Low-molecular-weight carbon nitrides for solar hydrogen evolution. *J Am Chem Soc* **2015,** *137* (3), 1064-72.
4. Zhao, R.-K., et al., Ultrafast transient mid IR to visible spectroscopy of fully reduced flavins. *Physical Chemistry Chemical Physics* **2011,** *13* (39), 17642-17648.
5. Ghisla, S.; Massey, V., Mechanism of inactivation of the flavoenzyme lactate oxidase by oxalate. *Journal of Biological Chemistry* **1975,** *250* (2), 577-84.
6. Lau, V. W.-h., et al., Rational design of carbon nitride photocatalysts by identification of cyanamide defects as catalytically relevant sites. *Nat Commun* **2016,** *7*.

Appendix B: Supplementary Information for Chapter 4

K_A determination using ground state absorption

Ground state absorption was used to monitor the formation of TAHz-R-PhOH complexes prior to photoexcitation. To account for any changes to the baseline, each spectrum was averaged from 495-500 nm (where there is no TAHz absorption) and subtracted from the spectrum. We chose to plot the change in absorption at 380 nm because of the large change at that wavelength, resulting in the cleanest fit. Additionally, this is far away from any tail absorption of the phenols. Using the difference in absorption at 380 nm we calculated the association constant between TAHz and the series of phenols. In this fit both the change in molar absorptivity ($\Delta\varepsilon_{380}$) between free TAHz and the bound complex as well as the association constant (K_A) were parameters. In all cases the derived $\Delta\varepsilon_{380}$ was around 50,000 $M^{-1}cm^{-1}$.

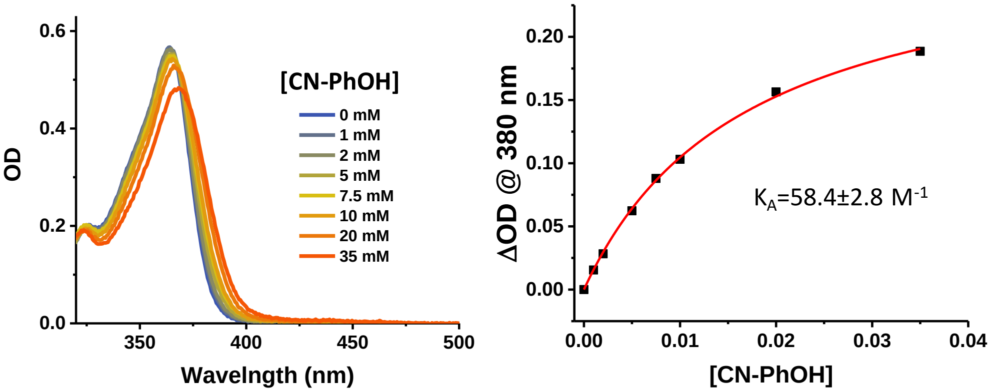

Figure B-1. Absorption of TAHz as a function of CN-PhOH concentration. Concentrations ranging from 0-35 mM (left). Fitting the difference in absorption at 380 nm versus the concentration of phenol gives a K_A= 58.4±2.8 M^{-1} (right).

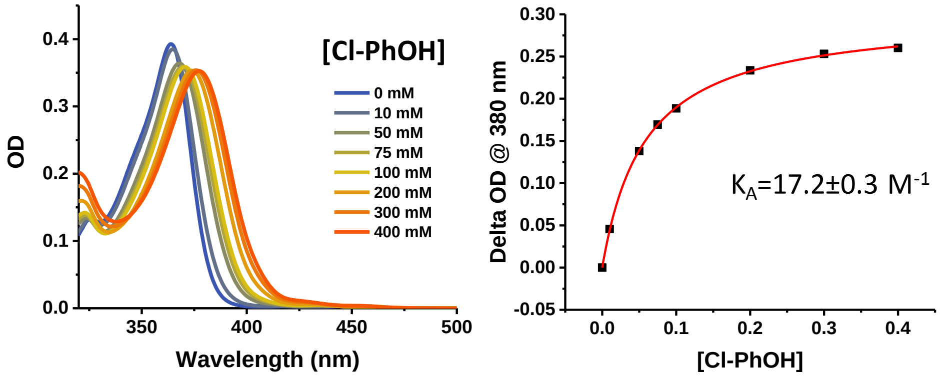

Figure B-2. Absorption of TAHz as a function of Cl-PhOH concentration. Concentrations ranging from 0-400 mM (left). Fitting the difference in absorption at 380 nm versus the concentration of phenol gives a K_A= 17.2±0.3 M^{-1} (right).

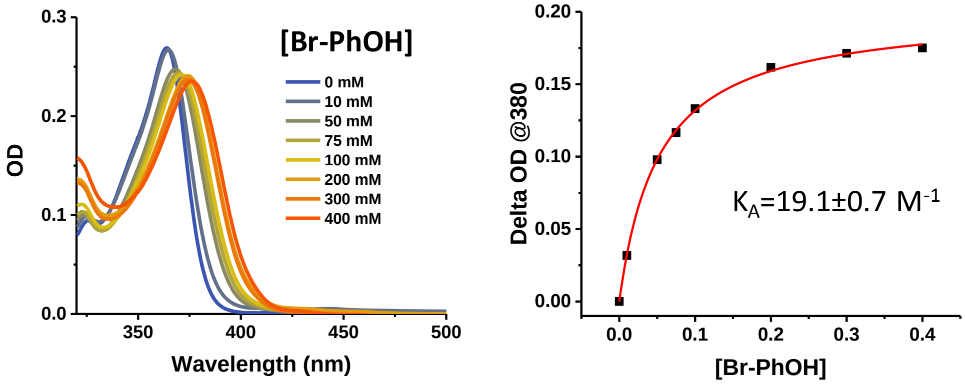

Figure B-3. Absorption of TAHz as a function of Br-PhOH concentration. Concentrations ranging from 0-400 mM (left). Fitting the difference in absorption at 380 nm versus the concentration of phenol gives a K_A= 19.1±0.7 M^{-1} (right).

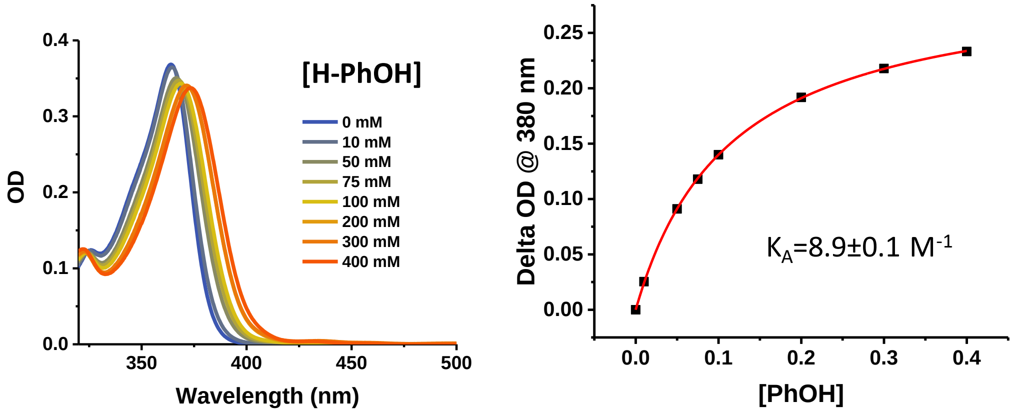

Figure B-4. Absorption of TAHz as a function of H-PhOH concentration. Concentrations ranging from 0-400 mM (left). Fitting the difference in absorption at 380 nm versus the concentration of phenol gives a K_A= 8.9±0.1 M^{-1} (right).

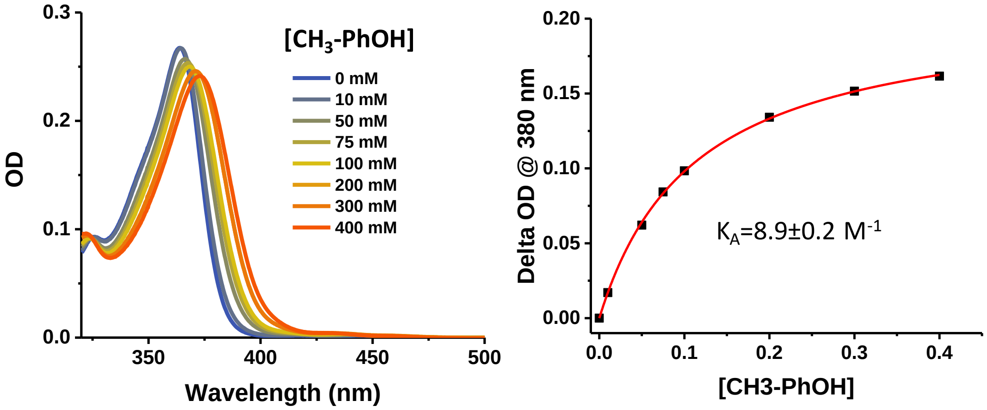

Figure B-5. Absorption of TAHz as a function of CH_3-PhOH concentration. Concentrations ranging from 0-400 mM (left). Fitting the difference in absorption at 380 nm versus the concentration of phenol gives a K_A= 8.9±0.2 M^{-1} (right).

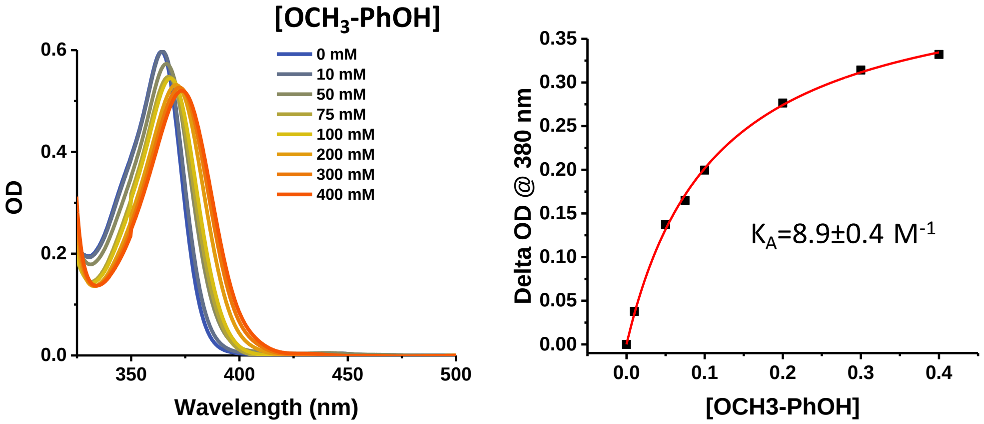

Figure B-6. Absorption of TAHz as a function of OCH_3-PhOH concentration. Concentrations ranging from 0-400 mM (left). Fitting the difference in absorption at 380 nm versus the concentration of phenol gives a K_A= 8.9±0.4 M^{-1} (right).

k_Q determination via lifetime quenching

We took lifetime measurements of TAHz:R-PhOH systems in a range of concentrations using the TCSPC system mentioned above. We plotted the data according to $\frac{1}{\tau} = k_f + k_Q[Q]$, where τ is the florescence lifetime, k_f is the radiative rate constant, k_Q is the quenching rate constant, and [Q] is the concentration of phenol. In this case, the slope is quenching rate constant for each phenol derivative. For CN-PhOH the concentration range was 2-10 mM and for all other phenols, the concentration range was 25- 125 mM. Due to residual pump light out to 5 ns, we fit all decay curves after this time period. This effectively cut out the fast lifetime component attributed to the hydrogen-bound complex. This only allows us to report on the quenching of free TAHz as a function of phenol concentration.

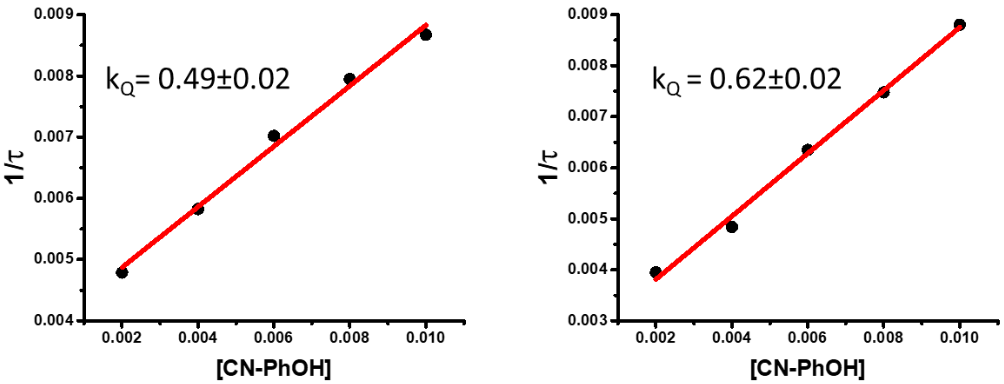

Figure B-7. Stern-Volmer quenching data for TAHz with CN-PhOH.
Gives an average k_Q=0.56 s^{-1}. The range of CN-PhOH concentrations was limited by the solubility of CN-PhOH in toluene.

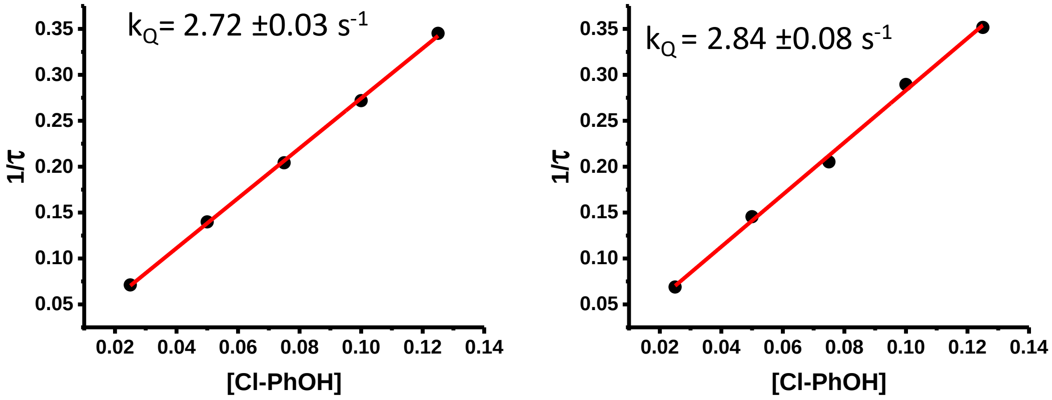

Figure B-8. Stern-Volmer quenching data for TAHz with Cl-PhOH.
Gives an average k_Q=2.78 s^{-1}.

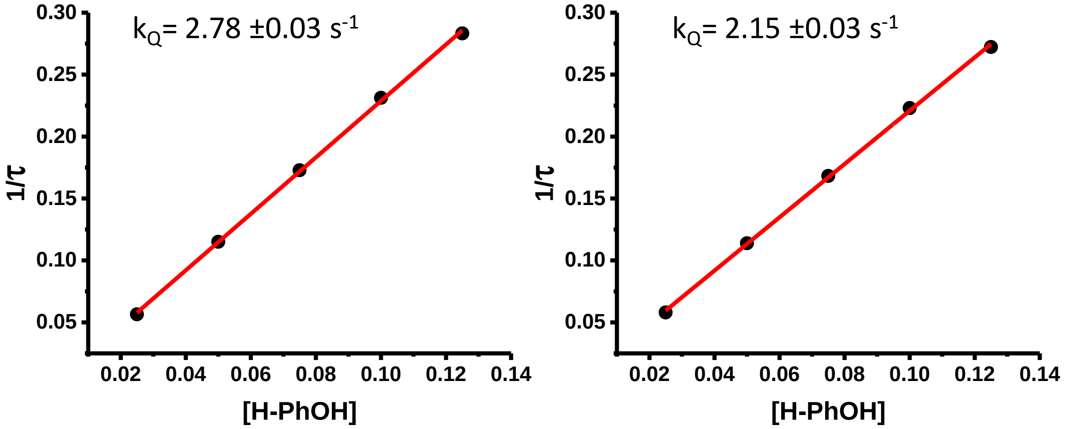

Figure B-9. Stern-Volmer quenching data for TAHz with H-PhOH.
Gives an average k_Q=2.21 s^{-1}.

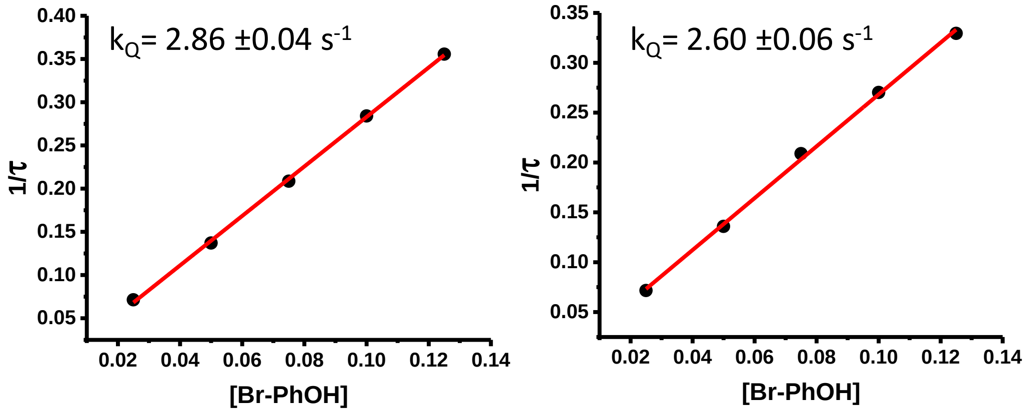

Figure B-10. Stern-Volmer quenching data for TAHz with Br-PhOH.
Gives an average k_Q=2.73 s^{-1}.

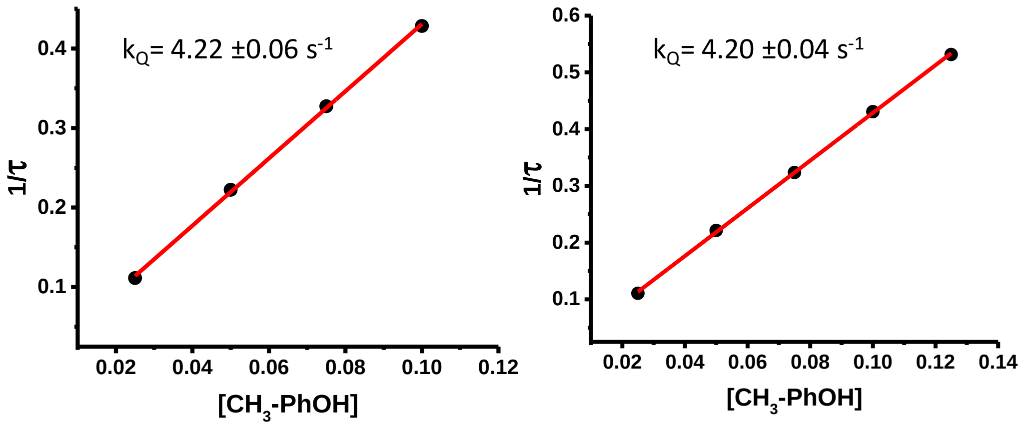

Figure B-11. Stern-Volmer quenching data for TAHz with CH_3-PhOH. Gives an average k_Q=4.21 s^{-1}.

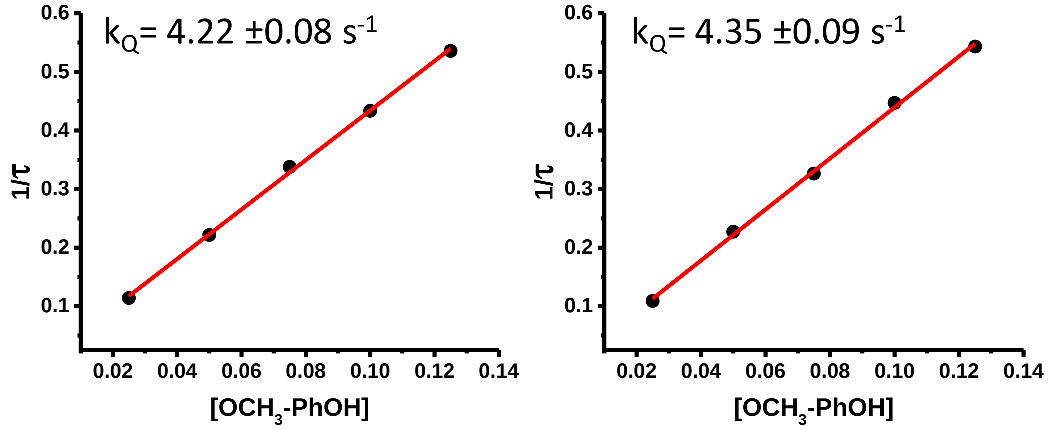

Figure B-12. Stern-Volmer quenching data for TAHz with OCH_3-PhOH. Gives an average k_Q=4.26 s^{-1}.

k_Q determination via intensity quenching

We took PLQY measurements of TAHz:R-PhOH systems in a range of concentrations (0-10 mM) to find the quenching constant and compare to the quenching constant found via lifetime quenching seen above. By plotting the ratio of the PLQY in the absence and presence of quencher (I_0/I), we can find the quenching rate constant (k_Q) by using $\frac{I_0}{I} = 1 + \frac{k_Q}{k_f}[Q]$ and knowing the fluorescence rate constant of TAHz in toluene without quencher, 3.486×10^6 s^{-1}.[1]

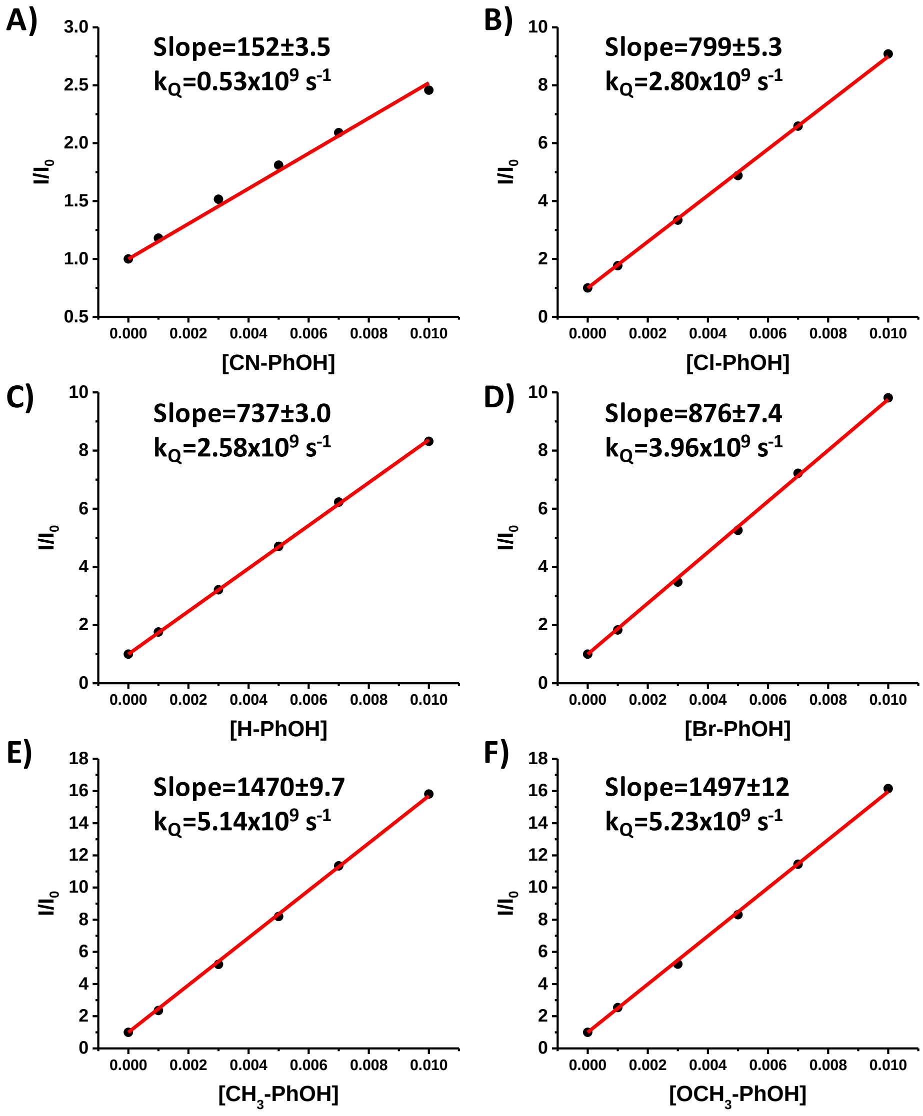

Figure B-13. Stern-Volmer quenching plots for TAHz.
A) CN-PhOH, B) CL-PhOH, C) H-PhOH, D) Br-PhOH, E) CH_3-PhOH, F) OCH_3-PhOH in toluene using PLQY values upon 365 nm excitation.

TR-PL of TAHz in toluene

Without phenol present, the TAHz emission decays monoexponentially across the entire spectrum (Figure B-14). Therefore, we attribute the fast component of the PL spectrum of TAHz and PhOH solutions to a hydrogen-bound TAHz-PhOH complex. We see this fast component with all phenol derivatives except OCH_3-PhOH (Figure B-20).

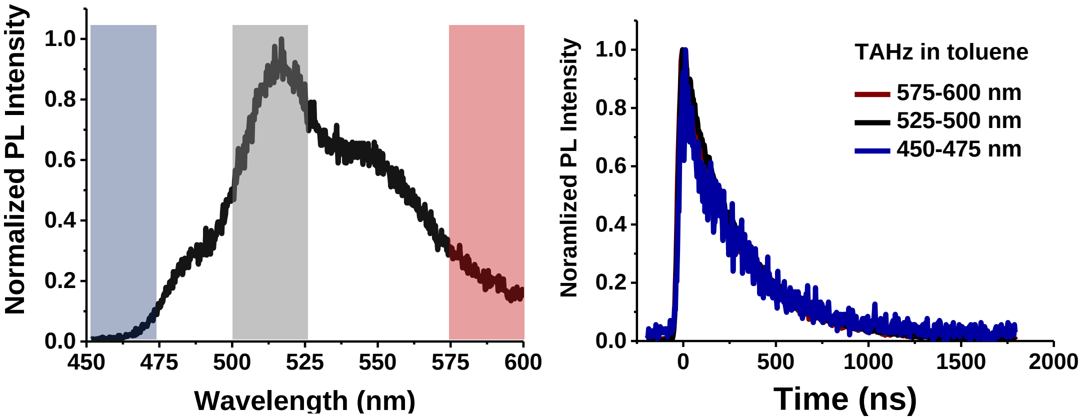

Figure B-14. The emission spectrum and decay of TAHz in toluene.
Without an abstractable hydrogen present the luminescence spectrum (left) shows a single exponential decay rate (right).

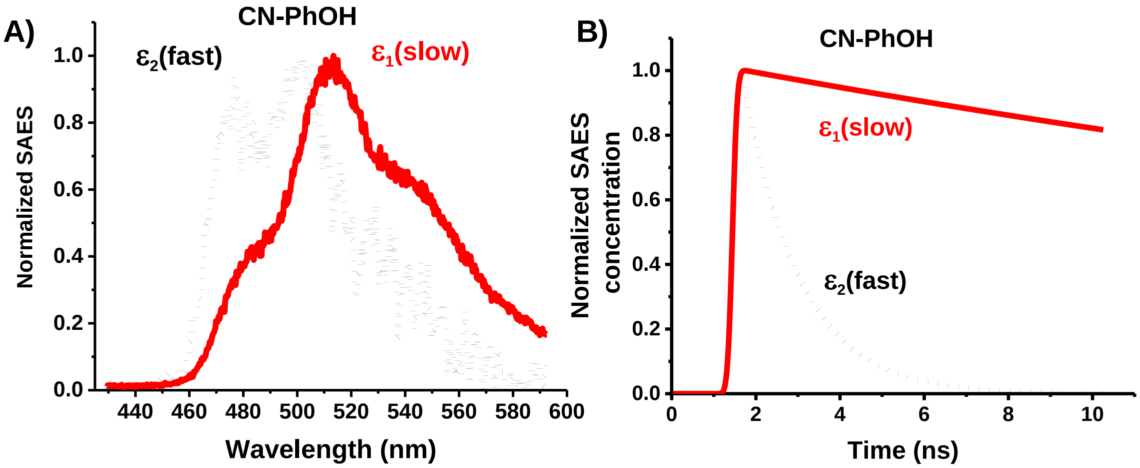

Figure B-15. Global target analysis of the TR-PL data of TAHz and 50 mM CN-PhOH.
It shows two species associated emission spectra (SAES) (A) and distinct kinetic decays (B). Emission attributed to the S_1 state, labeled ϵ_1 (red), is the emission shape seen in steady-state measurements. The second SAES, labeled ϵ_2 (dotted black), is seen at higher energies and decays notably faster than ϵ_1.

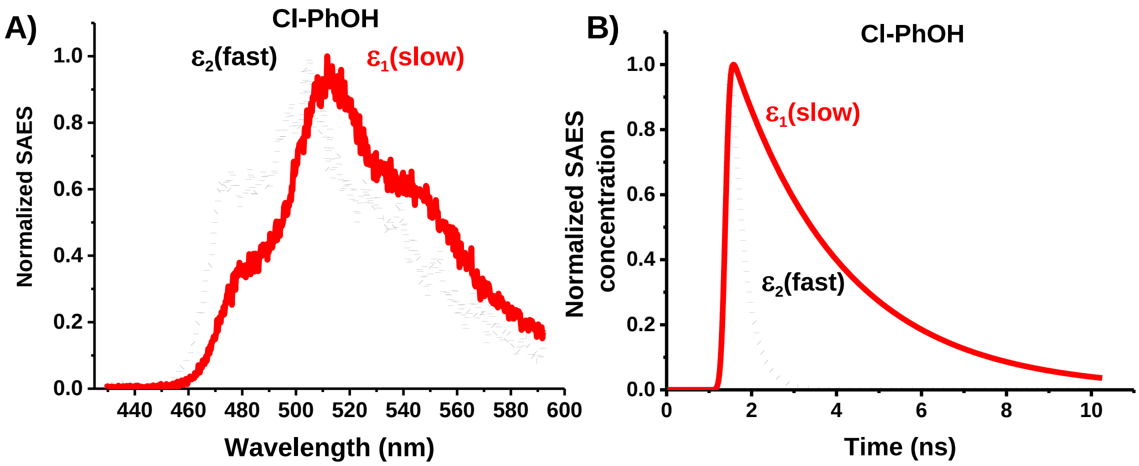

Figure B-16. Global target analysis of the TR-PL data of TAHz and 100 mM Cl-PhOH.
It shows two species associated emission spectra (SAES) (A) and distinct kinetic decays (B). Emission attributed to the S_1 state, labeled ϵ_1 (red), is the emission shape seen in steady-state measurements. The second SAES, labeled ϵ_2 (dotted black), is seen at higher energies and decays notably faster than ϵ_1.

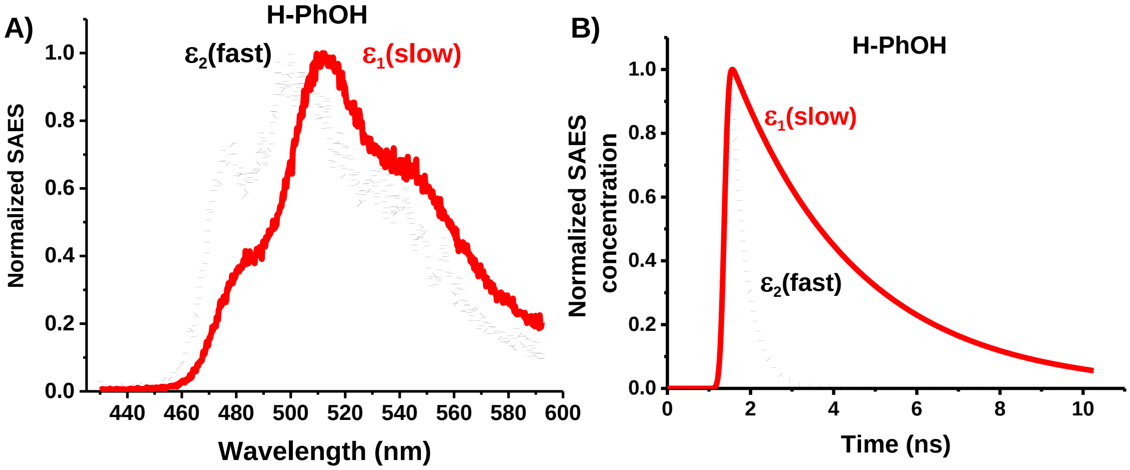

Figure B-17. Global target analysis of the TR-PL data of TAHz and 100 mM H-PhOH. It shows two species associated emission spectra (SAES) (A) and distinct kinetic decays (B). Emission attributed to the S_1 state, labeled ϵ_1 (red), is the emission shape seen in steady-state measurements. The second SAES, labeled ϵ_2 (dotted black), is seen at higher energies and decays notably faster than ϵ_1.

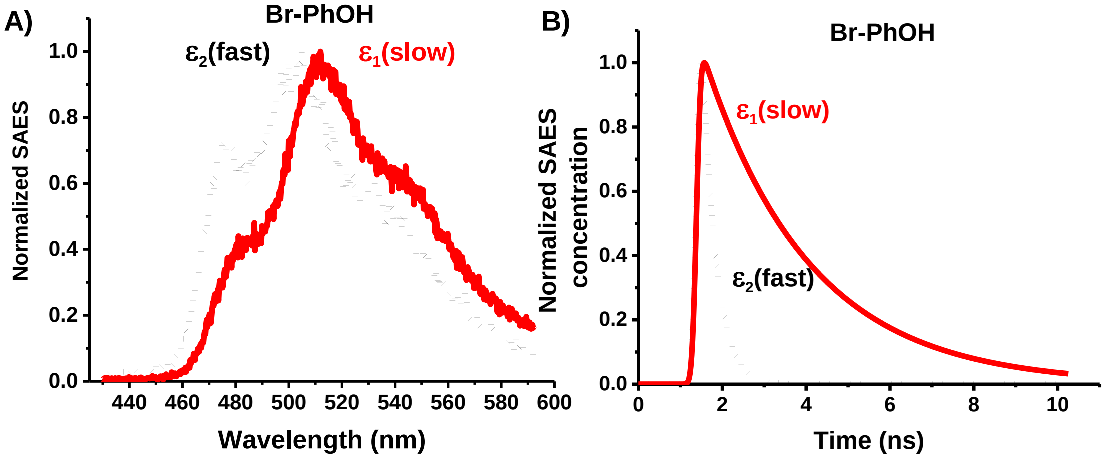

Figure B-18. Global target analysis of the TR-PL data of TAHz and 100 mM Br-PhOH. It shows two species associated emission spectra (SAES) (A) and distinct kinetic decays (B). Emission attributed to the S_1 state, labeled ϵ_1 (red), is the emission shape seen in steady-state measurements. The second SAES, labeled ϵ_2 (dotted black), is seen at higher energies and decays notably faster than ϵ_1.

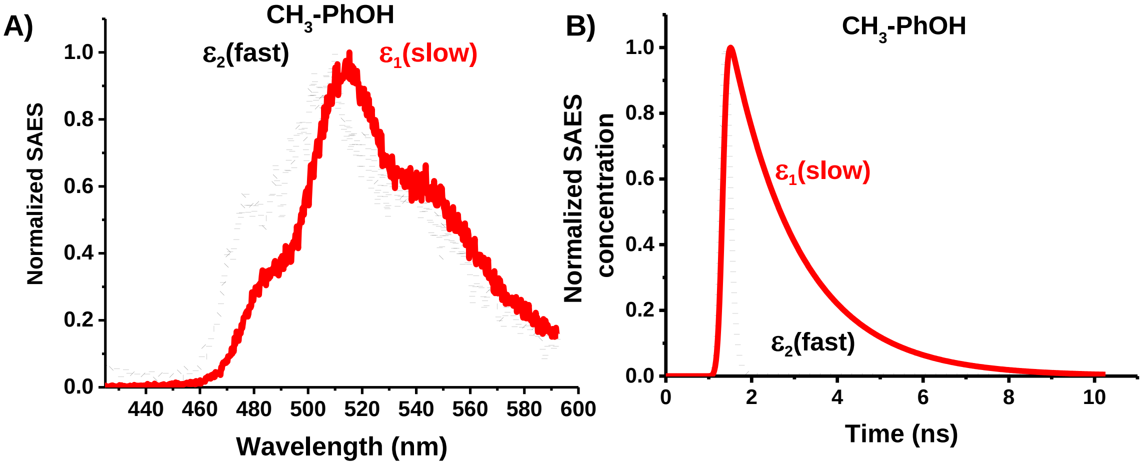

Figure B-19. Global target analysis of the TR-PL data of TAHz and 100 mM CH_3-PhOH.
It shows two species associated emission spectra (SAES) (A) and distinct kinetic decays (B). Emission attributed to the S_1 state, labeled ϵ_1 (red), is the emission shape seen in steady-state measurements. The second SAES, labeled ϵ_2 (dotted black), is seen at higher energies and decays notably faster than ϵ_1.

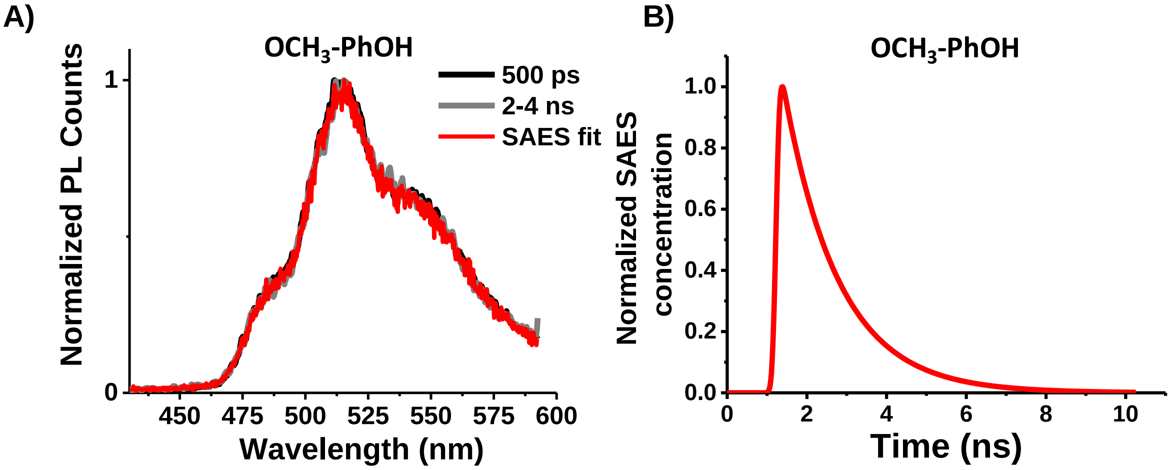

Figure B-20. The TR-PL of OCH_3-PhOH – a single component.
A) Normalized spectra of TAHz PL at 500 ps (black) and 2-4 ns (grey) show not spectral difference. The global analysis of the data showed the best fit with only one component, the spectrum of the species associated emission spectra (SAES) is shown in red. B) The kinetic decay of the SAES has a lifetime of 1.37 ns.

Electrochemistry

Cyclic voltammograms of TAHz in THF taken inside an argon glovebox are shown in Figure B-21. The 73 mV peak separation suggests this reduction is reversible. From this reduction CV we can estimate the electron affinity (EA), which corresponds to the LUMO, to be -2.85 eV relative to vacuum.[2] Using the singlet energy, we can estimate the excited state electron affinity (EA*) to be -5.99 eV relative to vacuum. This energy landscape is depicted in Figure B-21. The EA* represented the driving force for one-electron reduction of the photoexcited TAHz molecule.

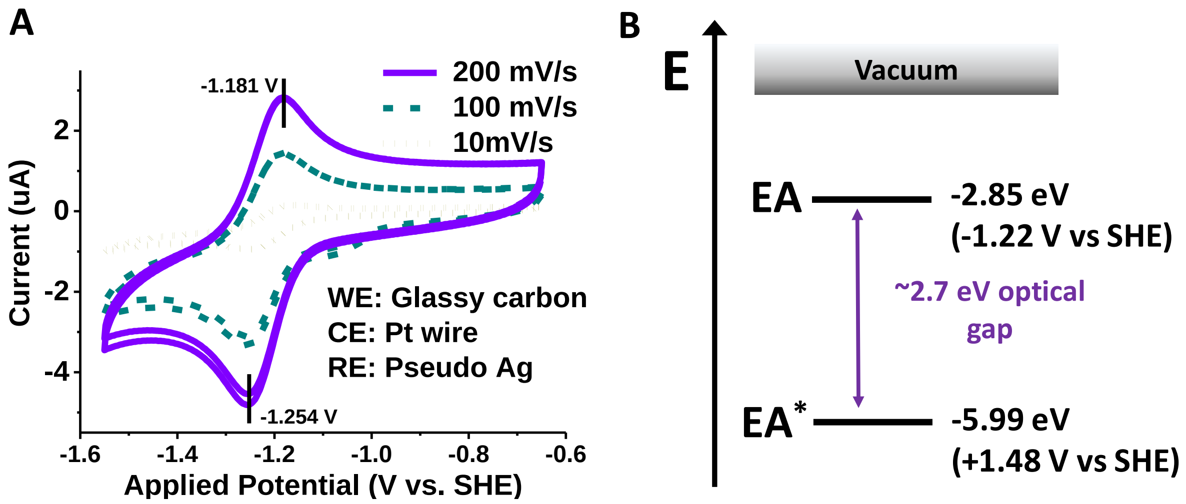

Figure B-21. Cyclic voltammogram of TAHz in THF.
A) Cathodic cyclic voltammogram of 475 μM TAHz in THF with 250 mM TABPF$_6$ as the supporting electrolyte. The reversible reduction allows us to calculate the E$_{red}$ to be -1.22 V vs SHE. This allows us to calculate the electron affinity (EA) and excited state electron affinity (EA*) shown in B.

Computational Methods

The geometries of the heptazine with PhOH, CN-PhOH, Br-PhOH, Cl-PhOH, CH_3-PhOH and OCH_3-PhOH complexes were obtained by minimizing the energy of the electronic ground-state using second-order Møller-Plesset perturbation theory (MP2).[3] The equilibrium geometries of them were optimized in C_s symmetry to speed up convergence. Vertical excitation energies were evaluated at these geometries using the second-order algebraic diagrammatic construction scheme (ADC(2)).[4] MP2 and ADC(2) have been benchmarked in previous studies and have turned out to be reliable tools to describe H-atom transfer reactions from water to carbon-nitride chromophores.[5-6]

For the two-dimensional potential-energy surfaces, the OH- and ON-distances were kept fixed and all other degrees of freedom were relaxed in order to minimize the energy of the lowest excited-state of A' symmetry. The C_s symmetry constraint has been applied for all calculations along the scans to be able to optimize the first excited state of A' symmetry.

Minimum energy geometries of the S_1 states of the systems were obtained by relaxation of all degrees of freedom in order to minimize the energy of the S_1 state using the C_s symmetry constraint.

The saddle point geometries of the lowest excited-state of A' symmetry are approached through structure optimization using the Trust Radius Image Minimization algorithm[7], which maximizes the energy along the only Hessian eigenvector with imaginary frequency while minimizing it along all the other directions. This particular vector should describe the H-atom transfer from phenol (or its derivatives) to heptazine. The estimated geometry of the saddle point from the two-dimensional potential energy surface served as initial guess for the saddle point optimization. After the optimization a frequency calculation was performed to confirm that there is only one mode with an imaginary frequency at the saddle point geometry.

For all calculations Dunning's correlation-consistent double ξ basis set (cc-pVDZ)[8] has been used and the resolution-of-identity[9] approximation was applied. Calculations were performed with the Turbomole program package.[10]

Computational results

Table B-1. Experimental data (for TAHz) and computational data (for Hz) for the hydrogen bonded complexes with the phenol derivatives, where R describes the substituent.
The energies of the first excited singlet state (S_1) at the ground-state equilibrium geometry (S_1^{GS}), at the equilibrium geometry (S_1^{min}), and at the geometry of the transition state of the ES-PCET reaction (S_1^{TS}) are given. S_{CT}^{GS} is the vertical excitation energy of the lowest charge-transfer state. ΔE^{min} is the vibrational stabilization energy of the S_1 state. $\Delta E^{\ddagger}$ is the barrier height for the ES-PCET on the S_1 potential-energy surface calculated as the energy difference between the energy of the transition state and the energy minimum of the locally excited S_1 state.

Experimental Data				Computational Data (eV)					
R	**E_0 ($RPhOH^+$/ RPhOH)**	**k_Q ($\times 10^9$ s^{-1}) PLQY**	**S_1 KIE**	**S_1^{GS}**	**S_{CT}^{GS}**	**S_1^{min}**	**ΔE^{min}**	**S_1^{TS}**	**$\Delta E^{\ddagger}$**
CN	2.03	0.532	1.9	2.61	3.86	2.52	0.085	2.89	0.369
Cl	1.88	2.80	1.4	2.60	3.45	2.52	0.083	2.69	0.169
Br	1.86	3.06	1.4	2.60	3.44	2.52	0.083	2.70	0.177
H	1.88	2.58	1.5	2.60	3.44	2.51	0.083	2.68	0.167
CH_3	1.79	5.14	1.2	2.60	3.23	2.51	0.082	2.61	0.093
OCH_3	1.68	5.23	1.1	2.59	2.80	2.51	0.081	----	----

Transition Structures

The geometries at the saddle point of heptazine with phenol and its derivatives are shown in Figure B-22, except for heptazine with OCH_3-PhOH, as there is no barrier and saddle point along the ES-PCET. The structures are ordered according to their hydrogen bond length.

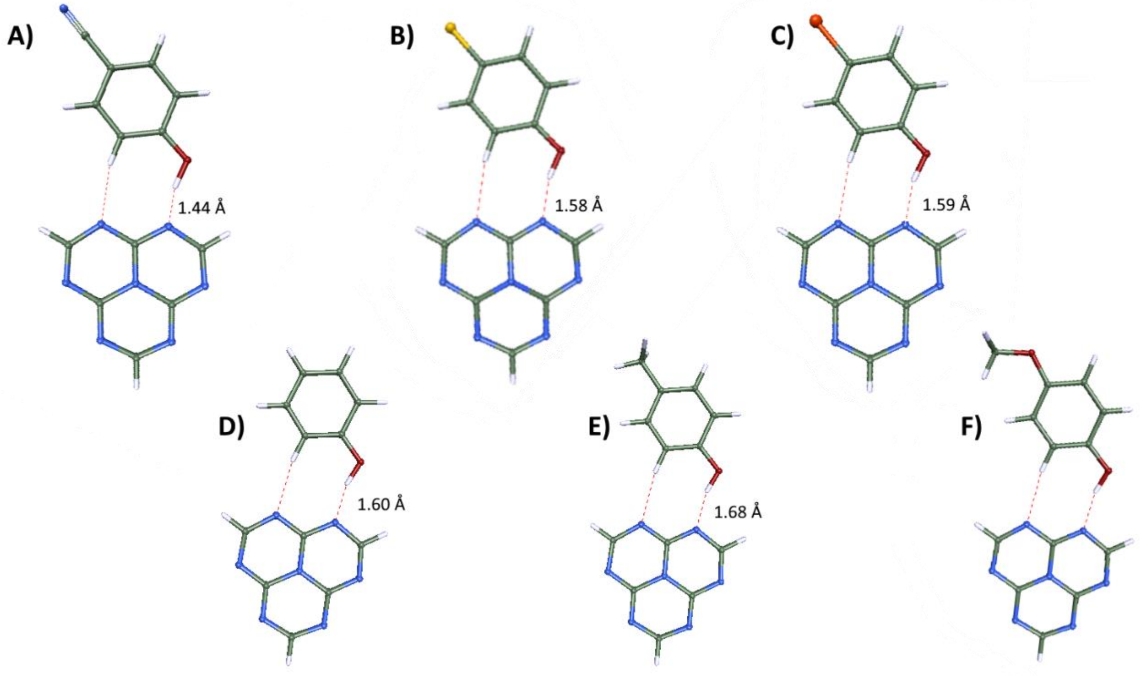

Figure B-22. Geometries of heptazine with A) CN-PhOH, B) Cl-PhOH, C) Br-PhOH, D) PhOH, E) CH_3-PhOH complexes at their transition state.
The geometry of heptazine with F) OCH_3-PhOH is an arbitrary structure between the FC point and the biradical state.

As optimization of the saddle points is a subtle task, the cartesian coordinates of the transition structures are given below for future benchmark calculations.

Heptazine with CN-PhOH:

C	2.2300760	-0.1260324	0.0000174
C	2.2186703	1.3014175	0.0000033
C	3.4540070	2.0159678	-0.0000115
C	4.6646841	1.3329382	-0.0000153
C	4.6655797	-0.0867014	-0.0000037
C	3.4473697	-0.8073914	0.0000134
O	1.1102537	2.0138420	-0.0000021
C	5.9179955	-0.7975145	-0.0000105
N	6.9515294	-1.3814581	-0.0000165
N	-1.1736144	0.9961279	0.0000169

C	-2.0876844	2.0225264	0.0000165
N	-3.4254300	1.9066063	0.0000076
C	-3.9273367	0.6680358	-0.0000010
N	-3.0361251	-0.4593672	0.0000008
C	-1.6419182	-0.2590085	0.0000101
N	-5.2464075	0.4426489	-0.0000108
C	-5.6425871	-0.8441613	-0.0000184
N	-4.8760309	-1.9685558	-0.0000172
C	-3.5590822	-1.7812680	-0.0000076
N	-0.8085020	-1.3075722	0.0000117
C	-1.3983079	-2.5315820	0.0000038
N	-2.7100661	-2.8252754	-0.0000057
H	-1.6622256	3.0313155	0.0000244
H	-6.7249568	-1.0115843	-0.0000268
H	-0.7126026	-3.3861185	0.0000057
H	3.4135492	3.1094777	-0.0000194
H	5.6146965	1.8756033	-0.0000274
H	3.4678433	-1.9015247	0.0000234
H	1.2792904	-0.6729761	0.0000315
H	0.1973327	1.4315844	0.0000072

Heptazine with Cl-PhOH:

C	3.9278357	1.5476083	0.0190938
C	2.5964686	1.0458386	0.0263108
C	1.5018287	1.9553608	-0.0217232
C	1.7440056	3.3292918	-0.0773288
C	3.0698595	3.8083290	-0.0861919
C	4.1664360	2.9180511	-0.0379357
O	2.4439508	-0.2729359	0.0793903
Cl	3.3628130	5.5142426	-0.1559581
N	0.0971589	-1.3587242	0.0752622
C	-1.1620603	-0.8971073	0.1284839
N	-2.2292070	-1.8243487	0.2263624
C	-1.9605675	-3.2142976	-0.0146609
N	-0.6939074	-3.6464823	-0.0649814
C	0.2684217	-2.7132800	0.0308302
N	-1.4066422	0.4180953	0.1204695
C	-2.7158536	0.7815606	0.1289987
N	-3.7946505	-0.0198823	0.0441063
C	-3.5629296	-1.3416886	0.0435611
N	-2.9842982	-4.0615444	-0.1542816
C	-4.2224452	-3.5220339	-0.1386480
N	-4.5649645	-2.2114521	-0.0942671
H	1.3074413	-3.0597282	0.0198841
H	-5.0542423	-4.2297484	-0.2208616
H	-2.9119065	1.8588365	0.1591130
H	4.7515454	0.8281815	0.0578408
H	5.1870083	3.3109952	-0.0451525
H	0.9115939	4.0379508	-0.1135978
H	0.4748125	1.5703829	-0.0091020

H	1.4524950	-0.5514719	0.0749836

Heptazine with Br-PhOH:

C	3.9335204	1.5424482	0.0001437
C	2.6016378	1.0423146	0.0002294
C	1.5082021	1.9542440	0.0000572
C	1.7512908	3.3295168	-0.0002426
C	3.0786915	3.8077553	-0.0003477
C	4.1747744	2.9138963	-0.0001409
O	2.4483562	-0.2772974	0.0004462
Br	3.3997614	5.6683855	-0.0007671
N	0.0946486	-1.3635378	0.0002546
C	-1.1622446	-0.8977604	0.0001589
N	-2.2314654	-1.8200351	-0.0003801
C	-1.9666951	-3.2269442	-0.0002541
N	-0.7016234	-3.6613174	-0.0001663
C	0.2626939	-2.7217680	-0.0000086
N	-1.4102110	0.4179536	0.0005525
C	-2.7204425	0.7780585	0.0004888
N	-3.8047288	-0.0232706	0.0002572
C	-3.5729374	-1.3454539	-0.0000687
N	-2.9976138	-4.0788839	-0.0003037
C	-4.2331844	-3.5340010	-0.0003408
N	-4.5788610	-2.2206972	-0.0001538
H	1.3011812	-3.0694736	-0.0000074
H	-5.0675845	-4.2433627	-0.0004563
H	-2.9165731	1.8557550	0.0007372
H	4.7564667	0.8209133	0.0002955
H	5.1978167	3.3006218	-0.0002121
H	0.9162146	4.0361045	-0.0003939
H	0.4805017	1.5705426	0.0001739
H	1.4584071	-0.5547074	0.0004490

Heptazine with PhOH:

C	1.1286021	-2.2374308	-0.0002474
C	-0.1700332	-2.8203391	0.0000657
C	-0.3143224	-4.2352230	0.0002561
C	0.8164897	-5.0509646	0.0000872
C	2.1055451	-4.4725596	-0.0002769
C	2.2519367	-3.0712447	-0.0004309
O	-1.2887446	-2.0972290	0.0000465
N	-1.2357627	0.5009980	0.0002413
C	-0.2720618	1.4329085	0.0005058
N	-0.6409764	2.7961418	0.0007939
C	-2.0233232	3.1664065	0.0001460
N	-2.9626872	2.2132679	-0.0001537
C	-2.5326956	0.9376523	-0.0000221
C	0.3673329	3.8001576	0.0002756
N	1.6595924	3.4366664	0.0002405

C	1.9128148	2.1124152	0.0004470
N	1.0207993	1.0867514	0.0004557
N	0.0136371	5.0857807	-0.0001741
C	-1.3197401	5.3426922	-0.0003552
N	-2.3458581	4.4637639	-0.0003140
H	2.9691275	1.8226052	0.0004575
H	-1.5985035	6.4017661	-0.0007892
H	-3.2954934	0.1518190	-0.0005202
H	1.2320194	-1.1459632	-0.0003525
H	3.2521441	-2.6260681	-0.0007216
H	2.9917347	-5.1152049	-0.0004539
H	0.7035785	-6.1397782	0.0002301
H	-1.3273702	-4.6491573	0.0005337
H	-1.0977816	-1.0906302	0.0000289

Heptazine with CH3-PhOH:

C	1.8772559	-0.2284492	-0.0000060
C	1.7223606	-1.6394014	-0.0000004
C	2.8740207	-2.4690413	0.0000298
C	4.1454649	-1.8986117	0.0000565
C	4.3177270	-0.4911198	0.0000528
C	3.1638519	0.3224606	0.0000197
O	0.5283238	-2.2450895	-0.0000150
C	5.7031992	0.1055202	0.0000862
N	-1.7264885	-0.8343502	-0.0001598
C	-2.0350670	0.4701705	-0.0002626
N	-3.3957455	0.8519782	-0.0005202
C	-4.4196429	-0.1438337	-0.0000297
N	-4.0825805	-1.4388206	0.0000650
C	-2.7638868	-1.7223676	-0.0001143
N	-1.0766353	1.4039970	-0.0001841
C	-1.4989945	2.6957832	-0.0001688
N	-2.7691177	3.1556942	-0.0000032
C	-3.7412400	2.2321955	-0.0000680
N	-5.7002411	0.2408159	0.0002661
C	-5.9319839	1.5736850	0.0002719
N	-5.0282938	2.5865154	0.0002249
H	-2.4820433	-2.7805274	-0.0001157
H	-6.9845343	1.8754426	0.0004359
H	-0.7098641	3.4550088	-0.0001938
H	0.9900810	0.4154575	-0.0000299
H	3.2768836	1.4127387	0.0000164
H	5.0282994	-2.5487082	0.0000815
H	2.7305184	-3.5541369	0.0000325
H	-0.2185091	-1.5697507	-0.0000541
H	6.2707608	-0.2195105	0.8891184
H	5.6653119	1.2057762	0.0000789
H	6.2708090	-0.2195210	-0.8889113

REFERENCES

1. Rabe, E. J., et al., Proton-Coupled Electron Transfer from Water to a Model Heptazine-Based Molecular Photocatalyst. *J. Phys. Chem. Lett.* **2018,** *9* (21), 6257-6261.
2. Djurovich, P. I., et al., Measurement of the lowest unoccupied molecular orbital energies of molecular organic semiconductors. *Org. Electron.* **2009,** *10* (3), 515-520.
3. Møller, C.; Plesset, M. S., Note on an approximation treatment for many-electron systems. *Phys. Rev.* **1934,** *46* (7), 618.
4. Schirmer, J., Beyond the random-phase approximation: A new approximation scheme for the polarization propagator. *Phys. Rev. A* **1982,** *26* (5), 2395-2416.
5. Ehrmaier, J., et al., Mechanism of photocatalytic water splitting with triazine-based carbon nitrides: insights from ab initio calculations for the triazine-water complex. *Phys. Chem. Chem. Phys.* **2018,** *20*, 14420-14430
6. Liu, X., et al., Computational investigation of the photoinduced homolytic dissociation of water in the pyridine–water complex. *Phys. Chem. Chem. Phys.* **2013,** *15* (16), 5957-5966.
7. Helgaker, T., Transition-state optimizations by trust-region image minimization. *Chem. Phys. Lett.* **1991,** *182* (5), 503-510.
8. Dunning Jr, T. H., Gaussian basis sets for use in correlated molecular calculations. I. The atoms boron through neon and hydrogen. *J. Chem. Phys.* **1989,** *90*, 1007.
9. Weigend, F., et al., RI-MP2: optimized auxiliary basis sets and demonstration of efficiency. *Chem. Phys. Lett.* **1998,** *294* (1-3), 143-152.
10. TURBOMOLE(V7.2)*, a development of University of Karlsruhe and Forschungszentrum Karlsruhe GmbH, 1989–2007, TURBOMOLE GmbH, since 2007.*

Appendix C: Supplementary Information for Chapter 5

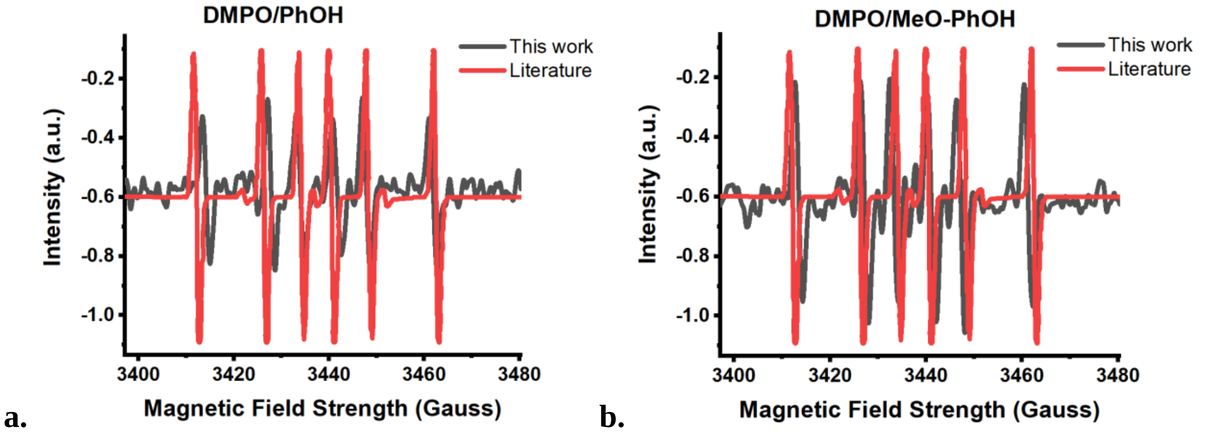

Figure C-1. Electron paramagnetic resonance spectra from this work and the literature of a. DMPO/PhOH radical adduct and b. DMPO/MeO-PhOH radical adduct. These suggest the radical we are detecting is from DMPO scavenging the phenoxyl radical after 365 nm irradiation.

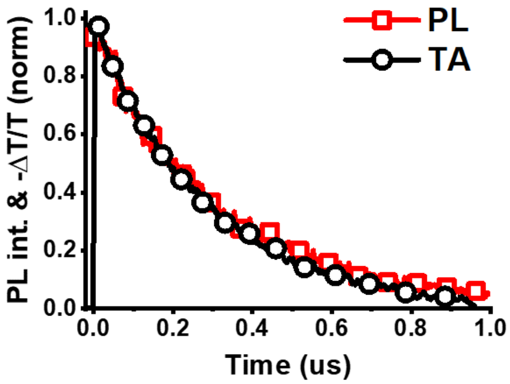

Figure C-2. Photoluminescence (480 – 520 nm) and transient absorption (900 – 1000 nm) decays of TAHz (30 μM) in toluene. Both traces are normalized to the maximum population at time zero. This demonstrates that the induced absorption and the photoluminescence are likely arising from the same excited-state species.

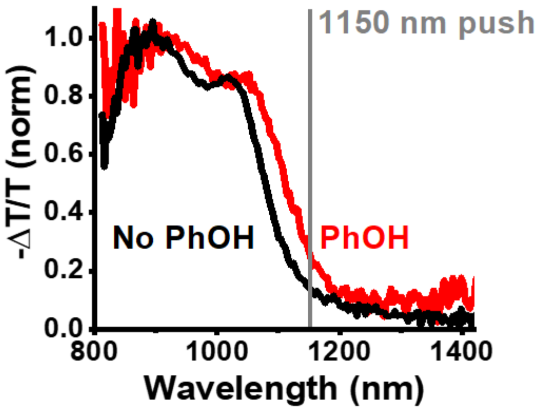

Figure C-3. Transient absorption spectrum of TAHz (50 μM) in toluene with (red) and without (black) phenol (1.0 M). Spectra averaged from 2-3 ps and normalized at 900 nm. This demonstrates a slight red shift due to the hydrogen bonding environment.

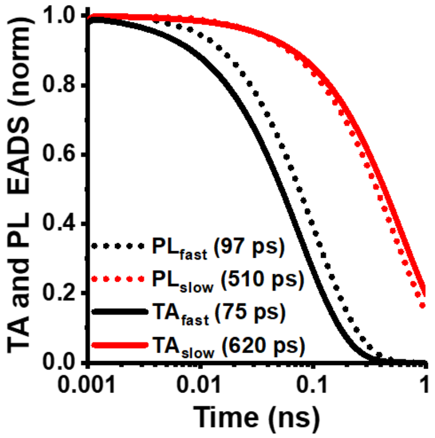

Figure C-4. The normalized transient absorption (TA) and photoluminescence (PL) evolution associated difference spectra (EADS) show two components with nearly identical decays.
This suggests luminescent species are the species being probed by transient absorption (pump-probe) spectroscopy. Data was collected with 15 μM TAHz in toluene with 1.0 M phenol.

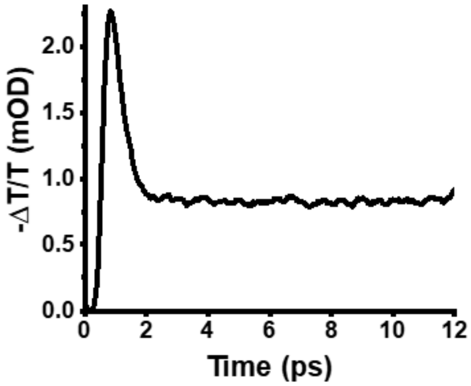

Figure C-5. The decay of the excited-state population of TAHz monitored from 500-550 nm in the presence of PhOH (1.0 M). Demonstrating the sub-picosecond relaxation of the S_n state after 365 nm excitation. Solvent reorganization is likely included in this relaxation.

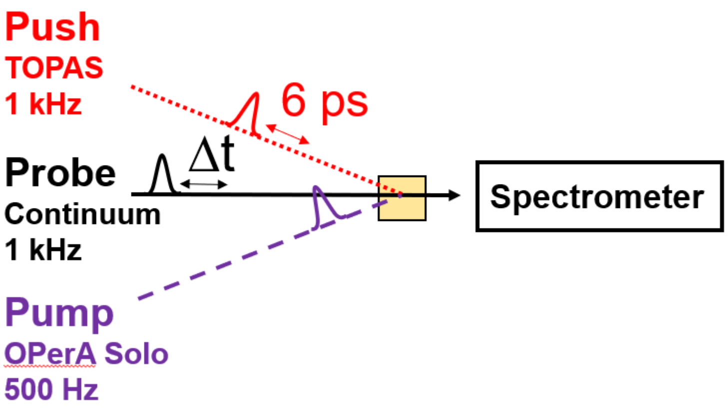

Figure C-6. Diagram of pump-push-probe beam overlap and timing.
The push in this work is fixed at 6 ps. The probe in this manuscript was delayed from 0 – 12 ps.

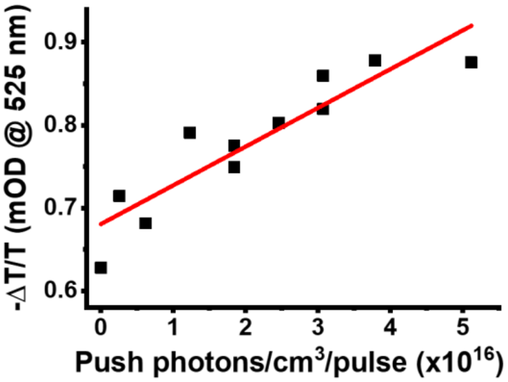

Figure C-7. Power dependence of push pulse on ΔOD transient absorption signal at 525 nm.
A linear dependence with signal intensity and push power implies the change in the signal due to the push pulse is a single-photon process.

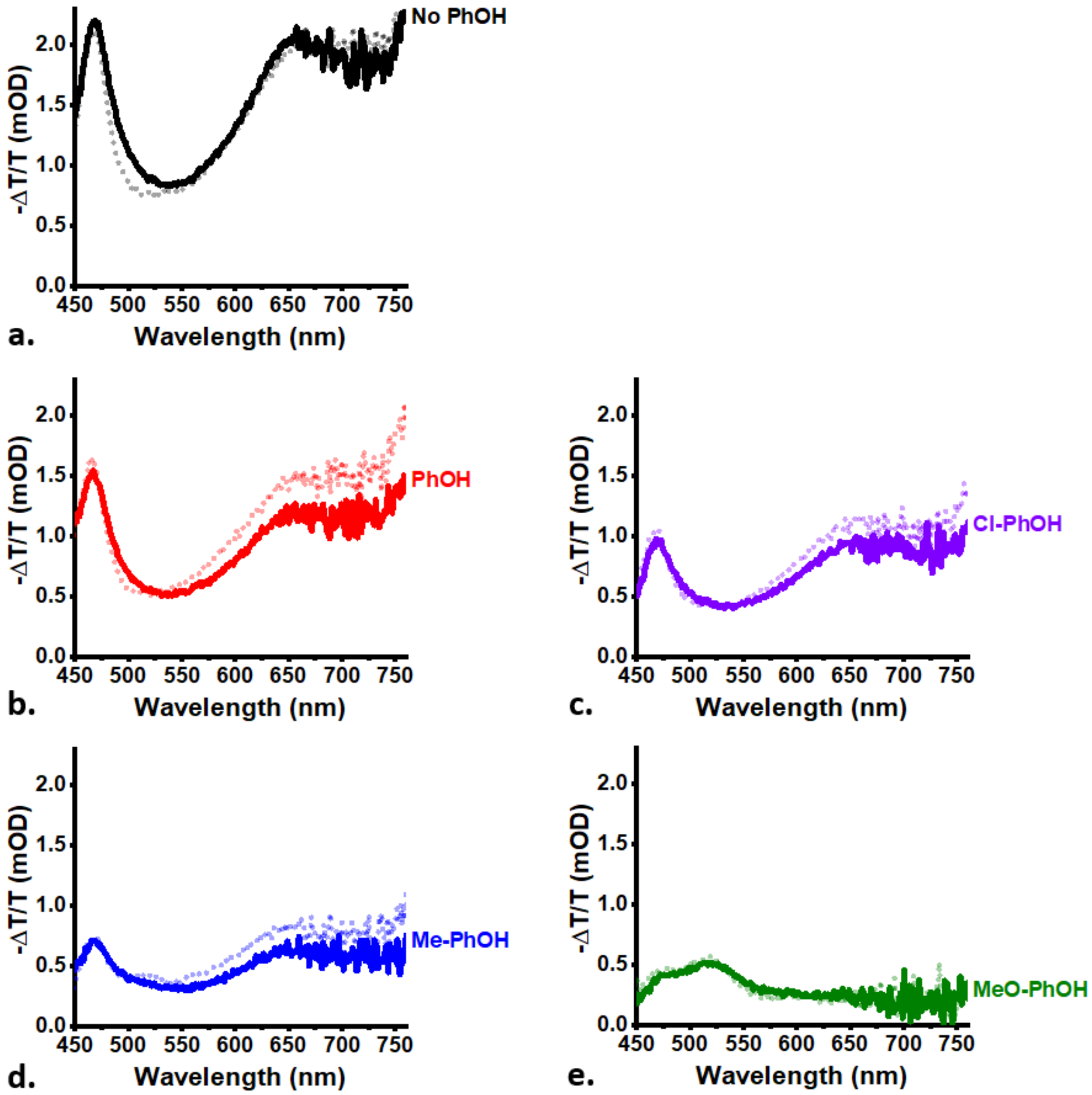

Figure C-8. Pump-push-probe spectra of TAHz (50 µM) in the presence of R-PhOH (1.0 M) with and without the push pulse (solid lines and dotted lines, respectively) averaged from 6.5 – 8.0 ps. The decrease in spectral intensity with the push pulse implies a loss of the excited-state hydrogen bonded species. MeO-PhOH (e) has very little change in spectra intensity with the push pulse, implying the push pulse did not considerably change the excited-state population. The system was pumped at 365 nm and pushed at 1150 nm at roughly 6 ps.

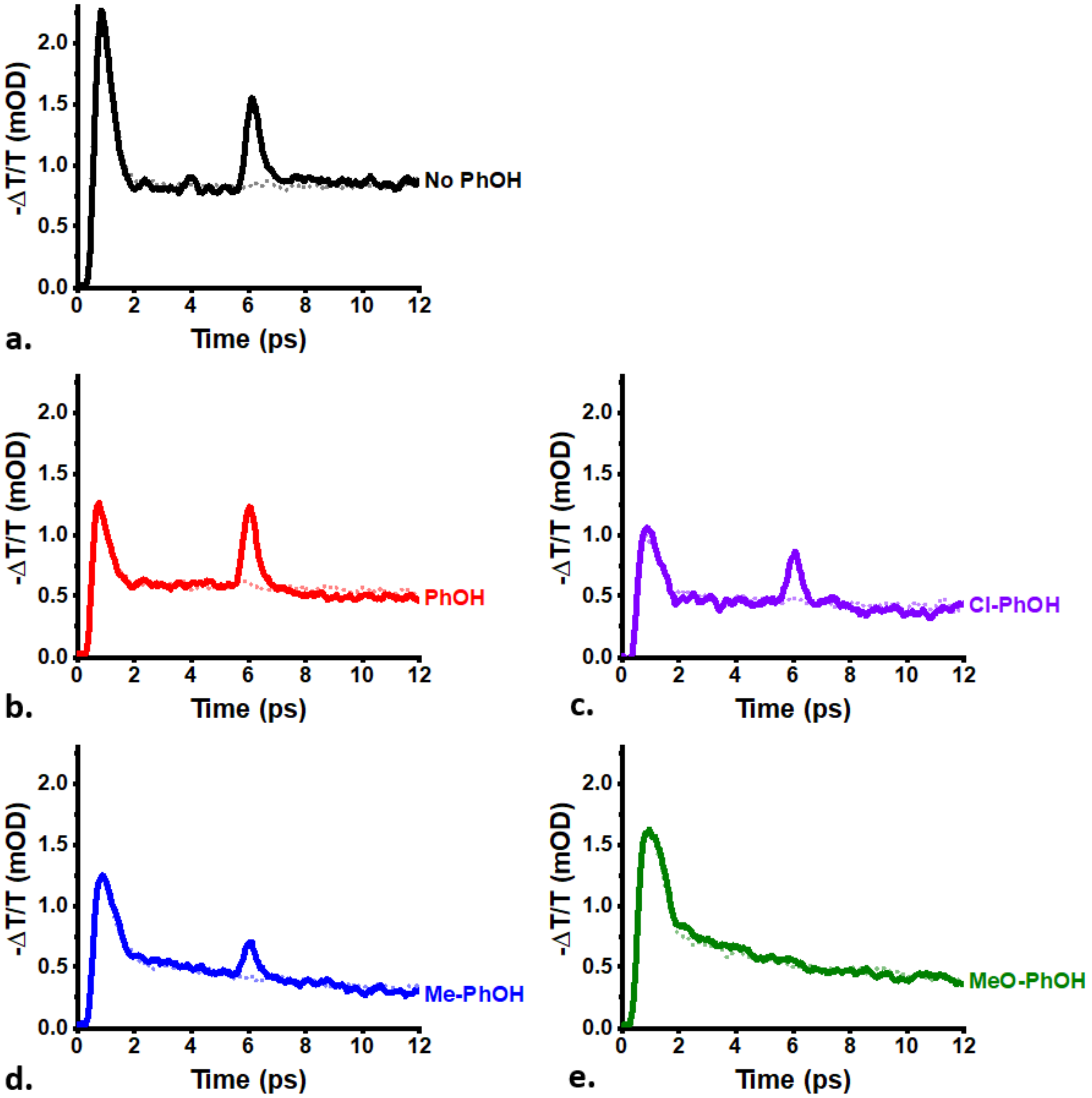

Figure C-9. The decay of the excited-state population of TAHz (50 μM) in toluene monitored from 500-550 nm in the presence of R-PhOH (1.0 M) with and without the push pulse (solid lines and dotted lines, respectively).

The short-lived species could be the absorption of a higher lying state that quickly relaxes. In the presence of MeO-PhOH (e), the push pulse does not readily populate this higher lying excited state. The system was pumped at 365 nm and pushed at 1150 nm at roughly 6 ps.

Kathryn L. Corp (208) 286-6118 katiecorp@gmail.com

PROFESSIONAL EXPERIENCES

Graduate Research Clean Energy Institute, University of Washington Sept. 2014 – Nov. 2019

Investigated the charge transfer processes in metal-free solar conversion materials using ultrafast spectroscopic techniques such as transient absorption and time-resolved photoluminescence. Uncovering the photophysics and electrochemical capabilities that control the efficiency of water splitting will dramatically influence rational design rules for organic energy conversion and storage systems.

Research Engineer Membrion, Inc. (Seattle, WA) Mar. 2014 – Sept. 2019

Developing and characterizing novel, inexpensive membranes for water purification and redox flow batteries. During my time here I've contributed heavily to 4 patent applications.

Lead Teaching Assistant University of Washington 2018 – 2019

Lead a group of 7-15 teaching assistants while teaching two sections of general chemistry. Organized and ran weekly meetings, proofread worksheets and exams, mentored other TAs, and divided grading.

Teaching Assistant University of Washington 2014 – 2019

General, Organic and Physical Chemistry, and Electronic Dynamics of Organic + Inorganic Materials

Mark Torrance Due Diligence Fellow E8 Angel Investors (Seattle, WA) 2017 - 2018

Consulted on clean energy technologies for investors while learning the business side of start-ups.

Education and Outreach Fellow Clean Energy Institute 2016 – 2017

Coordinated, managed and attended at least one outreach event per week. Created and edited clean energy curriculum for outreach events and University of Washington Clean Energy graduate classes.

Undergraduate Research Assistant Linfield College 2010 – 2014

Independently synthesized silver/gold composite nanoparticles and studied their enhancement of the Raman signal of various amino acids and 4-nitrobenzoic acid using our home-built Raman spectrometer.

Research and Business Intern Applied Physics Technologies, Oregon 2014

Characterized future electron sources for scanning electron microscopy. Assisted with office tasks.

International Research Experience, NSF Universite Paul Sabatier, France 2013

Synthesized colloidally stable bismuth nanoparticles and used NMR to investigate ligand stabilization.

LEADERSHIP POSITIONS

Undergraduate and Graduate Mentor University of Washington 2016 – 2019

Mentor undergraduate and graduate chemistry students in the Schlenker research group. Train students on electrochemical, synthetic, and spectroscopic techniques and general research etiquette.

President, Vice President, and Treasurer, Women in Chemical Sciences 2015 – 2019

Organize quarterly seminars and the annual named lecture, co-founded the graduate student mentoring program, and coordinated group outings for outreach and team building.

Resident Advisor Linfield College 2011 – 2014

Oversaw multimillion-dollar facilities, lead monthly hall meetings, and coordinated weekly events.

President, Chemistry Club Linfield College 2012 – 2013

Vice President, Pi Mu Epsilon (Math Honor Society) Linfield College 2013 – 2014

HONORS AND AWARDS

Scientific Achievement Award	Clean Energy Institute, University of Washington	2019
Sir Fraser Stoddart Scholar	Renewable Energy Scholarship Foundation	2019
Rising Women Fellowship	WRISE / GRID Alternatives	2018
Lloyd and Florence West Graduate Student Merit Fellowship	University of Washington	2018
Outreach and Service Award	Clean Energy Institute, University of Washington	2016
STEM Fellowship	Great Lakes Educational Loan Services, Academic Achievement	2015, 2016
Michael and Karen Schurr Endowed Fellowship	University of Washington	2014
Lois Gunning Fry Scholarship	Linfield College, Chemistry Department	2012, 2014
Student Leadership Award	American Chemical Society	2013

PRESENTATIONS

Research Seminar at University of Washington, Bothell	(invited talk)	2019
Inter-American Photochemical Society	(poster)	2019
Electron Donor-Acceptor Interactions Gordon Research Seminar and Conference	(poster)	2018
ORCAS: Energy Conversion & Storage - International	(posters)	2016, 2018
American Chemical Society National Meeting & Exposition	(posters)	2012, 2013, 2014
Oregon Academy of Sciences	(talks)	2012, 2013
Murdock Conference	(poster in 2011 and talk in 2012)	2011, 2012

PUBLICATIONS

8. **Corp, K.L.**; Rabe, E.J.; Schlenker, C.W. *In preparation.* **2019**. Photoinduced H-Atom Abstraction Reactions and Transient Intermolecular Excitations in Heptazine-Phenol Complexes.

7. Rabe, E.J.†; **Corp, K.L.†**; Estes, S.; Flores, R.; Haung, X.; Domcke, W.; Schlenker, C.W. *Submitted.* **2019**. Altering the H-Atom Donor: Elucidating Molecular Design Rules for Heptazine-Based Proton-Coupled Electron Transfer. †Authors contributed equally.

6. Pristash, S.; **Corp, K.L.**; Rabe, E.J. Schlenker, C.W. *Submitted.* **2019**. Triplet-Triplet Upconversion in All Organic Squaraine Chromophore: Expanding Light Harvesting for Solar Cells.

5. Ehrmaier, J.; Rabe, E.; Pristash, S.; **Corp, K.**; Schlenker, C.; Sobolewski, A.; Domcke, W. *J. Phys. Chem. A.* 123, 38, 8099-8108 **2019.** Singlet-Triplet Inversion in Heptazine and in Polymeric Carbon Nitrides. DOI: 10.1021/acs.jpca.9b06215

4. Rabe, E.J.; **Corp, K.L.**; Schlenker, C.W. *J. Phys. Chem Lett.* **2018**, 9, 6257-6261. Proton-Coupled Electron Transfer from Water to a Model Heptazine-Based Molecular Photocatalyst DOI: 10.1021/acs.jpclett.8b02519

3. **Corp, K.L.**; Schlenker, C.W. *JACS.* **2017**, 139, 7904-7912. Ultrafast Spectroscopy Reveals Electron-Transfer Cascade that Improves Hydrogen Evolution with Carbon Nitride Photocatalysts DOI: 10.1021/jacs.7b02869

2. Huang, C.Y.; Zou, C.; Mao, C.Y.; **Corp, K.L.**; Yao, Y.C.; Lee, Y.L.; Schlenker, C.W.; Jen, A.; Lin, L.Y., *ACS Photonics* **2017**, 4, 2281-2289. $CsPbBr_3$ Perovskite Quantum Dot Vertical Cavity Lasers with Low Threshold and High Stability DOI: 10.1021/acsphotonics.7b00520

1. Branca, M; **Corp, K.L.**; Ciuculescu-Pradines, D.; Coppel, Y.; Lecante, P.; Amiens, C., *New J. Chem.* **2017***, 41, 5960-5966.* Insights into the Chemistry of Bismuth Nanoparticles DOI: 10.1039/C7NJ01308F

EDUCATION

Doctoral Candidate in Chemistry	University of Washington, Seattle, WA	2014 – Nov 2019
Bachelor of Science in Chemistry & Mathematics	(Cum Laude) Linfield College	2010 – 2014